STUDY OF NANOSCALE DUCTILE MODE CUTTING OF SILICON USING MOLECULAR DYNAMICS SIMULATION

CAI MINBO

(M.Eng, B.Eng)

A THESIS SUBMITTED

FOR THE DEGREE OF DOCTOR OF PHILOSOPHY

DEPARTMENT OF MECHANICAL ENGINEERING

NATIONAL UNIVERSITY OF SINGAPORE

2007

Acknowledgement

First and foremost I would like to express my deepest and heartfelt gratitude to my supervisors, Professor Li Xiaoping, Professor Rahman Mustafizur, and Professor Steven Liang. Throughout the duration of the project, they provided me with not only strong technical guidance, a global view of research, background knowledge and many invaluable feedbacks on my research at all time, but also strong encouragement and kind affection.

I would like to thank Dr. Liu Kui for his precious advice and encouragement. Sincere appreciation is also expressed to the following staff for their help without which this project would not be successfully completed: Mr. Tan Choon Huat, Mr. Wong Chian Long, and Mr. Nelson Yeo from Advanced Manufacturing Lab (AML), who provided technical assistance in my study.

Special thanks come to my family members for their continuous support and understanding that helped me complete this work successfully.

At different stages of this research work, a lot of encouraging supports and help were delivered by my friends. Thanks also to my friends, Dr. Deng Mu, Dr. Xu Zhiping, Dr. Tang Shan, Dr. Liu Guangyan, Dr. Zhang Bin, Dr. Li Mingzhou, Dr. Zhang Guiyong, Javvaji Rajanish, He Tao, and Shamsul Arefin.

Last but not the least, I would like to thank the National University of Singapore for providing me with a research scholarship to support my study.

Table of Contents

Summary

Nanoscale ductile mode cutting of silicon wafers, by which good surface quality can be obtained, is an alternative approach for technological advancement in the semiconductor industry. Although much work has been done on micro/nano machining of brittle materials, the machining mechanism is not yet explained clearly.

In this research, a realistic molecular dynamics (MD) model taking into account the effect of tool cutting edge radius on the chip formation and cutting characteristics has been developed. Based on this model, MD simulations have been carried out to study the ductile mode cutting of monocrystalline silicon.

Different cutting tool edge radii and cutting directions were applied to simulate the cutting process. The simulated variation of the cutting forces with the tool cutting edge radius was compared with the cutting force results from experimental cutting tests. The good agreement of results indicated that the present MD model and simulation system can be used for simulation of the nanoscale ductile mode cutting of silicon. The results denoted that the stress in the cutting process is not uniformly distributed along the cutting tool edge, and the elastic spring-back of small thickness exists on the machined workpiece surface. The results also showed that the cutting direction has no obvious effects on the cutting forces and deformation of workpiece.

The mechanism of ductile chip formation has been explained based on the study of phase transformation in the ductile cutting of monocrystalline silicon. The results of

MD simulations of nanoscale cutting of silicon showed that because of the high hydrostatic pressure in the chip formation zone, there is a phase transformation of the monocrytslline silicon from diamond cubic structure to both β silicon and amorphous phase in the chip formation zone, which results in plastic deformation of the work material in the chip formation zone as observed in experiments.

In this study, based on the tensile stress distribution and the characteristics of the distribution obtained from MD simulation of nanoscale ductile cutting of silicon, an approximation for the tensile stress distribution was obtained. Using this tensile stress distribution with the principles of geometrical similarity and fracture mechanics, an upper bound of tool cutting edge radius for crack initiation has been found.

The crack initiation in the ductile-brittle mode transition as the undeformed chip thickness is increased from smaller to larger than the tool cutting edge radius has been studied using the MD method on nanoscale cutting of monocrystalline silicon with a non-zero edge radius tool, from which, for the first time, a peak deformation zone in the chip formation zone has been found in the transition from ductile mode to brittle mode cutting. This finding explains well the ductile-brittle transition as the undeformed chip thickness increases from smaller to larger than the tool cutting edge radius.

A new concept “dynamic hard particles” was proposed to investigate the mechanism of micro/nano groove wear formation in ductile mode cutting of monocrystalline silicon with a diamond tool. The MD simulation results showed that the temperature rise in the chip formation zone could soften the material at the flank face of the diamond

cutting tool. Also, the high hydrostatic pressure could result in “dynamic hard particles” in the material. Having the “dynamic hard particles” ploughing on the softened flank face of the diamond tool, the micro/nano grooves could be formed, yielding the micro/nano groove wear as observed.

Nomenclature

a	lattice constant of monocrystalline silicon
a_c	undeformed chip thickness
a_{ix}	the ith atom's acceleration in the x direction
A	proportional coefficient for hardness function
b	size of tensile stress field
	lattice constant of aluminum
c	crack length
c^*	critical crack length
$\mathscr{C}$	nominal defect length
$\mathscr{C}^*$	critical nominal defect length
D	cohesion energy
d_a	affected zone thickness
d_c	critical indent size or depth of cut
d_s	spring-back thickness
E	elastic modulus
E_g	energy gap
E_{tot}	total energy of a system
f	tool feed
f_A	attractive pair potential
f_C	smooth cut-off function
f_R	repulsive pair potential
F	embedding energy

F_c	cutting force
F_t	thrust force
F_{ijx}	interaction force acting on the *i*th atom by the *j*th atom in the *x* direction
F_{ijy}	interaction force acting on the *i*th atom by the *j*th atom in the *y* direction
F_{ijz}	interaction force acting on the *i*th atom by the *j*th atom in the *z* direction
F_{ix}	resultant force on the *i*th atom in the *x* direction
F_{iy}	resultant force on the *i*th atom in the *y* direction
F_{iz}	resultant force on the *i*th atom in the *z* direction
F_m	maximum cutting force
$\mathscr{F}$	nominal cutting force
$\mathscr{F}^*$	critical nominal cutting force
H	material hardness
H_c	cutting hardness
H_s	scratching hardness
k_B	Boltzmann constant
K_I	stress intensity factor
K_{Ic}	critical stress intensity factor
L	interatomic bond length
m_i	mass of the *i*th atom
N	number of atoms
N_e	electron density
P^*	critical load
r_{ij}	the distance between particle *i* and particle *j*
r_0	atomic distance at equilibrium
R	tool cutting edge radius

R^*	critical tool cutting edge radius
R_a	surface roughness
R_c	specific work per unit area required to propagate a crack
R_n	tool nose radius
t	time
Δt	time step
T	temperature
υ_i	resultant velocity of the *i*th atom
υ_c	cutting velocity
V_{ij}	bond energy
W_h, W_w	height and width of the area subject to cutting force in the cutting direction
y_c	subsurface damage depth
α	elastic modulus for potential
β_1, β_2	material constants
ε	minimum of potential
η	dimensionless constant
θ	dimensionless factor
θ_{ijk}	bond angle
κ	dimensionless factor
λ_1, λ_2, λ_3	dimensionless factors
ζ	ratio of the cutting hardness to the indentation hardness
ζ_{ij}	number of other bonds to atom *i* besides the *ij* bond
$\rho(r_{ij})$	‘‘atomic density’’ function
$\overline{\rho_i}$	host ‘‘density’’

σ_c	critical tensile stress
σ_{cleave}	resolved tensile stress
σ_m	maximum tension at the interface
σ_y	yield stress
σ_{xx}, σ_{yy}	normal stresses
σ_0	material constant for potential
τ_c	critical shear stress
τ_{slip}	resolved shear stress

List of Figures

List of Tables

Chapter 1

Introduction

1.1 Significance of the Research

Since the transistor action in germanium was discovered by J. Bardeen and W. H. Brattain in 1948, the high technology based on the semiconductor has been explosively developing. To meet rapid developments of high technology, semiconductor industry has also been keeping pace in the world. Silicon is a typical semiconductor material, and constitutes 90% of all semiconductor materials. Monocrystalline silicon wafer can be found in every type of microelectronic application, including computer systems, telecommunication equipment, automobiles, consumer electronics products, industrial automation and control systems and analytical and defense systems.

As a substrate material, silicon is used in microelectronic chips, which require flatness and good surface integrity. Currently, silicon wafers are finished by grinding, lapping and polishing. Because grinding is a kind of random and uncontrolled material removal process, the brittle fracture and severe subsurface damage are inevitable. Therefore, the surface left by grinding operation cannot be directly used for further application. The post-grinding polishing operation is usually needed to make the wafer achieve a high quality surface. This manufacturing process is complicated, time consuming and costly.

Nanoscale ductile mode cutting of silicon wafer materials, by which good surface quality can be obtained without requirement for subsequent polishing, tends to be an alternative approach for technological advancement in semiconductor industry. Since the 1980s, many researchers have reported the nanoscale ductile cutting of brittle materials, such as silicon and germanium. It has been well recognized that ductile machining of monocrystalline silicon can be achieved when depth of cut is down to several tens of nanometers. Moreover, many attempts have been made to systematically understand the ductile behavior of brittle materials and the machining mechanism of this technology. This emerging technology is important because of the decrease in production time, which has many manufacturing and economic advantages.

1.2 Background and Literature Review

In machining, a layer of material is removed from the workpiece material surface in two types of machining modes: ductile mode and brittle mode, which normally depend on the workpiece material property. For materials with high ductility, the ductile mode controls the machining process and continuous chips can be formed; for brittle materials with low fracture toughness, the machining process is normally in the brittle mode and the chip is discontinuous. However, material removal depends not only on the workpiece materials but also on the machining parameters. Under special machining conditions, brittle materials like ceramics, glass, and silicon, which are difficult to machine because of the low fracture toughness of these materials, still can be removed with continuous chip in ductile mode like the machining of ductile materials.

Ductile mode machining is a great advance in machining of brittle materials, and obviously it is beyond the understanding based on conventional cutting processes. Therefore, many researchers have attempted to understand the mechanism of ductile mode machining of brittle materials. In this regard, molecular dynamics (MD) method has been used to simulate the nanoscale ductile mode machining of brittle materials.

This chapter provides an overview of literature in the areas of ductile mode machining of brittle materials. The following topics relevant to the present study are reviewed:

- Machining of brittle materials;
- Material removal mechanism of brittle materials;
- Molecular dynamics simulation of nanoscale machining;
- Diamond tool wear in ductile mode machining.

1.2.1 Machining of Brittle Materials

Amongst the materials which are difficult to machine, most are those that are hard and brittle, for example, glasses and engineering ceramics and semiconductors. The ability to manufacture high quality surfaces from them is becoming more reliant on processes such as ductile mode machining. Improvements in machining tolerances have enabled the researchers to achieve the ductile mode removal of brittle materials. There are two distinct topics among the studies on ductile machining of brittle materials, which are ductile mode grinding and cutting.

1.2.1.1 Ductile Mode Grinding

The possibility of grinding brittle materials in a ductile mode was proposed as early as 1954, when it was noted that during frictional wear of rock salts, although there was some cracking and surface fragmentation, the material removal process was dominated by plastic deformation in the surface layers but not fracture (King and Tabor, 1954). By 1975, improvements in precision diamond grinding mechanisms allowed the first reproducible evidence of grinding ductility in brittle glass workpieces (Huerta and Malkin, 1976).

The first systematic studies of grinding ductility were performed using a single grit grinding apparatus. It was observed that the nature of cracking is very similar to that occurring about a quasi-static pointed indenter. The material-removal regime in this experiment was shown to progress through three stages: plastic grooving, generation of median and lateral cracks, and finally crushing (Swain 1979). In this study, it was demonstrated that the progression of material-removal mechanism was directly related to the force on the abrasive grain, with lower forces corresponding to a decrease in the observed surface fracture.

The study of Bifano et al. (1988, 1991) showed that by controlling a stiff, accurate grinding apparatus so that it has an exceptionally small scale of material removal, brittle materials can be ground in a ductile manner. As a result, a brittle workpiece can be machined in a deterministic process while producing a surface finish characteristic of those achieved in nondeterministic, inherently ductile processes such as lapping and polishing. A model of critical depth of cut was proposed based on the experimental

results and the details will be introduced in the section on mechanism of ductile mode machining later in this chapter.

Ductile grinding, lapping and polishing of silicon, silicon carbide and glass materials show that polishing time can be reduced by grinding with smaller grit size diamonds having higher concentration so as to increase ductile mode and reduce fracture mode (Zhong and Venkatesh, 1994). Observation on polishing and ultraprecision machining of semiconductor substrate materials indicated that ductile grinding using chemical-mechanical polishing has many advantages (Venkatesh et al., 1995). The elimination of the polishing process altogether, or a substantial reduction in polishing time had been successfully established by the use of electrolytic in-process dressing technique (ELID) (Ohmori and Nakagawa, 1990).

Pei et al. (1998) studied the subsurface cracks in silicon wafers machined by surface grinding process. Based on a cross-sectional microscopy method, several crack configurations were identified and the relation between the depth of the subsurface crack and the wheel grit size was experimentally determined. Pei et al. (2001, 2002) investigated the unique requirements regarding the grinding wheels, the grinder design, and the process parameter optimization in fine grinding of silicon wafers.

1.2.1.2 Ductile Mode Turning

Pioneering work on the design and construction of single point diamond turning (SPDT) machine was initiated in the 1970's at Lawrence Livermore National Laboratory (LLNL) (Komanduri et al., 1997). In the past two decades, diamond turning has been used for ultraprecision machining in a variety of ductile materials, polymers and crystals. Brittle materials were initially considered as non-machinable

for diamond turning because of the severe subsurface damage and high tool wear rate. With improvements in machining tolerances, it was found that it is possible to machine the brittle material in ductile mode at a very small depth of cut.

The single point diamond turning process is a well-established technology for the production of mirror surfaces (Blackley and Scattergood, 1990, 1991; Leung et al., 1998). The salient feature of this technology is the ability to control directly the contour as well as the surface roughness by direct numerical control. Puttick et al (1995) argued that although the finished surface roughness value in the diamond cutting is much better than in grinding, it is not certain that the diamond cutting is superior to grinding, because he found that subsurface damage also can be observed under the condition of ductile regime machining.

Research into ductile mode cutting of brittle materials is concentrated on germanium and silicon. Blake and Scattergood (1990), who studied the precision machining of germanium and silicon using single-point diamond turning, pointed out that the critical chip thickness is a governing pivotal parameter, which governs the transition from plastic flow to fracture along the tool nose. Nakasuji et al. (1990) carried out single-point diamond turning of silicon with a tool having a nose radius of 0.5-1 mm and a rake angle varying from 0 to -25^{o} and found a surface roughness of 0.04 μm. Ductile-regime response during diamond turning of brittle germanium crystals was evident from the damage-free surfaces obtained and the chip topography provided insight into the ductile regime machining of germanium that occurred along the tool nose (Balckley and Scattergood, 1994). A germanium surface and the chips produced from a single-point diamond turning process operated in the ductile-regime was analyzed by

transmission electron microscopy and parallel electron-energy-loss spectroscopy. Lack of fracture damage on the finished surface and continuous chip was indicative of a ductile removal process (Morris et al, 1995). Shibata et al. (1996) experimented on silicon wafers with a single-point diamond tool of nose radius 0.8 mm and a rake angle of -40^o . The depth of cut was taken as 100 nm and 500 nm at a feed rate of 10 mm/rev and a speed of 3.3 m/s. Kerosene was used as the cutting fluid and at 100 nm depth of cut, a mirror-finished surface of roughness value 20 nm was obtained. Fang and Venkatesh (1998) reported that for turned silicon surfaces with roughness value of R_a = 23.8 nm, mirror surfaces of 1 nm roughness were achieved repeatedly by micro-cutting, where a depth of cut of 1 μm was used. Leung et al. (1998) carried out direct machining of silicon on a precision lathe equipped to a finish of 2.86 nm roughness and found that in order to produce a high quality surface, it is necessary that the machining process is in the ductile regime and the chip thickness must be less than the critical value, which depends on the machining conditions. Yan et al (2001) have studied the role of hydrostatic pressure in the ductile machining of silicon using a single crystal diamond tool with a large negative rake and undeformed chip thickness in the nanoscale range. The stage was arranged inside a high external hydrostatic pressure apparatus and the results indicate that large hydrostatic pressure is helpful to realize ductile cutting. Liu and Li (2001) further observed that only when the undeformed chip thickness is smaller than the cutting edge radius of a zero rake angle tool (the tool cutting edge radius R and the undeformed chip thickness a_c are shown in Figure 1.1) and the tool cutting edge radius is small enough, ductile mode cutting can be achieved.

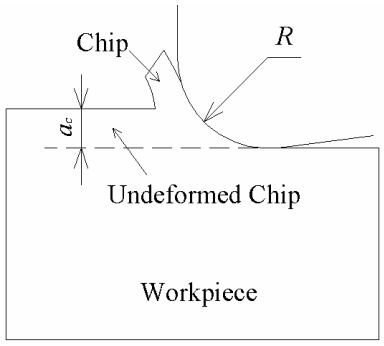

Figure 1.1 The schematic of cutting process.

1.2.2 Material Removal Mechanism of Brittle Materials

Based on past research work available, the material removal mechanism in brittle materials is reviewed as follows.

1.2.2.1 Material Removal with Microfracture

During conventional machining operations on brittle materials, most of the material is removed by brittle fracture, enabling higher removal rates. An appreciation of the mechanism of material removal by this mode can be obtained by comparing this process with indentation-sliding analysis (Lawn and Evans, 1977; Lawn et al., 1980). The material removal takes place in six stages. As shown in Figure 1.2, (a) the material under the indenter is initially subjected to elastic deformation. This creates a small inelastic deformation zone due to high hydrostatic pressure below the indenter; (b) a median vent is formed on a plane of symmetry containing the contact axis at the elastic-plastic boundary; (c) further increase of load makes the median vent stable; (d) the median vent begins to close as the load is removed; (e) the lateral vents are formed as indenter removal goes on and spread out laterally on a plane closely parallel to the specimen surface. Residual stresses are the main cause of lateral cracks, (f) as the

indenter is removed completely, lateral vents continue to extend towards the specimen surface and may eventually lead to removal of material by chipping.

In nanometric cutting of brittle materials such as silicon using a monocrystalline diamond tool, this mode of material removal must be avoided as much as possible to eliminate brittle fracture and consequent micro-crack formation on or near the surface.

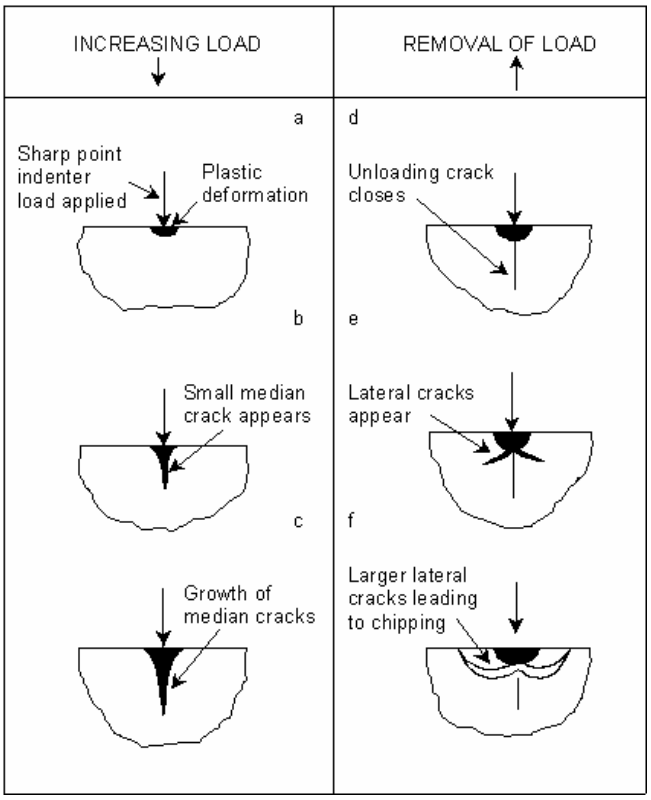

Figure 1.2 Schematic showing various stages of indentation (Lawn and Wilshaw, 1975).

1.2.2.2 Brittle-Ductile Transition

Much work about ductile mode machining of brittle materials has been reported, but the nature of the brittle-ductile transition is not clear. Systematic study of the machining mechanism and technology is of theoretical significance and practical

value. Many researchers have been delving into understanding the phenomena of brittle-ductile transition and revealing the mechanism. Some initial work is noteworthy and briefly described here.

(1) Competition between shear stress and tensile stress

Nakasuji et al. (1990) and Shimada et al. (1995) proposed a possible material removal mechanism, which can be classified into two modes when machining brittle materials. One is the process due to plastic deformation in the slip direction on the characteristic slip plane and the other is due to cleavage fracture on the characteristic cleavage plane. When the resolved shear stress τ_{slip} in the slip direction on the slip plane exceeds a certain critical value τ_c inherent to the workpiece material, plastic deformation occurs in a small stressed field in the cutting region of a specified scale, which may correspond to the depth of cut, for example. On the other hand, a cleavage occurs when the resolved tensile stress normal to the cleavage plane σ_{cleave} exceeds a certain critical value σ_c. The mode of material removal depends on which criteria dominates or precedes $\tau_{slip} > \tau_c$ or $\sigma_{cleave} > \sigma_c$ for the stress state under a particular machining condition.

Furthermore, they argued that this transition is related to the defect density in the machining region. Figure 1.3 shows a model of chip removal with a size effect in terms of defects distribution. When the machining scale is larger than a micrometer, micro-cracks and dislocations are usually included in the stress field. σ_c sensitively decreases as the scale of machining increases because the number of defects in the stress field increases. On the other hand, τ_c is not sensitive to the defect. Therefore, brittle mode material removal is the predominant criteria in this region. When the machining scale

becomes smaller, such as sub-micrometer or nanometer, both of σ_c and τ_c increase to the same level as the intrinsic strength of a perfect workpiece material. Then, plastic deformation takes place before cleavage.

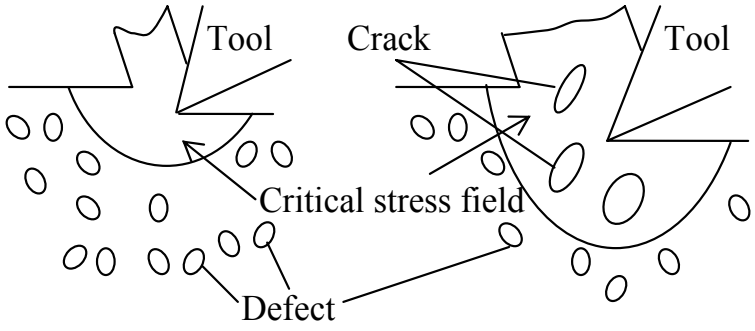

Figure 1.3 A model of chip removal with a size effect in terms of defects distribution: (a) small depth of cut; (b) large depth of cut.

(2) Extrusion

In the indentation hardness field, pyramidal indenters, such as Vicker's, Knoop, and various conical indenters are classified as sharp indenters while spherical indenters as blunt indenters. If indentation sliding is applied to simulate ultra-precision machining, grinding, or abrasion then all these indenters do in fact fall into the category of blunt indenters. For example, a Vicker's indenter with a 136^o included angle would be equivalent to a high negative rake angle of -68^o. The spherical indenter would be equivalent to a varying high negative rake angle from close to $\sim$ - 90^o at the tool-workmaterial interface to whatever the angle subtended by the tool at the depth of cut line is. Thus, both radius and the depth of cut of the spherical indenter come into the picture in this case. Shaw (1972) proposed a mechanism of material removal involving extrusion of heavily deformed material ahead of a large radius tool in grinding of

ductile metals (Figure 1.4) and Komanduri (1971) proposed a mechanism likening the grinding process to machining with high negative rake tools (Figure 1.5).

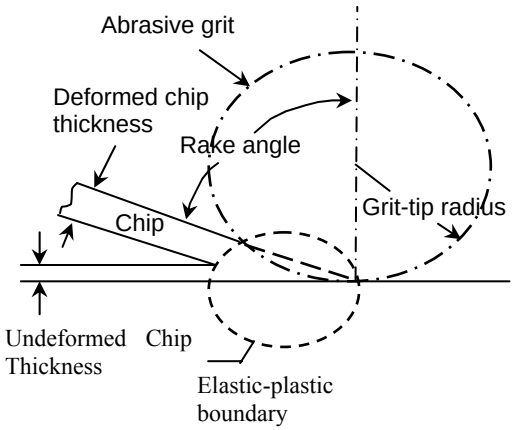

Figure 1.4 Mechanism of material removal involving extrusion of heavily deformed material ahead of a large radius tool in grinding of ductile metals.

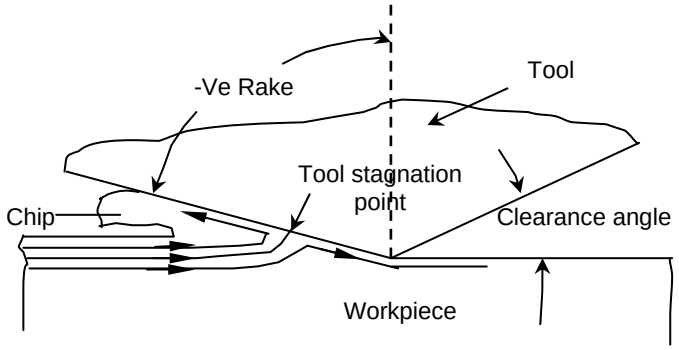

Figure 1.5 Mechanism of material removal in grinding with machining with high negative rake tools.

Puttick et al (1994) used similar models to include the case of nanometric cutting of a nominally brittle material, such as silicon. They proposed that brittle materials may be machined in a ductile manner provided that the depth of cut is restricted below a critical value for crack initiation predicted by energy scaling. Ductile machining is like the extrusion of plastic material ahead of the tool.

(3) Critical chip thickness

Some researchers have attempted to explain why there is a critical threshold of the undeformed chip thickness in the ductile mode cutting of brittle materials. One of the explanations is based on a model (Lawn and Evans, 1977) for crack initiation in elastic/plastic indentation fields. In this model, Lawn and Evans obtained a lower bound of the critical crack length c^* and the critical load P^* to the requirements for crack initiation in indentation,

$$c^* = \beta_1 (K_{Ic} / H)^2 , \; P^* = \beta_2 (K_{Ic} / H)^3 K_{Ic} , \tag{1.1}$$

where β_1 and β_2 are constants for different materials, K_{Ic} is the critical stress intensity factor, and H is the material hardness. Below this critical load P^*, no crack will be initiated. Corresponding to this critical condition, Marshall and Lawn (1986) proposed that the critical indent size d_c is scaled to the critical crack length c^*,

$$d_c = \mu (K_{Ic} / H)^2 , \tag{1.2}$$

where $\mu \propto E/H$ and E is the elastic modulus. Based on this formula, describing the critical depth for fracture during indentation of hard materials, Bifano et al. (1991) investigated ductile-regime grinding. They postulated a basic hypothesis for ductile-regime grinding: all materials, regardless of their hardness or brittleness, will undergo a transition from brittle machining regime to a ductile machining regime if the grinding infeed rate is made small enough. Below this threshold infeed rate, the energy required

to propagate a crack is larger than the energy required for plastic yielding, so plastic deformation becomes the predominant grinding mechanism.

Based on Eq. (1.2), Blake and Scattergood (1990), Blackley and Scattergood (1991) claimed that although the chip formation action of a diamond turning tool differs dynamically and geometrically from the deformation produced using indentation, there are essential similarities in both processes and it will be hypothesized that a critical depth parameter d_c will divide fracture from ductility in ultraprecision. They also developed a model for single point diamond turning of brittle materials to determine the critical depth parameter in a certain machining condition by experiments. Figure 1.6 shows a projection of machining cut perpendicular to the cutting direction.

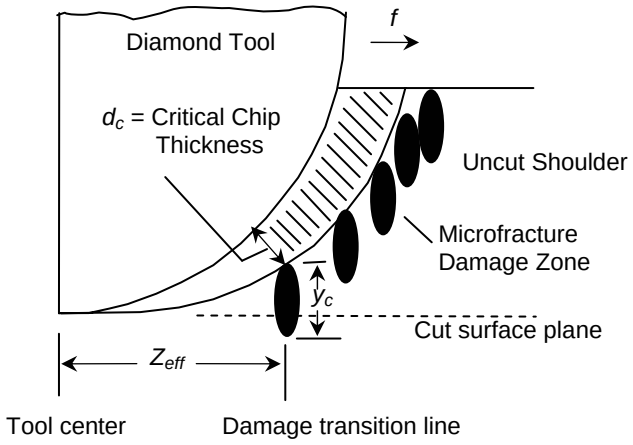

Figure 1.6 A projection of machining cut perpendicular to the cutting direction.

According to the energy balance concept, fracture damage will initiate at the effective cutting depth and will propagate to an average depth. The chip thickness varies from zero at the tool center to a maximum at the top of the uncut shoulder as shown in the figure. As long as the damage does not replicate beyond the cut surface plane, ductile

regime conditions are achieved. If the damage extends too deeply into the substrate, the subsequent machining will not remove all the damaged material and indeed some damage will remain in the finished workpiece surface. The model uses two parameters, the critical depth of cut d_c and the subsurface damage depth y_c, to characterize the ductile-regime material removal process. Eq. (1.3) was derived so that both d_c and y_c could be obtained using the known machining parameters, namely, tool nose radius R_n and tool feed f, and location of the ductile-to-brittle transition Z_{eff},

$$\frac{Z_{eff} - f^2}{R_n^{\,2}} = \frac{d_c^{\,2}}{f^2} - 2\left(\frac{d_c + y_c}{R_n}\right). \tag{1.3}$$

Puttick et al. (1989) used a critical linear dimension d_c of the stressed volume of material to predict the critical depth of cut in the ductile mode machining of glass,

$$d_c = \beta E R_c / \sigma_y^2, \tag{1.4}$$

where σ_y is the yield stress for plastic flow and R_c the specific work per unit area required to propagate a crack.

1.2.3 Molecular Dynamics (MD) Simulation of Nanoscale Machining

Except the experimental and theoretical studies on nanoscale machining of brittle materials, numerical simulation technology also has been applied to simulate and study the nanoscale machining of brittle materials. The nanoscale cutting involves changes in only a few atomic layers near the surface of the workpiece, and needs to be studied from the atomic viewpoint. On such a small governing length scale, the continuum

representation of the problem becomes questionable. Therefore, a MD simulation method has been attempted in the present work.

1.2.3.1 The Concept of MD Simulation

MD simulation is a methodology investigating statistical properties of material systems. Predictions based on an atomistic level of understanding are providing increasingly useful and accurate information for a myriad of applications in material science, tribology and machining. Unlike the FEM, in MD simulation nodes and the distance between nodes are selected not on an arbitrary basis but on more fundamental units of the material, namely, centres of the atoms as the nodes, i.e. the crystal lattice is similar to the FEM mesh and interatomic distance to the distance between the nodes. Thus the process can be reduced to the materials' fundamental units for analysis. Also, MD techniques give higher temporal and spatial resolution of the cutting process than is possible by a continuum mechanics approach. Consequently, certain phenomena of necessity neglected in continuum analysis can be effectively investigated by MD simulation. Now, MD is playing an increasingly prominent role in the analysis of the behaviour of materials at an atomistic level that cannot be readily obtained either by other theoretical methods or by experiments (Komandury and Raff, 2001).

MD studies were initiated in the late 1950s at the Lawrence Radiation Laboratory (LRL) in the United States by Alder and Wainwright (1959, 1960) in the fields of equilibrium as well as non-equilibrium statistical mechanics to calculate the response of several hundred interacting classical particles using the then available highly powerful mainframe computers at LRL. Since then, MD simulation has been applied to a range of fields including crystal growth, indentation, tribology, low-pressure

diamond synthesis and laser interactions. However, its application to machining is of recent origin and only a limited number of research groups around the world are actively involved in investigating these processes.

1.2.3.2 MD Simulation of Machining of Metals

In LRL, Hoover et al. (1989) studied the interface tribology using MD simulation of fabrication technology; Belak and Stowers (1990) have studied both two- and three-dimensional cutting of copper using the potential energy of embedded-atom method (EAM) at a cutting speed of 100 m/s with different edge radii tools and different depths of cut. The diamond cutting tool was assumed to be infinitely hard in cutting copper. With the two-dimensional MD model, Ikawa et al. (1991a, 1991b), Shimada et al. (1992, 1993, 1994), and Shimada (1995) investigated the effect of tool edge radius and depth of cut on the chip formation process, subsurface deformation, specific energy etc. Inamura et al. (1992, 1994) followed the changes in the minimum energy positions, which are the mean positions of the vibrating atoms, i.e. under quasi-static condition. However, because of the fewer atoms used, the interpretation of results is not as obvious as in MD simulation. Rentch and Inasaki (1994a, 1994b) used MD to simulate the abrasive process and found the pile-up phenomenon in abrasive machining. They also investigated the surface integrity in abrasive machining. Komanduri (1998) built a three-dimensional model to simulate the cutting of copper and investigated the effect of tool geometry in nanoscale cutting. Fang and Weng (2000) have studied the nanoscale cutting of copper by a pin tool with three-dimensional MD simulation. Ye et al. (2003) employed the MD method to simulate copper removal, chip formation and frictional forces.

1.2.3.3 MD Simulation of Machining of Silicon

As a type of brittle material, monocrystalline silicon can be machined in ductile mode on the nanoscale. On this small scale, MD method is suitable for the simulation of ductile mode machining of silicon. However, very little effort on MD simulation has been expended in this area. This is due to the complex potential involved for silicon in the simulation.

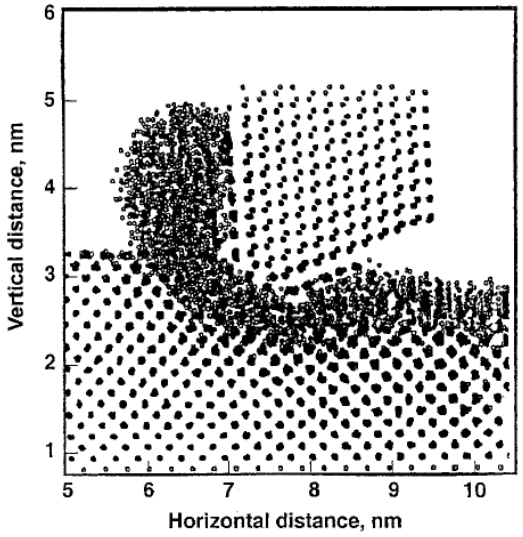

Figure 1.7 The cutting of silicon with diamond tool at a cutting speed of 540 m/s showing that the first few layers of newly cut surface appear to be amorphous (Belak et al.,1993).

Belak et al. (1993) have used the Tersoff potential to simulate the cutting of silicon with diamond tool at a cutting speed of 540 m/s and found that the silicon atoms in the chip and in the first few layers of newly cut surface appear to be amorphous (as shown in Figure 1.7). They pointed out that less energy is required to transform the crystal into an amorphous solid than to shear the crystal. These observations are very significant in attempting to understand the mechanism of material removal in semiconductor materials. They also found that the temperature in the chip was comparable to the bulk melting temperature of silicon. Such a temperature is too high

and unrealistic, and has never been reported in the experiments. It may be caused by the high cutting speed (540 m/s) in the simulation.

Shimada et al. (1997) also found amorphous phenomenon by MD simulation. They explained that the energy of elastic waves comes from potential energy and when the energy released is not enough to create the microcrack, ductile cutting is realized. Zhang and Tanaka (1998) used MD simulation to study the atomic scale deformation in silicon induced by two-body and three-body contact sliding and found that amorphous phase transformation is the main deformation phenomenon. They (1999) also simulated the indentation of silicon and the results showed that inelastic deformation of silicon is caused by amorphous phase transformation. Cheong and Zhang (2000) further found that there is a phase transformation from diamond cubic structure to β silicon in the MD simulation of indentation of silicon.

Although the phase transformation has been found in MD simulation and it is supposed to be the cause of inelastic deformation, why the phase transformation causes ductile machining is not clear. Also, the difference between the inelastic deformation in ductile machining of silicon and the plastic deformation in machining of ductile metals has not been studied in detail.

Inamura et al. (1997, 1999) proposed to use the renormalized MD to study the brittle-ductile transition phenomena in the machining of silicon. Their results showed that a microcrack-like defect could be initiated during cutting of monocrystalline silicon at a depth of cut of 1 micron. They assumed that the defect was created though the interaction between a local microscopic static stress and a global dynamic stress

associated with acoustic waves. In their simulation, the tool cutting was assumed to be perfectly sharp and the effect of the tool cutting edge radius was ignored. This is obviously unacceptable, because the tool cutting edge radius is an important factor related to the crack initiation according to the experiment results, which have been mentioned in section 1.2.1.

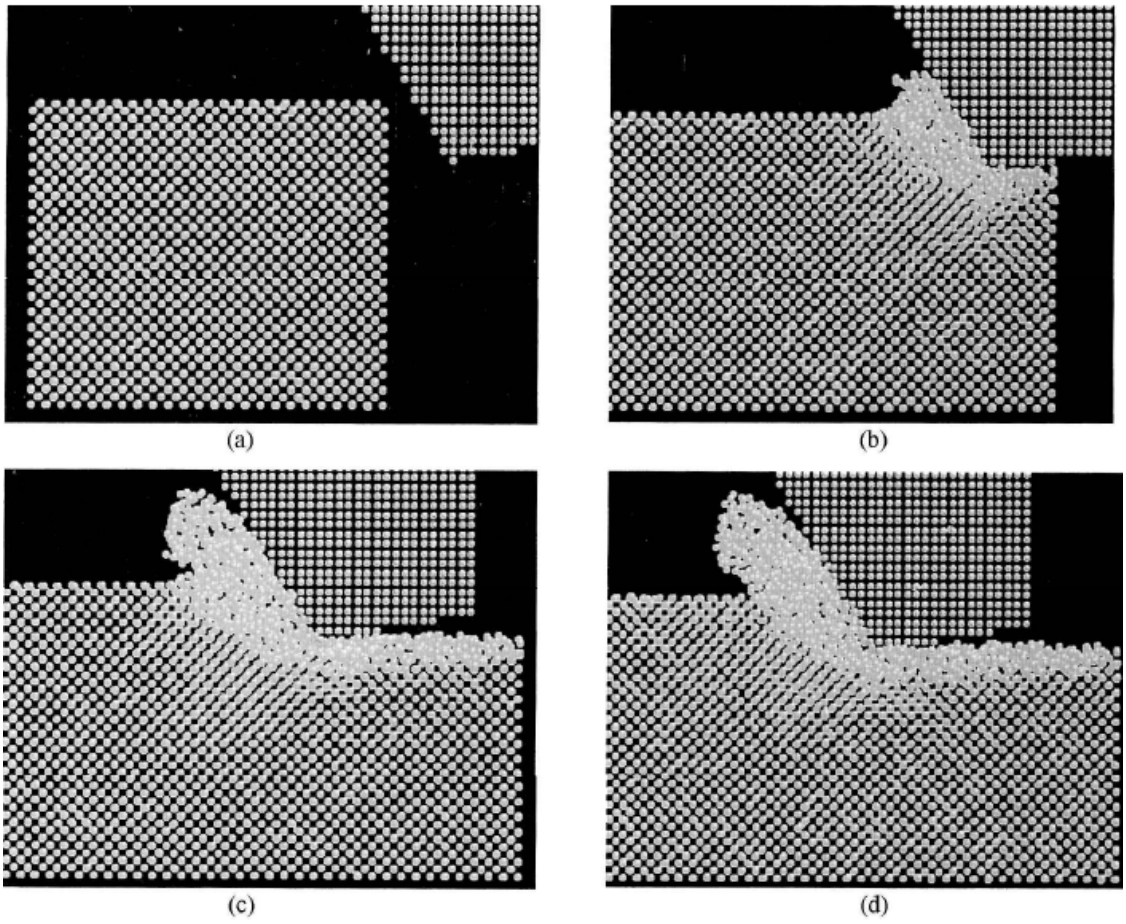

Figure 1.8 MD simulation of the nanometric cutting of silicon at various stage of chip formation with a -30° rake angle (depth of cut 1.1 nm) (Komanduri et al., 2001).

Komanduri et al. (2001) applied MD to simulate nanometric cutting of single-crystal, defect-free, pure silicon. The simulation was performed using the Tersoff potential over a wide range of rake angles (from -60° to +60°), depths of cut (0.01 to 2.72nm) and clearance angles (10° to 30°) to investigate the nature of material removal and

surface generation process in ultraprecision machining. Figure 1.8 shows the MD simulation results of the nanometric cutting of silicon at various stages of chip formation with a -30° rake angle (depth of cut 1.1 nm). The simulation of silicon cutting shows an extrusion-like chip formation process without a specific crystallographic preference. This appears to be due to a phase transformation from α to β silicon under a hydrostatic pressure and consequent densification of the material. In their simulation, the tool cutting edge radius has not yet been considered.

Han et al. (2002) carried out MD simulations with various tool edge radii and various depths of cut to study the effect of tool geometry on nanometric machining. The results showed that in the case of nanometric cutting, the edge radius cannot be ignored compared with the depth of cut. However, their simulations could not show the hydrostatic pressure in the chip formation zone to support their claim. Moreover, the result that the sharp tool also could cause ductile mode cutting in the simulation is unacceptable, because the sharp cutting tool cannot provide the hydrostatic pressure that is necessary in the ductile mode cutting of silicon according to their claim.

Fang et al. (2005) also modeled the nanoscale cutting of monocrystalline silicon with various tool edge radii, but in their simulation, they could not obtain the threshold value of the ratio of chip thickness to cutting edge radius.

MD simulation is fast becoming a widely used technique in understanding the deformation mechanisms of materials. Based on MD simulation, some special phenomena, such as chip formation, workpiece deformation and phase transformation during nanoscale cutting can be observed at the nanoscale level, but it is difficult to

observe them by other methods. Using MD simulation, it is easy to change the machining conditions to get different results, as is helpful for us to understand the mechanism of nanoscale cutting. Therefore, the MD is a useful method and it provides a good approach to study the nanoscale machining of brittle materials.

1.2.4 Diamond Tool Wear in Ductile Mode Cutting

Rapid wear of single point diamond tools is a limiting factor in ductile mode cutting of silicon wafers. Because of the existence of high hydrostatic pressure and the property of brittle materials, the wear of diamond cutting tools is rapid. Since cutting is carried out at the nanoscale, any wear of the tools will affect the quality of the finish surface of the workpiece. Therefore, it is very important to study the wear of diamond tools in nanoscale ductile mode cutting. A number of researchers in the past have made contributions to a better understanding of tool wear processes in cutting metal materials using a diamond tool, for example, Keen (1971) and Wada et al. (1980). Some researchers have extended their investigation into the wear of diamond tools in cutting of glass and single-crystal silicon (Glardon and Finne, 1981; Yan et al., 2003; Li et al., 2005).

Yan et al. (2003) dealt with the performance of diamond cutting tools during single point diamond turning of monocrystalline silicon substrates at a machining scale smaller than 1 μm. The cutting edge, the finished surface and the cutting chips were examined by scanning electron microscope (SEM) and the micro-cutting forces were measured. It was found that tool wear could be generally classified into two types: micro-chippings and gradual wear, the predominant wear mechanism depending on the undeformed chip thickness. In ductile mode cutting, flank wear was predominant and the flank wear land was characterized by trailing micro-grooves and step structures.

Li et al. (2005) studied the tool wear characteristics in nanoscale ductile mode cutting of monocrystalline silicon and the effects of the tool wear on the chip formation mode. It was found that the tool cutting edges undergo two processes simultaneously. One was the wear of material on the tool main cutting edge, which increased the main cutting edge radius, but left the shape of the main cutting edge unchanged, enhancing the conditions for ductile mode chip formation. The other one was the generation of nano or micro grooves at the tool flank, which formed sub-cutting edges of much smaller radii on the main cutting edge. As the grooves became deeper, the sub-cutting edges extended towards the tool rake face ultimately becoming the dominating cutting edge of much smaller radius. In such a way these sub-cutting edges tended to change the cutting mode from ductile to brittle.

Maekawa and Itoh (1995), and Cheng et al (2003) used MD simulation to study the tool wear in nanoscale machining, and they observed the tip wear of the sharp cut in the simulation, but they have not explained the tip wear using the MD simulation results. As to groove wear observed by Li et al. (2005), the MD simulation has not been used to study it.

1.3 Problem Formulation

As previously mentioned, ductile mode machining of brittle materials, such as ceramics and semiconductor, has been investigated and developed over the years. It has been found that when the depth of cut is down to nanoscale and some other machining conditions are satisfied, brittle materials can be machined with a

performance like ductile materials. However, the mechanism of ductile mode cutting of brittle materials has not been explained clearly.

In most of the studies, the radius of the tool cutting edge is normally ignored and the tool is assumed to be completely sharp. Nevertheless, in nanoscale cutting of materials, where the undeformed chip thickness can be well below 100 nm and the smallest cutting edge radius of a moncrystalline diamond tool may still be in the range of 20–70 nm under the current best manufacturing condition, this assumption is obviously not reasonable. Although some researchers have used MD to model the tool cutting edge radius and study its effects on cutting of brittle materials, they have not considered the relation between the tool cutting edge radius and the undeformed chip thickness. That is, they have not observed the differences in the simulation under different cutting conditions, where the tool cutting edge radius can be larger or smaller than the undeformed chip thickness. Some researchers have studied the upper bound of cut depth, but it is without the consideration of tool cutting edge radius, so consequently the upper bound tool cutting edge radius has not been theoretically studied.

Although most of the studies show that there is plastic deformation in ductile mode cutting of brittle materials, the essence of this plastic deformation is not clear. That is, what causes plastic deformation is unknown. With consideration of the tool cutting edge radius, the mechanism of ductile chip formation has not been adequately explained. Some researchers have used the phase transformation from diamond cubic structure to β silicon to explain the ductile chip formation, but the β phase silicon has not been shown clearly and why the phase transformation from diamond cubic structure to β silicon leads to ductile is not well answered.

The groove wear of diamond tool in ductile mode cutting of silicon has been reported. In conventional cutting processes, such as cutting of alloys, the groove wear of tool flank face is usually caused by abrasion, in which hard particles (carbide, nitride or oxide) in the workpiece material abrade the tool face and form grooves on it. Since a monocrystalline silicon body is supposedly free of hard particles, and the diamond cutting tool material is much harder than monocrystalline silicon at room temperature, the generation of grooves in nanoscale cutting of monocrystalline silicon with diamond tools is beyond the understanding based on conventional cutting processes. Until now, the mechanism of groove wear also has not been explained clearly.

1.4 Objectives of Research

The purpose of this research was to develop a MD simulation system as a tool to study nanoscale ductile mode cutting of monocrystalline silicon. The following objectives were to be achieved in this research:

- To develop a realistic MD model and a MD simulation system for simulation of nanoscale ductile mode cutting of monocrystalline silicon, in which the tool cutting edge radius is considered.

- To study the effect of tool cutting edge radius and cutting direction on cutting forces and deformation of silicon workpiece in nanoscale ductile mode cutting of monocrystalline silicon.

- To understand the mechanism of ductile chip formation in nanoscale ductile mode cutting of silicon based on the study of phase transformation in the chip formation zone.

- To explain the experimental phenomenon that there is an upper bound of tool cutting edge radius in nanoscale ductile mode cutting of silicon based on the tensile stress distribution and the characteristics of the distribution obtained from MD simulation of nanoscale cutting of silicon.

- To investigate crack initiation in the ductile-brittle mode transition as the undeformed chip thickness is increased from a smaller value to a larger value than the tool cutting edge radius.

- To study the mechanism of micro/nano groove wear of diamond tools in nanoscale ductile mode cutting of monocrystalline silicon with monocrystalline diamond cutting tools.

1.5 Thesis Organization

The thesis details the study of nanoscale ductile mode cutting of monocrystalline silicon with diamond tools using MD simulation. The background related to the machining of brittle materials, material removal mechanism of brittle materials, MD simulation of nanoscale machining and diamond tool wear in ductile mode cutting of brittle materials, are reviewed in Chapter 1.

Chapter 2 firstly introduces the MD method. Based on the MD method, a MD model and a simulation system of ductile mode cutting of monocrystalline silicon are described.

Chapter 3 describes the experimental details, including experimental materials, experimental equipment, and procedure.

MD was employed to simulate the ductile mode cutting of monocrystalline silicon. Different cutting tool edge radii and different cutting directions were applied in the simulations. Furthermore, an experiment was conducted to verify the MD model. In Chapter 4, the comparison of cutting forces between the simulated results and experimental results is presented. Also, the simulated results of deformation of the chip formation zone, the elastic spring-back of small thickness, and the effects of the cutting direction are introduced in this chapter.

In the ductile mode cutting of monocrystalline silicon, why can the ductile chip be formed and what is the essence of the ductile deformation? Chapter 5 is to answer these questions.

Chapter 6 explains the experimental phenomenon that there is an upper bound of tool cutting edge radius in nanoscale ductile mode cutting of silicon based on the tensile stress distribution and the characteristics of the distribution obtained from MD simulation of nanoscale cutting of silicon.

A new finding that a peak deformation zone in the chip formation zone occurs in the transition from ductile mode to brittle mode cutting is described in Chapter 7. Based on this finding, the ductile-brittle transition as the undeformed chip thickness increases from smaller to larger than the tool cutting edge radius is explained.

Chapter 8 presents a possible mechanism of micro/nano diamond tool groove wear formation in ductile mode cutting of monocrystalline silicon with a diamond tool based on the studies of temperature and deformation in the chip formation zone of silicon workpiece. In this proposal, a new concept of "dynamic hard particles" is introduced into the study of diamond groove wear.

In Chapter 9, the conclusions of this study about MD simulation of ductile mode cutting of monocrystalline silicon are described in the following aspects: the MD model, the effects of tool cutting edge radius, the mechanism of ductile chip formation, the upper bound of tool cutting edge radius, the crack initiation in relation to undeformed chip thickness, and the mechanism of diamond tool groove wear. Moreover, some recommendations for future work about this study are also given in this chapter.

Chapter 2

Molecular Dynamics Simulation Method and Model

2.1 Introduction

A simulation system for nanoscale ductile mode cutting of monocrystalline silicon has been developed in this thesis using the molecular dynamics (MD) method for better understanding of the ductile mode cutting mechanism. This chapter first introduces the MD method. Based on the MD method, a MD model of ductile mode cutting of monocrystalline silicon was built. In this model, the initial atom positions of silicon workpiece material are arranged according to the crystal lattice structure, the atomic interactive actions of silicon are based on the Tersoff potential, the diamond cutting tool is assumed to be undeformable, the tool cutting edge is realistically modeled to have a finite radius, and the motions of the atoms in the chip formation zone are determined by the Newton's equation of motion. For the simulation of this MD model, a MD simulation system has been developed.

2.2 Molecular Dynamics Simulation Method

2.2.1 The Principles of MD Simulation

In the MD simulation method, an appropriate potential energy function of the material

is needed to describe the interatomic energy of the material. Based on this potential energy function, the interatomic force can be derived. Then, the acceleration of every atom can be obtained according to the Newton's equation of motion. Consequently, the new position of every atom can be determined when the initial position and velocity of every atom have been given. The essence of the MD simulation method is the numerical solution of Newton's equation of motion for an ensemble of atoms. These equations are integrated by numerical techniques for extremely short time intervals (on fs scale, 1 fs = 10^{-15} s), and statistical averages, such as the temperature, the stress, etc., are computed as temporal averages over the observation time.

2.2.2 Potential Energy Functions

The potential energy function is the base of the MD simulation, because in the MD simulation, there is a need to consider the forces that exist between the atoms, for it is these forces that decide much of what happens in any physical phenomenon. Furthermore, these forces are determined by the potential energy functions. While the accuracy of the potential dictates the quality of the simulation results, its functional complexity determines the computational time required for a given computing system. These potential energy functions vary depending on the type of material and a potential that is developed for one type of material would not be satisfactory for application to other materials. Therefore, it is necessary to develop a potential for each type of material. Normally, empirical potentials are used. Empirical potentials are based on simple mathematical expressions for the pairwise interaction between two atoms or ions, which may or may not be justified from theory, and which will contain one or more parameters adjusted to the experimental data. The validity of the function as well as the stability of the crystal for a given material are checked for various properties

including cohesive energy, the lattice constant, the compressibility and the elastic constants as well as the equation of state. Consequently, these potentials can be considered to be reasonably valid for simple cubic crystals.

Figure 2.1 shows the dependence of attractive, repulsive and net forces (a) and potential energies (b), as a function of the interatomic separation, *r*, for two isolated atoms (Kommandury and Raff, 2001). The attractive force binds the atoms together while the repulsive force prevents them from coalescing. The magnitude of both forces increases as the distance between them decreases, the repulsive force increasing more rapidly than the attractive force. The curvature of the potential energy function is determined mainly by the repulsive force, which therefore dictates the elastic behaviour of the solid. The length of the bond *r* is the centre-to-centre distance of the bonding atoms. Strong bonds pull the atoms closer and so have smaller bond lengths compared with weak bonds. At r_0, the attractive and the repulsive forces exactly balance and the net force is zero. This corresponds to stable equilibrium with a minimum potential energy, the magnitude of which is the bond energy.

Some commonly used potentials are introduced in the following:

(1) Lennard-Jones potential

At the beginning of the MD method, it was mainly used to simulate inert gases and liquids, and some simple pair potentials were developed. Lennard-Jones potential is one of them. Normally, the Lennard-Jones ‘6-12’ potential (Lennard-Jones, 1925; Lennard-Jones and Dent, 1926) is used and the function is given as

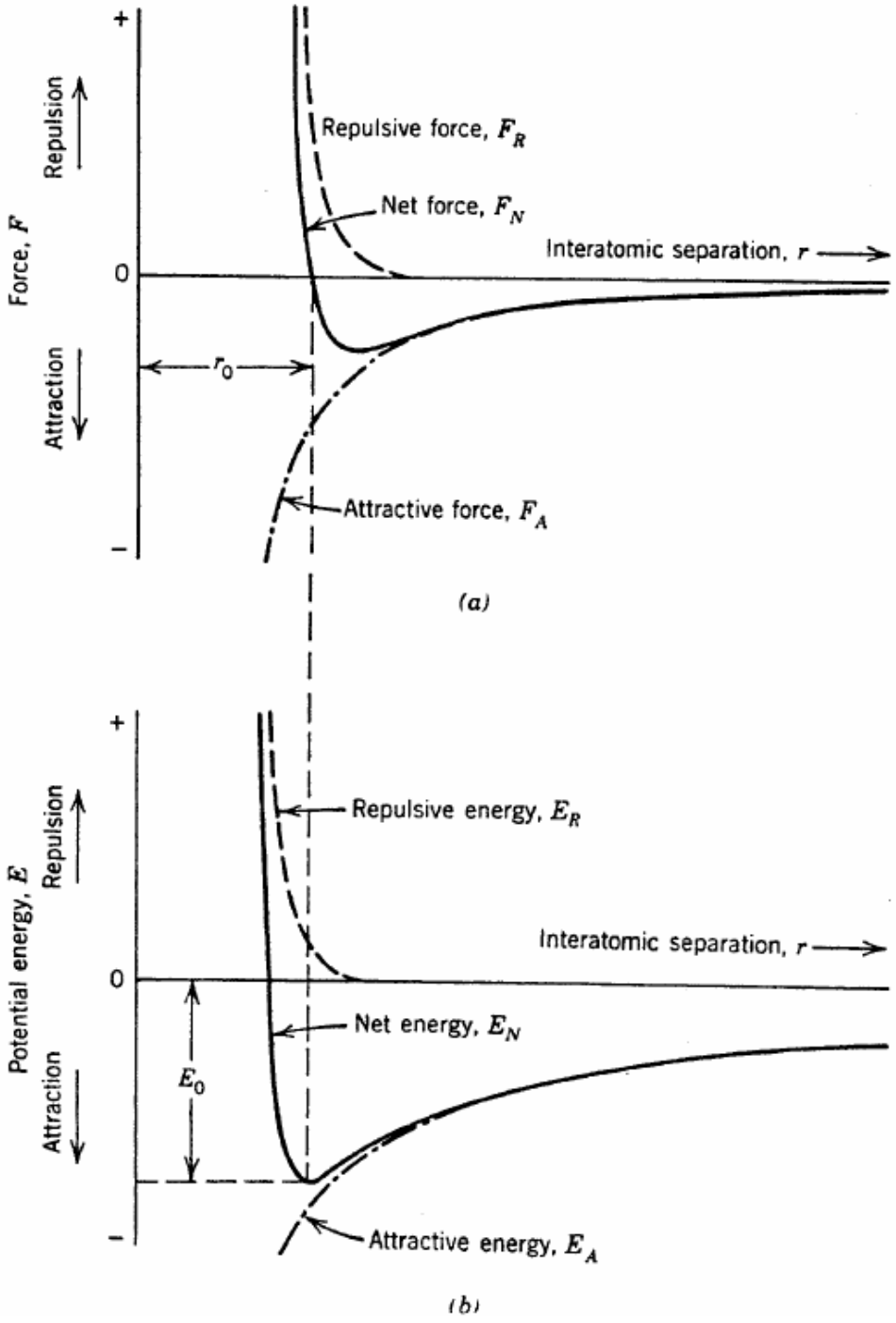

Figure 2.1 Variation of the attractive, repulsive and net forces (a) and the attractive, repulsive and net potential energies (b), as a function of the interatomic distance *r* between two atoms (Kommandury and Raff, 2001).

$$V_{ij} = 4\varepsilon\left[\left(\frac{\sigma_0}{r_{ij}}\right)^6 - \left(\frac{\sigma_0}{r_{ij}}\right)^{12}\right], \tag{2.1}$$

where V_{ij} is the bond energy of all the atomic bonds, r_{ij} denotes the distance between particle i and particle j, ε is the minimum of potential, which occurs when the distance r_{ij} is equal to $2^{1/6}\sigma_0$, where σ_0 is determined by the physical property of the material.

(2) Morse potential

Morse potential is a popularly used empirical pairwise potential energy function for bonded interactions (Morse, 1929) and many researchers have given the different constants of Morse potential for different materials. This potential produces repulsive force in the short range, attractive force in the medium range and decays smoothly to zero in the long range. It uses a form of potential containing two exponential terms instead of power law dependence considered by other researchers. The Morse potential energy function is given by

$$V_{ij}\left(r_{ij}\right) = D\left\{\exp\left[-2\alpha\left(r_{ij} - r_0\right)\right] - 2\exp\left[-\alpha\left(r_{ij} - r_0\right)\right]\right\}, \tag{2.2}$$

where D, α and r_0 correspond to the cohesion energy, the elastic modulus and the atomic distance at equilibrium, respectively.

In the simulation of this thesis, the interactions between atoms of the workpiece and carbon atoms of diamond cutting tool are obtained from Morse potential and the parameters are shown in Table 2.1.

Table 2.1 The parameters for Morse potential.

Item	D (eV)	α (nm^{-1})	r_0 (nm)
C - Si	0.435	46.487	0.19475
C - Al	0.280	27.80	0.22

(3) Embedded atom method potential

The EAM (embedded-atom method) potential is a type of multi-body potential and is normally used to describe the system energy of cubic materials, such as aluminum, copper and so on (Daw and Baskes, 1983 and 1984; Baskes, 1992; Foiles, 1996; Doyama and Kogure, 1999; Mishin, et al., 1999). In this potential the total energy of a system is represented as

$$E_{tot} = \frac{1}{2}\sum_{ij} V_{ij}(r_{ij}) + \sum_{i} F(\ \overline{\rho_i}\ ). \tag{2.3}$$

Here $V_{ij}(r_{ij})$ is a pair potential as a function of the distance r_{ij} between atoms i and j, and F is the "embedding energy" as a function of the host ''density'' $\overline{\rho_i}$ induced at site i by all other atoms in the system. The latter is given by

$$\overline{\rho_i} = \sum_{j \neq i} \rho(r_{ij}), \tag{2.4}$$

$\rho(r_{ij})$ being the ‘‘atomic density’’ function. The second term in Eq. (2.3) is volume dependent and represents, in an approximate manner, multi-body interactions in the system.

(4) Tersoff potential

For the diamond lattice with covalent bonds, Stillinger-Webers Silicon Potential (Stillinger and Weber, 1985) and Tersoff potential (Tersoff, 1988, 1989) are available to describe the potential. These potentials consider not only the pair bond energy, but also the energy contributed by the covalent bond. It is found that the Tersoff potential can well describe the energy and geometry of silicon (Zhang and Tanaka, 1998; Komanduri et al., 2001). Therefore, the Tersoff potential is applied to the MD simulation of cutting of silicon, as follows:

$$E_{tot} = \sum_i E_i = \frac{1}{2}\sum_{i \neq j} V_{ij}\ ,\ V_{ij} = f_C(r_{ij})[f_R(r_{ij}) + b_{ij} f_A(r_{ij})], \tag{2.5}$$

$$f_R(r_{ij}) = A_t \exp(-\lambda_t r_{ij})\ ,\ f_A(r_{ij}) = -B_t \exp(-\mu_t r_{ij})\ , \tag{2.6}$$

$$f_C(r_{ij}) = \begin{cases} 1, & r_{ij} < R_t \\ \frac{1}{2} + \frac{1}{2}\cos[\pi(r_{ij} - R_t)/(S_t - R_t)], & R_t < r_{ij} < S_t \\ 0, & r_{ij} > S_t \end{cases}, \tag{2.7}$$

$$b_{ij} = (1 + \beta_t^{n_t} \zeta_{ij}^{n_t})^{-1/2n_t}, \zeta_{ij} = \sum_{k \neq i,j} f_C(r_{ik}) g(\theta_{ijk})\ , \tag{2.8}$$

$$g(\theta_{ijk}) = 1 + c_t^2 / d_t^2 - c_t^2 / [d_t^2 + (h_t - \cos\theta_{ijk})^2]\ , \tag{2.9}$$

where E_i is the site energy, V_{ij} is the bond energy about all the atomic bonds, *i, j, k* label the atoms of the system, r_{ij} is the length of the *ij* bond, b_{ij} is the bond order term, θ_{ijk} is the bond angle between the bonds *ij* and *ik* (as shown in Figure 2.2), f_R represents

a repulsive pair potential, f_A represents an attractive pair potential, f_C merely represents a smooth cut-off function to limit the range of the potential, and ζ_{ij} counts the number of other bonds to atom *i* besides the *ij* bond. The parameter values are shown in Table 2.2.

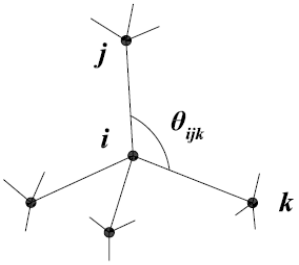

Figure 2.2 The bond angle in crystals.

Table 2.2 Tersoff potential parameters for silicon.

A_t(eV)	1.8308×10^{3}
B_t (eV)	4.7118×10^{2}
λ_t (nm^{-1})	24.799
μ_t (nm^{-1})	17.322
β_t	1.1000×10^{-6}
n_t	7.8734×10^{-1}
c_t	1.0039×10^{5}
d_t	1.6217×10^{1}
h_t	-5.9825×10^{-1}
R_t (nm)	0.27
S_t (nm)	0.30

2.2.3 Force and Acceleration

By differentiating the potential energy (Frenkel and Smit, 2002), the interaction force can be obtained. For example, based on the Tersoff potential, the interaction force between silicon atoms is given by:

$$F_{ijx} = -\frac{\partial V_{ij}}{\partial x_i} = -[\frac{\partial f_C}{\partial x_i}(f_R + b_{ij} f_A) + f_C(\frac{\partial f_R}{\partial x_i} + b_{ij}\frac{\partial f_A}{\partial x_i} + \frac{\partial b_{ij}}{\partial x_i} f_A)] \tag{2.10}$$

$$\frac{\partial f_R}{\partial x_i} = -\lambda_t f_R(r_{ij})\frac{x_i - x_j}{r_{ij}}, \quad \frac{\partial f_A}{\partial x_i} = -\mu_t f_A(r_{ij})\frac{x_i - x_j}{r_{ij}}, \tag{2.11}$$

$$\frac{\partial f_C}{\partial x_i} = \begin{cases} 0, \ r_{ij} < R_t \\ -\dfrac{\pi}{2(S_t - R_t)}\sin[\pi(r_{ij} - R_t)/(S_t - R_t)]\dfrac{x_i - x_j}{r_{ij}}, \ R_t < r_{ij} < S_t . \\ 0, \ r_{ij} > S_t \end{cases} \tag{2.12}$$

where F_{ijx} is the interaction force acting on the ith atom by the jth atom in the x direction, and x_i indicates the ith atom's coordinate in the x direction. Similarly, F_{ijy} and F_{ijz} can be obtained.

The resultant force F_{ix} on the ith atom in the x direction is given by the sum of all the forces arising from the interactions with every other atom,

$$F_{ix} = \sum_{j=1, j\neq i}^{N} F_{ijx} . \tag{2.13}$$

In the simulation, atom motion should follow the Newton's equation of motion,

$$a_{ix} = \frac{d^2 x_i}{dt^2} = \frac{F_{ix}}{m_i}, \tag{2.14}$$

where a_{ix} represents the ith atom's acceleration in the x direction, m_i is the mass of the ith atom.

2.2.4 Finite-Difference Method

A standard method for solution of ordinary differential equations, such as Eqs. (2.10) and (2.14), is the finite difference approach. The general idea is that the atom's new position can be obtained by integrating the ordinary difference equations. Then, from the new position of atoms, the new resultant force acting on every atom, acceleration and new velocity can be determined. Based on this, next movement of every atom can also be determined.

(1) Runge-Kutta (RK) algorithm

Of the large number of finite-difference methods that can be devised, the most commonly used are the Runge-Kutta (RK) methods (Press et al., 1986). These methods have the structure of Euler's method. Runge-Kutta methods generally have good stability characteristics; nevertheless, they have been little used in MD because, for large numbers of molecules, the RK algorithms are too slow, however, in MD the evaluation of interatomic forces is by far the most time consuming calculation.

(2) Verlet's algorithm

The simplest finite-difference method that has been widely used in MD is the Verlet's method (Verlet, 1967). The algorithm is a combination of two Taylor expressions, combined as follows. First write the Taylor series for position from time t to $t + \Delta t$:

$$x(t+\Delta t) = x(t) + \frac{dx(t)}{dt}\Delta t + \frac{1}{2}\frac{d^2x(t)}{dt^2}\Delta t^2 + \frac{1}{3!}\frac{d^3x(t)}{dt^3}\Delta t^3 + O\left(\Delta t^4\right). \tag{2.15}$$

Then write the Taylor series from t back to $t - \Delta t$:

$$x(t-\Delta t) = x(t) - \frac{dx(t)}{dt}\Delta t + \frac{1}{2}\frac{d^2x(t)}{dt^2}\Delta t^2 - \frac{1}{3!}\frac{d^3x(t)}{dt^3}\Delta t^3 + O\left(\Delta t^4\right). \tag{2.16}$$

Adding these two expansions eliminates all odd-order terms, leaving

$$x(t+\Delta t) = 2x(t) - x(t-\Delta t) + \frac{d^2x(t)}{dt^2}\Delta t^2 + O\left(\Delta t^4\right). \tag{2.17}$$

This is Verlet's algorithm for positions, It has a local truncation error that varies as $(\Delta t)^4$ and hence is third order. Nor dose Eq. (2.17) for positions involve any function of velocities; the acceleration in Eq. (2.17) is obtained in Eq.(2.14). To estimate the velocities, Verlet used the first order central difference estimator

$$\upsilon(t) \approx \frac{x(t+\Delta t) - x(t-\Delta t)}{2\Delta t}. \tag{2.18}$$

The Verlet algorithm offers the virtues of simplicity and good stability for moderately large time steps. In its original form it treated velocities as less important than positions- a view in conflict with the attitude that the phase-space trajectory depends equally on positions and velocities. Modern formulations (Beeman, 1976; Swope et al., 1982) of the method try to overcome this asymmetric view.

(3) Gear's Predictor-Corrector Algorithm

Predictor-corrector algorithms were first introduced into MD by Rahman (1964).Those commonly used in MD are often taken from the collection of methods devised by Gear (1971). Here, the fifth-order Gear's predictor-corrector algorithm is introduced. The Gear's predictor-corrector algorithm consists of following three steps:

Predictor: from the positions and their time derivatives up to a certain order q (In the fifth-order Gear predictor-corrector algorithm, $q=5$), all known at time t , one "predicts" the same quantities at time $t+\Delta t$ by means of a Taylor expansion:

$$x(t+\Delta t)=x(t)+\dot{x}(t)\Delta t+\ddot{x}(t)\frac{\Delta t^2}{2!}+x^{(iii)}(t)\frac{\Delta t^3}{3!}+x^{(iv)}(t)\frac{\Delta t^4}{4!}+x^{(v)}(t)\frac{\Delta t^5}{5!}, \tag{2.19}$$

$$\dot{x}(t+\Delta t)=\dot{x}(t)+\ddot{x}(t)\Delta t+x^{(iii)}(t)\frac{\Delta t^2}{2!}+x^{(iv)}(t)\frac{\Delta t^3}{3!}+x^{(v)}(t)\frac{\Delta t^4}{4!}, \tag{2.20}$$

$$\ddot{x}(t+\Delta t)=\ddot{x}(t)+x^{(iii)}(t)\Delta t+x^{(iv)}(t)\frac{\Delta t^2}{2!}+x^{(v)}(t)\frac{\Delta t^3}{3!}, \tag{2.21}$$

$$x^{(iii)}(t+\Delta t)=x^{(iii)}(t)+x^{(iv)}(t)\Delta t+x^{(v)}(t)\frac{\Delta t^2}{2!}, \tag{2.22}$$

$$x^{(iv)}(t+\Delta t)=x^{(iv)}(t)+x^{(v)}(t)\Delta t, \tag{2.23}$$

$$x^{(v)}(t+\Delta t)=x^{(v)}(t). \tag{2.24}$$

Force evaluation: the force is computed taking the gradient of the potential at the predicted positions. The resulting acceleration $\ddot{x}$ will be in general different from the "predicted acceleration" $\ddot{x}^P$ and the difference between the two constitutes an "error signal", as follows:

$$\Delta\ddot{x} = \left[\ddot{x}\left(t+\Delta t\right) - \ddot{x}^{P}\left(t+\Delta t\right)\right]. \tag{2.25}$$

Corrector: this error signal is used to "correct" positions and their derivatives. All the corrections are proportional to the error signal; thus,

$$x = x^{P} + \alpha_0 \Delta R2\,, \tag{2.26}$$

$$\dot{x}\Delta t = \dot{x}^{P}\Delta t + \alpha_1 \Delta R2\,, \tag{2.27}$$

$$\frac{\ddot{x}\left(\Delta t\right)^2}{2!} = \frac{\ddot{x}^{P}\left(\Delta t\right)^2}{2!} + \alpha_2 \Delta R2\,, \tag{2.28}$$

$$\frac{x^{(iii)}\left(\Delta t\right)^3}{3!} = \frac{x^{(iii)P}\left(\Delta t\right)^3}{3!} + \alpha_3 \Delta R2\,, \tag{2.29}$$

$$\frac{x^{(iv)}\left(\Delta t\right)^4}{4!} = \frac{x^{(iv)P}\left(\Delta t\right)^4}{4!} + \alpha_4 \Delta R2\,, \tag{2.30}$$

$$\frac{x^{(v)}\left(\Delta t\right)^5}{5!} = \frac{x^{(v)P}\left(\Delta t\right)^5}{5!} + \alpha_5 \Delta R2\,, \tag{2.31}$$

where $\Delta R2 = \dfrac{\Delta\ddot{x}\left(\Delta t\right)^2}{2!}$, (2.32)

$\alpha_0 = 3/16$, $\alpha_1 = 251/360$, $\alpha_2 = 1$, $\alpha_3 = 11/18$, $\alpha_4 = 1/6$, $\alpha_5 = 1/60$. (2.33)

With judicious combinations of predictor and corrector, this algorithm often offers good stability because the corrector step amounts to a feedback mechanism that can dampen instabilities that might be introduced by the predictor. In this study, the Gear's predictor-corrector algorithm is used to integrate Newton's equations of motion.

During integration, the time step Δt needs to be selected. On one hand, the smaller time step size will lead to more practical approach and will increase the integral accuracy, but it is more time-consuming. On the other hand, the larger time step size can simulate longer process. However, it should be noted that the MD integral algorithm becomes unstable at large time step sizes. Generally, there is a suitable time step size when conducting a MD simulation. Physically this time step size should be less than 1% of the smallest vibrational period of an atom in the simulation. The smallest vibrational period depends most strongly on the potential used. If the Tersoff potential is used, the period of silicon atoms is about 84 fs (Zhang and Tanaka, 1999). Therefore, in this study the time step is set as 1 fs, which is reasonable.

2.2.5 Periodic Boundary Condition

MD programs run at extremely small size scale (nm) and time scale (fs) and if the MD model includes a large number of atoms, the computer might not be able to execute the program or there will be taken an extremely long time to finish. So, the size of the system is limited by the available storage of the computer and the speed of execution of the program. In order to reduce the simulation time, the number of atoms in cube of the system cannot be very large. This leads to a problem how the boundary effect of the model can be reduced.

Born and Von Karman (1912) proposed the periodic boundary condition (PBC) to overcome this problem and PBC has been commonly used (Allen and Tildesley, 1986). In PBC, the cubic box of the model is replicated throughout space for an infinite lattice. In the course of the simulation, as a particle moves in the original box, its periodic image in each of the neighboring boxes moves in exactly the same way. Thus,

as a particle leaves the central box, one of its images will enter through the opposite face. There are no walls at the boundary of the central box. A two-dimensional version of such a periodic system is shown in Figure 2.3. The duplicate boxes are labeled A, B, C, etc. As particle 1 moves through a boundary, its images 1A, 1B, etc., move across their corresponding boundaries. The number density in the central box is conserved. It is not necessary to store the coordinates of all the images in simulation, just the particles in the central box. When a particle leaves the box by crossing a boundary, attention may be switched to the image just entering. A similar analogy exists for a three-dimensional periodic system.

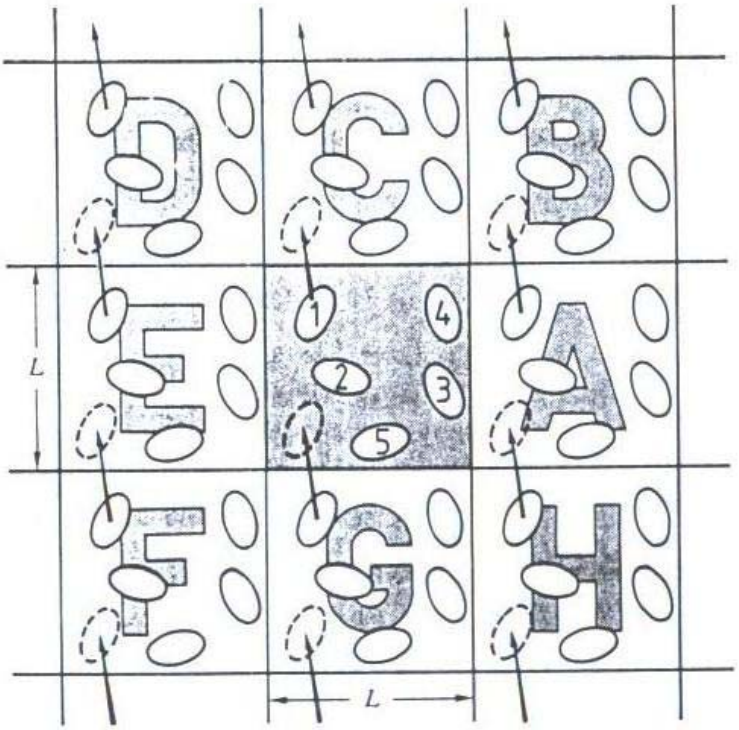

Figure 2.3 A two-dimensional periodic system.

2.2.6 Stress and Temperature

The micro-scopic stress tensor σ, given by (Haile, 1992)

$$\sigma = \begin{bmatrix} \sigma_{xx} & \sigma_{xy} & \sigma_{xz} \\ \sigma_{yx} & \sigma_{yy} & \sigma_{yz} \\ \sigma_{zx} & \sigma_{zy} & \sigma_{zz} \end{bmatrix}. \tag{2.34}$$

In which $\alpha, \beta = x, y, z$ denote Cartesian components and element $\sigma_{\alpha\beta}$ represents the stress on the plane perpendicular to the α direction in the β direction. Actually, $\sigma_{\alpha\beta}$ also measures the rate at which β-directed momentum is transported in the α direction.

Stress is a momentum flux; it's the amount of momentum that crosses a unit area of the surface in unit time. In general, this flux is composed of two parts: (a) the momentum carried by the atoms themselves as they cross the area, and (b) the momentum transferred as a result of forces acting between atoms that lie on different sides of the surface. In the volume V,

$$V\sigma_{\alpha\beta} = \sum_i m_i \upsilon_{i\alpha} \upsilon_{i\beta} + \frac{1}{2} \sum_{i \neq j} r_{ij\beta} F_{ij\alpha} , \tag{2.35}$$

where m_i is the atomic mass, υ_{ia} is the α-component of the velocity of atom i, $r_{ij\beta}$ is the β-component of the bond length r_{ij} separating atoms i and j, and F_{ija} is the α-component of the force exerted on atom i by atom j.

The most obvious prescription (Slawomir, 1994; Schiøtz, 1999; Fabrizio, 2001; Chandra et al., 2004; Zimmerman, 2004; Wu, 2006) to calculate the individual atom of the sum in Eq. (2.35) for the atoms enclosed in volume V:

$$\sigma_{\alpha\beta}^{i}=\frac{1}{\Omega_i}\left(m_i\upsilon_{i\alpha}\upsilon_{i\beta}+\frac{1}{2}\sum_{j,j\neq i}r_{ij\beta}F_{ij\alpha}\right), \tag{2.36}$$

where $\sigma_{\alpha\beta}^{i}$ represents the stress of atom i on the plane perpendicular to the α direction in the β direction, and Ω_i is the Voronoi volume of individual atom i. However, the volume of individual atom is very difficult to calculate and especially at the boundary surface, this value is not determinate. In order to get the stress, a small enough cube with volume V is taken in the crystal and the stresses of all atoms in this cube are considered to be the same. So, the average stress $\sigma_{\alpha\beta}$ is obtained instead of $\sigma_{\alpha\beta}^{i}$,

$$\sigma_{\alpha\beta}=\frac{1}{V}\left(\sum_i m_i\upsilon_{i\alpha}\upsilon_{i\beta}+\frac{1}{2}\sum_{i\neq j}r_{ij\beta}F_{ij\alpha}\right). \tag{2.37}$$

The conversion between the kinetic energy and temperature of atoms follows the equation (Heermann, 1990)

$$\frac{1}{2}\sum_i m_i\upsilon_i^2=\frac{3}{2}Nk_BT, \tag{2.38}$$

where N is the number of atoms, υ_i presents the resultant velocity of the ith atom, k_B is the Boltzmann constant equal to 1.3806503×10^{-23} J/K and T represents the temperature of atoms.

2.3 Molecular Dynamics Model

2.3.1 The Crystal Structure of Silicon

The monocrystalline silicon workpiece is crystallized in the diamond lattice as shown in Figure 2.4, which is a special cubic crystal structure. In the face-centered cubic crystal, atoms are located at the corners and at the face centers. Based on the face-centered cubic crystal, the diamond lattice has four further atoms located inside the lattice. Their centers can be found on the body diagonals at a height of ¼ and ¾ respectively, measured from the base plane. In diamond lattice, the interatomic forces are developed by the covalent bond, and the lattice constant a = 0.543 nm.

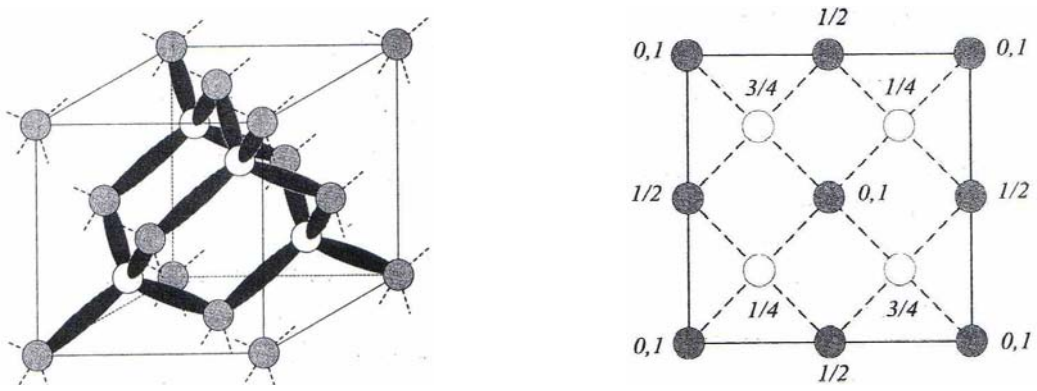

(a) (b)

Figure 2.4 The diamond crystal lattice: (a) spatial illustration with covalent bonding, (b) projection view.

2.3.2 Model

In this study, a three-dimensional MD model has been developed for the nanoscale ductile mode cutting of silicon, as shown in Figure 2.5, where (a) shows a schematic diagram of the MD model, and (b) shows an output of the MD simulation system.

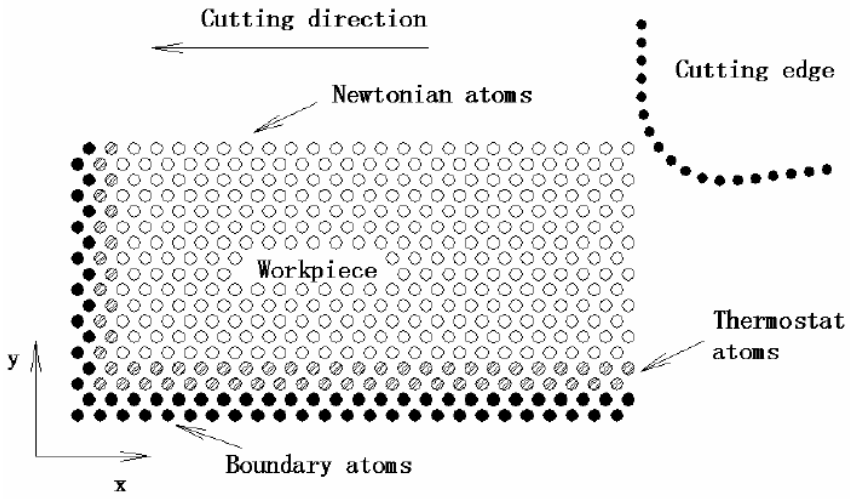

(a)

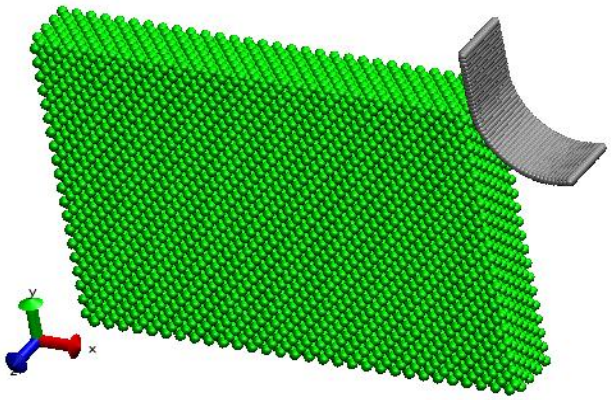

(b)

Figure 2.5 The model for the MD simulation of nanoscale ductile mode cutting of silicon: (a) a schematic of the MD model, (b) an output of the MD simulation system.

In the model, the positions of silicon atoms are arranged according to the crystal structure of silicon. The dimension of the workpiece is $30a \times 20a \times 4a$. Theoretically speaking, when the dimension of the model is larger, the model is more close to the actual workpiece. However, the larger model requires much longer computing time. If the boundary effect is light and can be ignored, the model dimension is suitable to do the simulation. By some computing tests, the dimension $30a \times 20a \times 4a$ is determined for simulation.

The dimension in the z axis direction, $4a$, is small, but the periodical boundary condition is applied to reduce the boundary effect. The x and y axis directions include machining surface, so they are free surfaces and the periodical boundary condition is not applied to them.

According to the solid state physics, every atom is vibrating around the equilibrium position at some temperature. The velocities of all the atoms should satisfy the Maxwell-Boltzmann distribution (Haile, 1992). This simulation is conducted at an absolute temperature T = 293 K. At this temperature, the initial velocities of all the atoms are randomly assigned according to Maxwell-Boltzmann distribution.

The workpiece atoms consist three different atoms: boundary atoms, Newtonian atoms and thermostat atoms. The boundary atoms are fixed in positions to reduce the boundary effects, avoid rigid body motion of the workpiece and maintain the proper symmetry of the lattice. The motion of the Newtonian atoms is determined by the Newton's equation of motion. The thermostat atoms, which are used to simulate the heat conduction, are arranged to surround the Newtonian atoms to make the boundary

temperature close to ambient temperature. The thermostat atoms' movement also should comply with the Newton's equation of motion, but their velocities need to be scaled at some integrating steps, such as 50 steps. For the silicon, the velocity scaling factor is

$$\beta = \left[3Nk_B T \Big/ \sum_i m_i \upsilon_i^2 \right]^{1/2}, \tag{2.39}$$

The diamond cutting tool is assumed to be rigid, that is, the relative positions of tool atoms remain unchanged in the simulation. As mentioned earlier, the tool cutting edge radius can not be ignored, so the carbon atoms are arranged along an arc with a radius of the cutting edge. In the simulation, the cutting velocity is assumed as 20 m/s.

2.4 Molecular Dynamics Simulation System

Based on the MD method and simulation model, a MD simulation system is developed. In this system, the inputs are given to initialize the parameters. After computing, the results can be output. The results can include displacement, velocity, force and other information of all the atoms. Before simulation, the model needs to be relaxed for about 100 time steps to reach equilibrium. Figure 2.6 provides a flow chart of the procedure of the MD simulation system.

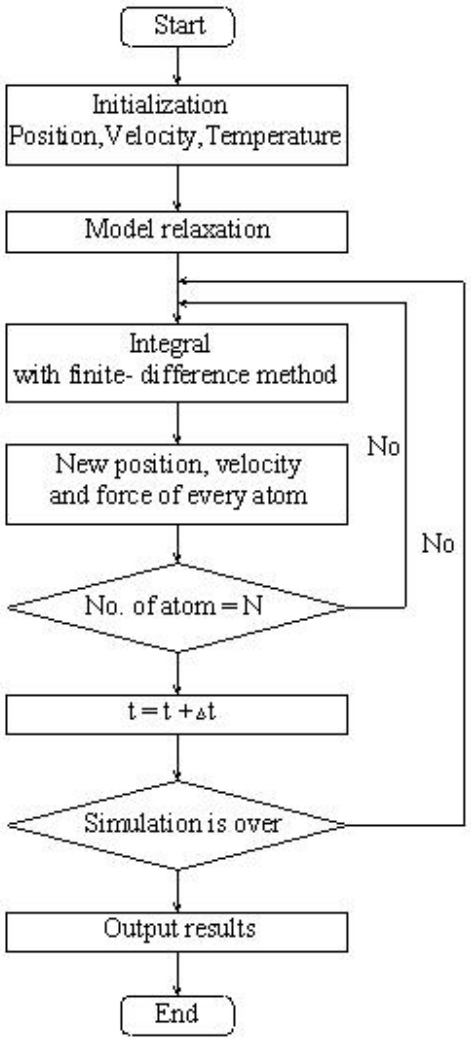

Figure 2.6 Flow chart of the MD simulation system.

2.5 Concluding Remarks

The MD method has been briefly introduced. Based on the MD method, for the simulation of nanoscale ductile mode cutting of the monocrystalline silicon, a realistic molecular dynamics model taking into account the effect of tool cutting edge radius on

the chip formation and cutting characteristics has been developed. In this model, the initial atom positions of silicon workpiece material are arranged according to the crystal lattice structure, the atomic interactive actions of silicon are based on the Tersoff potential, the diamond cutting tool is assumed to be undeformable, and the motions of the atoms in the chip formation zone are determined by Newton's equation of motion. A simulation system for nanoscale ductile mode cutting of monocrystalline silicon is developed using this MD model.

Chapter 3

Experimental Setup and Procedure

3.1 Introduction

The molecular dynamics (MD) simulation is used to study the nanoscale ductile mode cutting of monocrystalline silicon. In order to observe the phenomenon of ductile mode cutting, provide the basis of MD study, and verify the MD simulation, experiments of nanoscale ductile mode cutting of monocrystalline silicon wafer with diamond tools were conducted. In this chapter, the experimental details, including experimental materials, experimental equipment, and procedure are introduced.

3.2 Experimental Materials

3.2.1 Workpiece Material

Monocrystalline silicon wafers with the surface crystallographic orientation <100> having lapped and polished finishes were used as workpiece materials. Each wafer is 100 mm in diameter and 0.5 mm in thickness. The wafers were mounted on prefaced aluminium blanks using a heat softening glue.

3.2.2 Cutting Tool

Round-nosed monocrystalline diamond cutting inserts which had the same tool geometry were used in the experiments. Tools used in diamond turning are made in variety of configurations using a variety of diamond types. Monocrystalline or polycrystalline, natural or synthetic, diamond tools are preferred in many applications because of their strength and abrasion resistance. Monocrystalline tools can be polished to an extremely fine edge that can generate high precision finishes when removing a small amount of workpiece material. Figure 3.1 shows a typical monocrystalline diamond cutting insert with a round nose. These tools had 0.5 mm nose radius, 0° nominal rake angles and 7° relief angles.

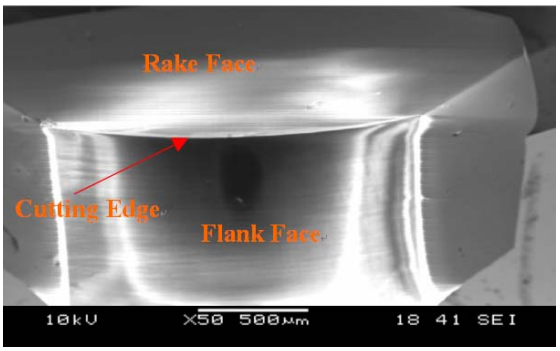

Figure 3.1 SEM examination of a diamond cuter.

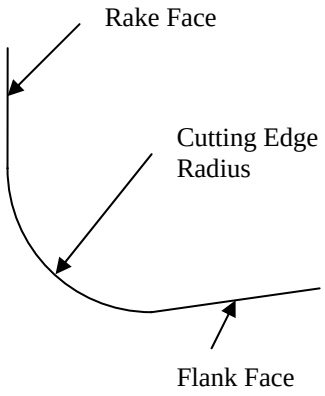

Figure 3.2 The schematic of the cutting edge radius.

Before cutting, the cutting edge radii of all tools, as shown in Figure 3.2, were measured by indentation tests on the surface of a copper material. In the non-destructive nano-precision measurement (Li et al., 2003), the profile of the tool cutting edge is copied into the copper material and then the indentation piece is measured at nano-precision level using an AFM (SPA500). Copper is selected as the indentation material due to its high ductility and high density, large Young's modulus, and low yield strength. The elastic error compensation coefficient for copper material is determined by comparing the actual value and the measured value of tool cutting edge. As far as the elastic error compensation coefficient is consistent with the copper material used, the only source of errors with the measurement will come from the analysis instrument.

3.3 Experimental Equipment and Procedure

3.3.1 Toshiba Ultra Precision Lathe (ULG-100)

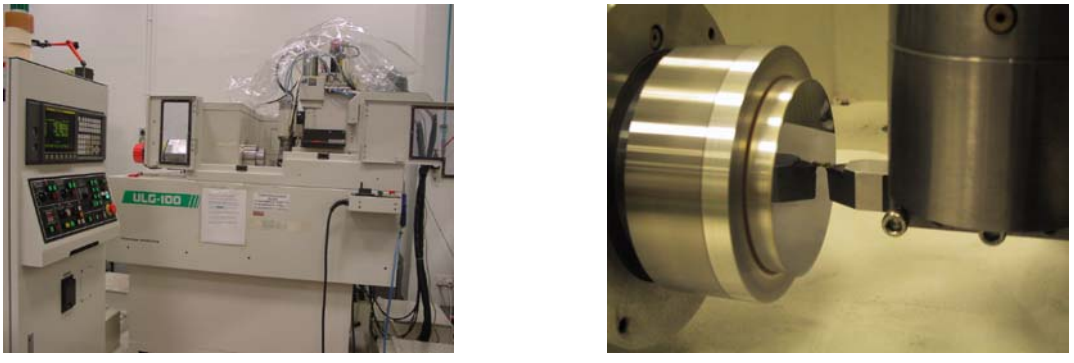

(a) (b)

Figure 3.3 The nanoscale cutting of silicon: (a) Toshiba ULG-100C ultraprecision machine; (b) the cutting operation.

The cutting tests were carried out on the ULG-100 Toshiba Ultra-precision Machine (as shown in Figure 3.3) having a feed resolution of 1 nm. The maximum spindle speed and feed of this machine is 1500 rev/min and 450 mm/min respectively. A high precision aerostatic bearing spindle improved rigidity and stability at different speeds. Inaccuracies caused by hydrostatic thermal displacement are eliminated with the rigid aerostatically preloaded V-V roller guideways. The temperature and vibration proof environment using four air mounts set under the machine base enhances accuracies and eliminates errors induced by vibrations and thermal fluctuation.

3.3.2 Examining Equipment

The Keyence Microscope, shown in Figure 3.4 is a fully integrated microscope with an 18 million CCD camera was used to observe the surface of the silicon wafer surface finish after it is cut with the diamond cutter.

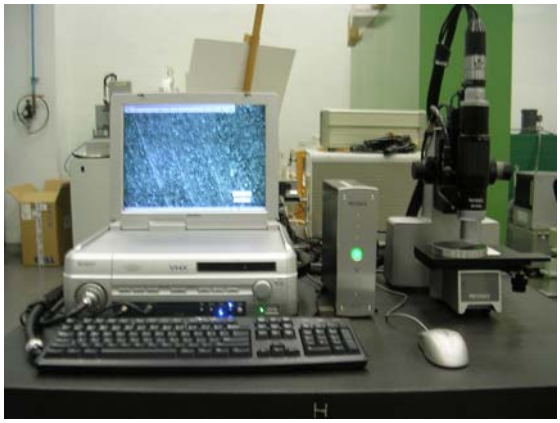

Figure 3.4 Keyence Microscope.

The JEOL JSM-5500 Scanning Electron Microscope (SEM), shown in Figure 3.5 is an easily operable SEM equipped with electron optics, specimen chamber and stage for high magnification observation and imaging of specimens.

Figure 3.5 JEOL JSM-5500 Scanning Electron Microscope.

The atomic force microscope (AFM), shown in Figure 3.6 was used to measure the cutting edge radius of the monocrystalline diamond cutter by inspecting the indentation of the diamond cutter onto the copper blocks. The copy of the profile was measured at nano precision level by analyzing it using the AFM.

Figure 3.6 Atomic Force Microscope (SPA-500).

Figure 3.7 shows the schematic diagram of cutting force measurement system. A three-component piezoelectric dynamometer (Kistler 9256A1) was mounted on the tool

holder post to measure the three orthogonal force components, namely the feed force F_f, the cutting force F_c and the thrust force F_t. Force signals were amplified by a charge amplifier (Kistler 5015) and then recorded onto a cassette by a digital recorder (Sony PC204Ax). They were downloaded and monitored simultaneously by software (PC Scan II) onto a computer. The cutting forces, therefore, can be processed and tabulated using Mircrosoft Excel.

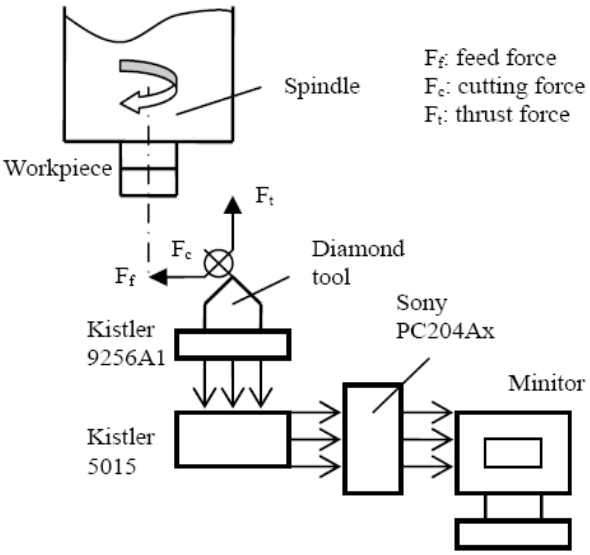

Figure 3.7 Schematic diagram of cutting force measurement system.

Chapter 4

Effects of Tool Edge Radius and Cutting Direction on Ductile Mode Cutting

4.1 Introduction

Unlike in conventional cutting where the undeformed chip thickness is significant compared to the cutting tool edge radius, in nanoscale cutting process, the undeformed chip thickness is very small. Therefore, the tool edge radius can not be ignored. MD was employed to simulate the ductile cutting of monocrystalline silicon. Different cutting tool edge radii were applied to simulate the cutting process. Furthermore, an experiment was conducted to verify the MD model. The simulated variation of the cutting forces with the tool cutting edge radius was compared with the cutting force results obtained from experimental cutting tests. The good agreement of results indicated that the present MD model and simulation system can be used for simulation of the nanoscale ductile mode cutting of silicon. The MD simulation results showed that in nanoscale ductile mode cutting of silicon the thrust force is much larger than the cutting force. The results also denoted that the resultant force in the cutting process is not uniformly distributed along the cutting tool edge. In the simulation, elastic spring-back of small thickness was observed on the machined workpiece surface.

In this chapter, the effects of cutting direction on the cutting forces and deformation of workpiece in ductile mode cutting also have been studied. Three different cutting directions were used in the MD simulation. The results showed that the cutting direction has no obvious effects on the ductile mode cutting of silicon.

4.2 MD Simulation Condition

In this simulation of nanoscale ductile cutting of monocrystalline silicon, the dimensions of the silicon workpiece were $30a \times 20a \times 4a$. The working environment temperature was set to 293 K. The simulation time step was set to 1 fs. The cutting speed was set to 20 m/s.

In the study of effects of tool cutting edge radius, the undeformed chip thickness a_c was set to 2.0 nm and the values of radius R of cutting tool edge were 2.5 nm, 3.0 nm, 4 nm and 5 nm respectively. Therefore, the undeformed chip thickness was always less than the tool cutting edge radius.

In the study of the effects of cutting direction, the tool cutting edge radius R and undeformed chip thickness a_c were 2.5 nm and 2.0 nm, respectively. Three different cutting directions [100], [101] and [001] were used in the simulation.

4.3 Effects of Tool Cutting Edge Radius

4.3.1 Simulated Cutting Forces with Experimental Verification

An output of the MD simulation of nanoscale ductile mode cutting of monocrystalline silicon is shown in Figure 4.1, where a_c is the undeformed chip thickness, d_s denotes the spring-back thickness of the finished surface, and d_a denotes the affected zone thickness of the tool edge, respectively.

The simulated results are shown in Table 4.1, where R denotes the radius of the tool cutting edge, F_c and F_t denote the cutting force in the cutting direction and the thrust force perpendicular to the cutting direction, respectively. a_c, R, F_c and F_t are shown in Figure 4.2.

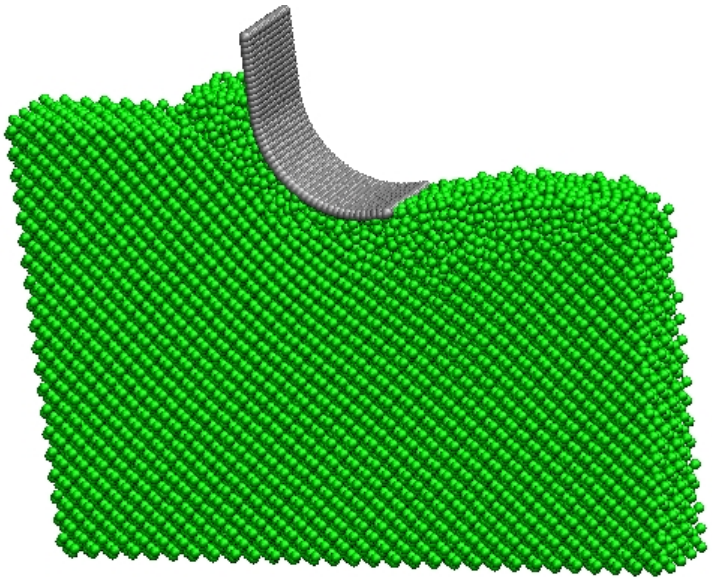

(a)

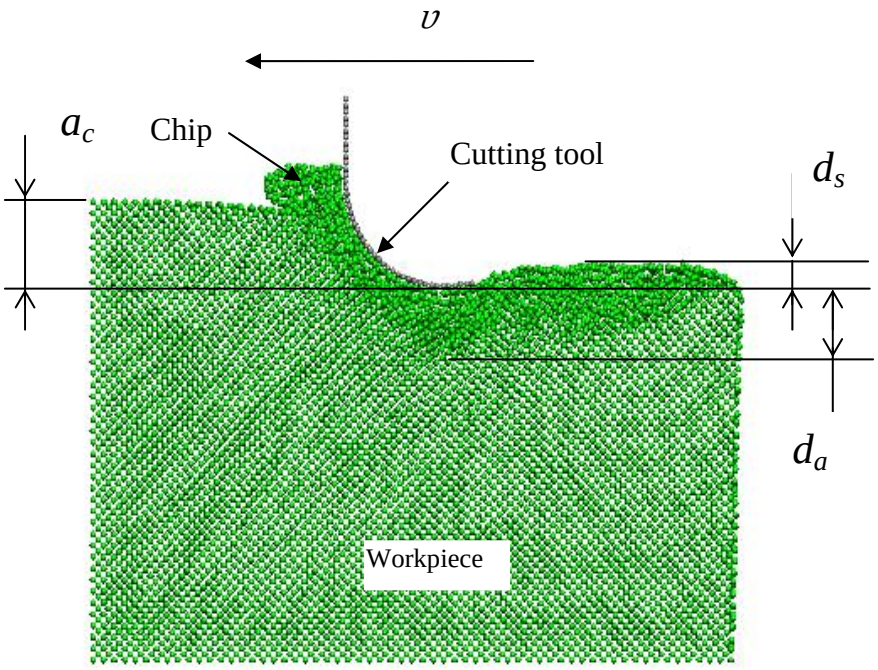

(b)

Figure 4.1 An output of the MD simulation of nanoscale ductile cutting: (a) a 3-D output of the results, (b) the output is shown in a 2-D plan.

Table 4.1 The MD simulated results for a_c = 2 nm.

R (nm)	F_c (10^{-9}N)	F_t (10^{-9}N)	d_s (nm)	d_a (nm)
2.5	70	130	0.6198	1.4394
3.0	83.1	188.8	0.6268	1.7990
4.0	102.4	226.1	0.5643	1.9773
5.0	100.1	260.5	0.5940	2.2899

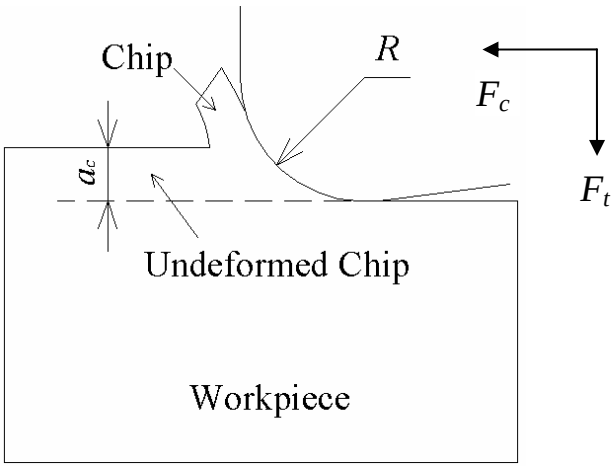

Figure 4.2 The cutting force components, F_t and F_c, acting on the cutting tool.

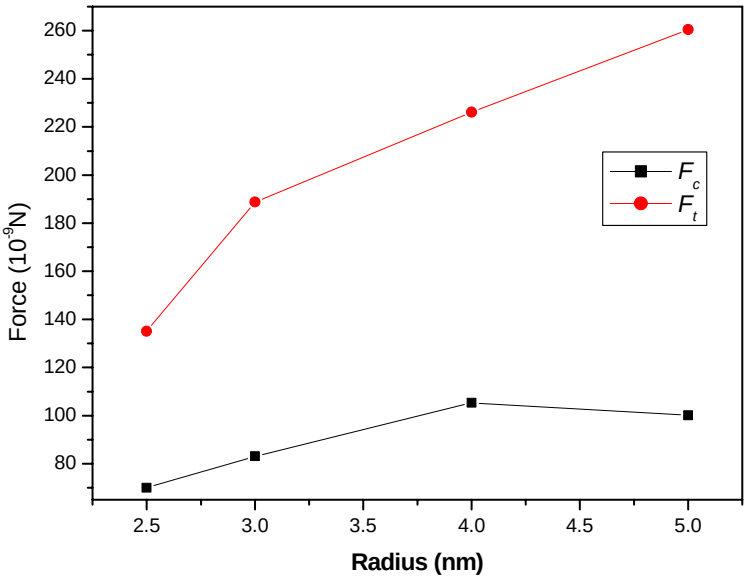

Figure 4.3 The MD simulated cutting forces acting on the cutting tool.

Figure 4.3 shows the MD simulated cutting forces versus cutting edge radius. From this figure, three obvious features can be observed.

1) The thrust force is much larger than the cutting force during cutting, which is different from that in conventional cutting, where the cutting force is generally greater than the thrust force and the tool cutting edge radius is far smaller than the undeformed chip thickness.

2) The cutting force exhibits no significant change as the tool edge radius increases with the undeformed chip thickness fixed.

3) Unlike the cutting force, the thrust force changes significantly. The thrust force obviously increases as the cutting tool edge radius is increased.

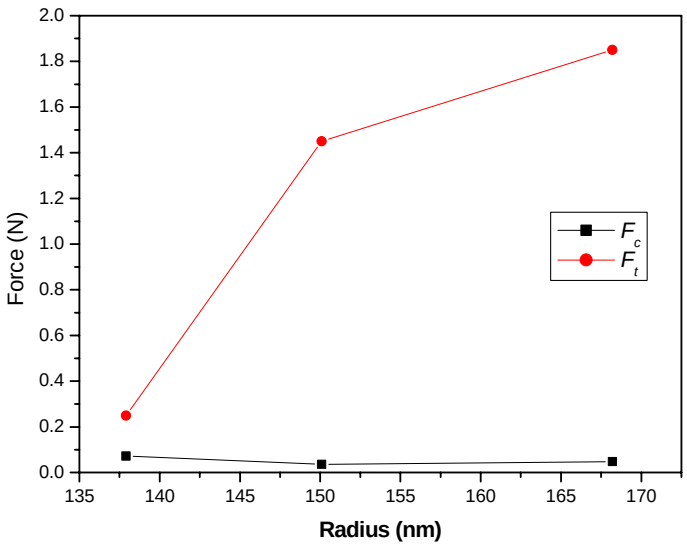

Figure 4.4 Forces acting on the cutting tool in the experiment.

In the experiment, four diamond tools of different cutting edge radii were applied and cuts in ductile mode were conducted (feed rate was 300 nm/rev and rotation rate was 1000 rpm). The cutting edge radii were 52.7 nm, 71.10 nm, 97.00 nm and 110.10 nm, respectively, and the undeformed chip thickness was fixed at 9.587 nm. The

undeformed chip thickness was set to be smaller than the cutting edge radius to ensure ductile mode cutting conditions. Figure 4.4 shows the mean cutting forces versus cutting edge radius, and Figure 4.5 shows the cutting forces versus cutting time at the undeformed chip thickness 7.730 nm and 9.978 nm, respectively. From Figures 4.4 and 4.5, it can be seen that the three cutting force features observed from the MD simulated results can also be seen in the experimental tests of nanoscale ductile mode cutting of monocrystalline silicon wafer. In Figure 4.5, the oscillation of forces could be caused by the slight vibration of the lathe. Because the thrust force is large, the magnitude of its oscillation is larger than that of the cutting force.

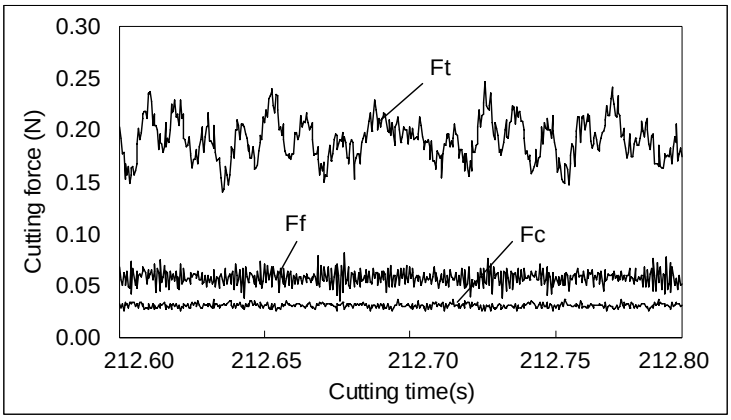

(a)

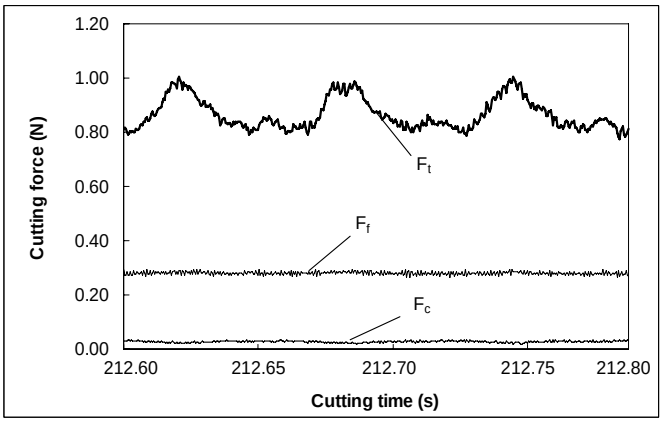

(b)

Figure 4.5 Cutting force components vs. cutting time at undeformed chip thickness (a) 7.730 nm and (b) 9.978 nm.

The good agreement between the MD simulated results and the experimental cutting results for the trends of cutting forces in variation with tool edge radius indicated that the present MD model and simulation system can be used for simulation of the nanoscale ductile mode cutting of silicon. The MD simulation system was then used for further simulation of the effects of the tool cutting edge radius on the workpiece material deformation zone as well as on the material spring-back. The results are shown in the next two subsections.

4.3.2 Effect of Cutting Edge Radius on Workpiece Material Deformation Zone

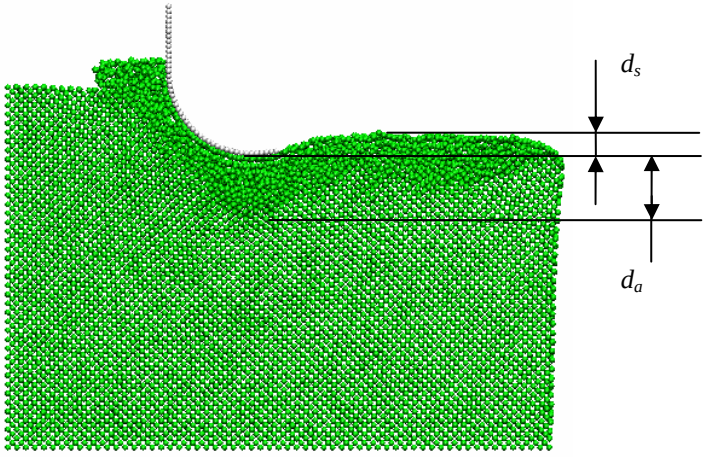

(a)

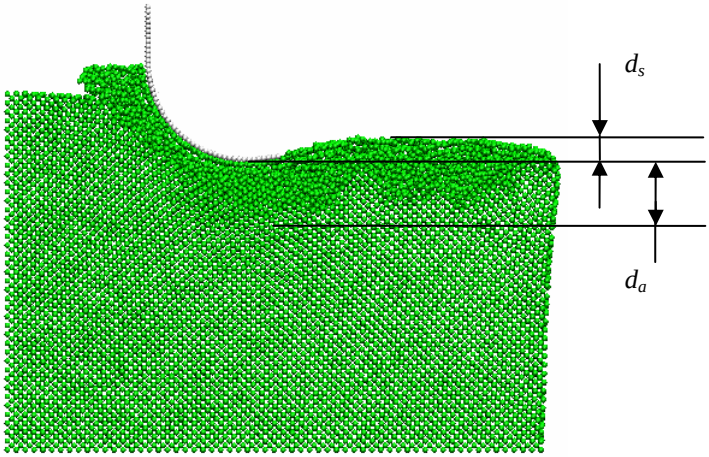

(b)

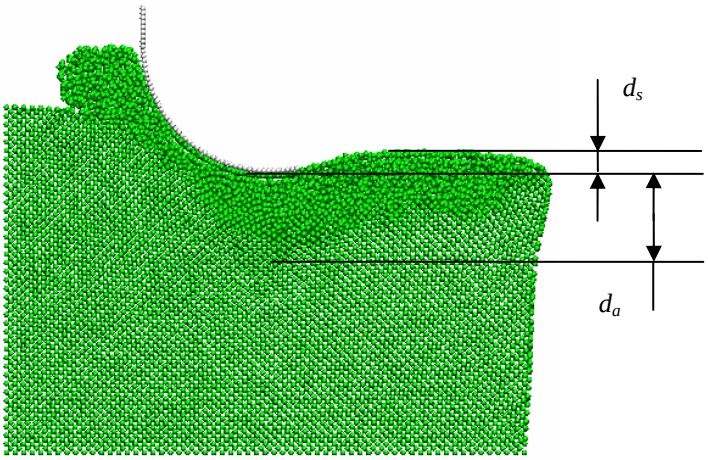

(c)

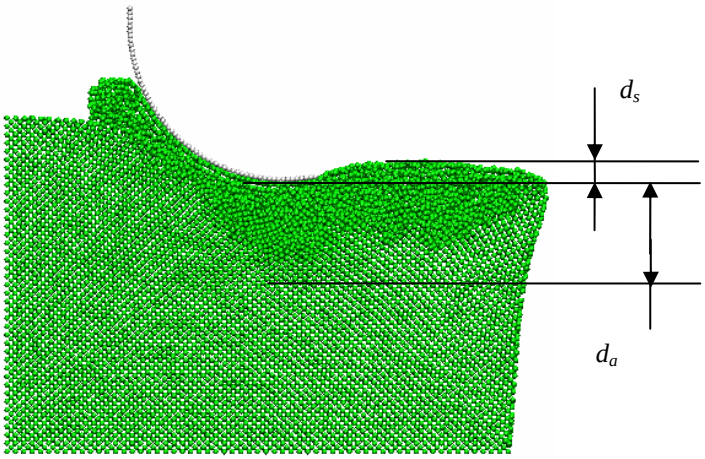

(d)

Figure 4.6 Workpiece material deformation zone varying with the tool cutting edge radius: (a) R = 2.5 nm, (b) R = 3.0 nm, (c) R = 4.0 nm and (d) R = 5.0 nm.

When the tool cuts the workpiece, the material near the cutting edge will be deformed because of compression or tension. Figure 4.6 shows the snapshots of MD simulation of nanoscale ductile mode cutting of silicon at different tool edge radii. From Figures 4.6(a) – (d), the deformed zones or affected zones can be seen clearly. In the affected zones, the lattice structure is different from the original structure. Another important

phenomenon is that along the tool cutting edge, the affected zones are not uniformly distributed. Generally, near the part of tool edge that interfaces with the machined workpiece surface, the affected zone is large. Here, the parameter d_a denotes the affected zone thickness of this large affected zone. This phenomenon denotes that the stress in the cutting process cannot be simply considered to be uniformly distributed along the tool cutting edge.

In Table 4.1, the data of d_a for different tool cutting edge radii are given. It can be found that when undeformed chip thickness is fixed and the cutting edge radius increases, the value of d_a also increases.

Actually, when the cutting edge radius increases, the contact area between cutting tool and machined workpiece also increases. This can be seen clearly in Figure 4.6. At the same time, as mentioned before, the resultant force also increases when the cutting edge radius increases. Therefore, maybe the stress along the cutting edge does not change because of the synchronous increment of resultant force and contact area. However, the increment of d_a denotes that the stress increases faster in this zone than other zones. This further indicates that the resultant force is not uniformly distributed along the cutting tool edge.

4.3.3 Effect of Cutting Edge Radius on Spring-Back of Machined Surface

Silicon as a brittle material should have elastic spring-back when the loading is released after it is deformed under loading. In the MD simulation of nanoscale ductile mode cutting of silicon, the elastic spring-back on the machined workpiece can be seen in Figure 4.6. The data of spring-back thickness is given in Table 4.1. Under the

simulation condition, the spring-back thickness fluctuated by around 0.6 nm. Moreover, the elastic spring-back thickness is smaller compared with the affected zone thickness.

4.4 Effects of Cutting Direction

4.4.1 Different Cutting Directions

In the study of effects of cutting direction, three different cutting directions [100], [101] and [001], as shown in Figure 4.7, were used in the simulation. The silicon crystal structure is regular and these three cutting directions represent the typical cutting directions.

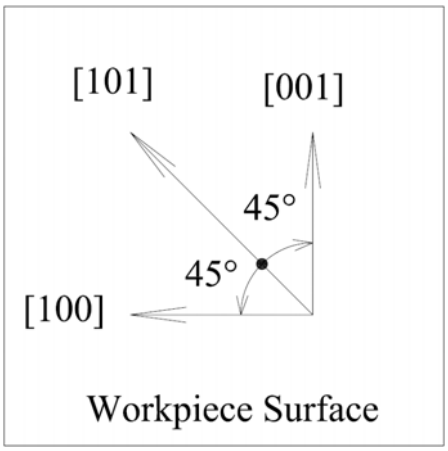

Figure 4.7 Cutting directions in the MD simulation.

4.4.2 Effect of Cutting Direction on Cutting Forces and Workpiece Deformation

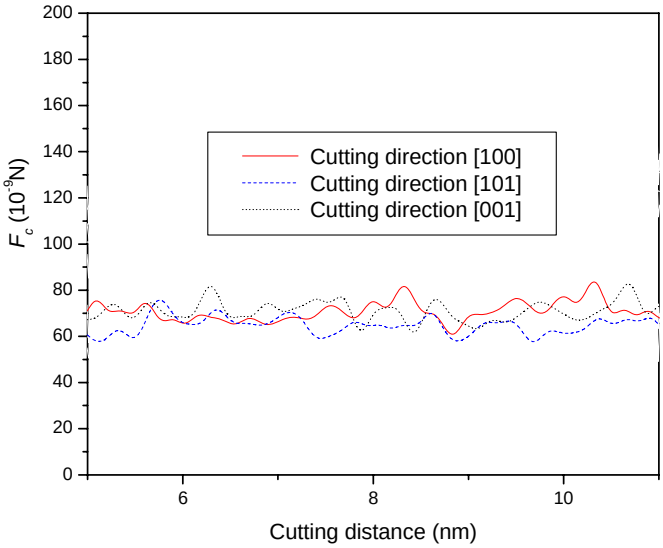

Figure 4.8 The cutting forces in different cutting directions.

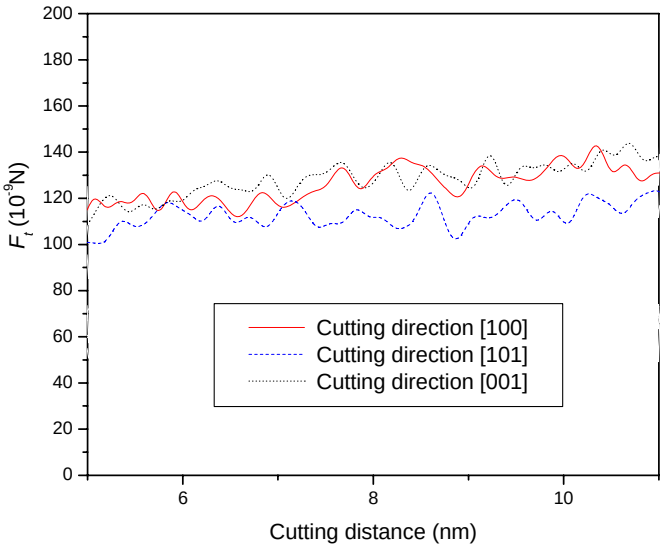

Figure 4.9 The thrust forces in different cutting directions.

Figure 4.8 and Figure 4.9 show the cutting force and thrust force vs. cutting distance in different cutting directions, respectively. From them, it can be seen that for both the cutting force and thrust force, there are nearly no obvious differences among the three different cutting directions.

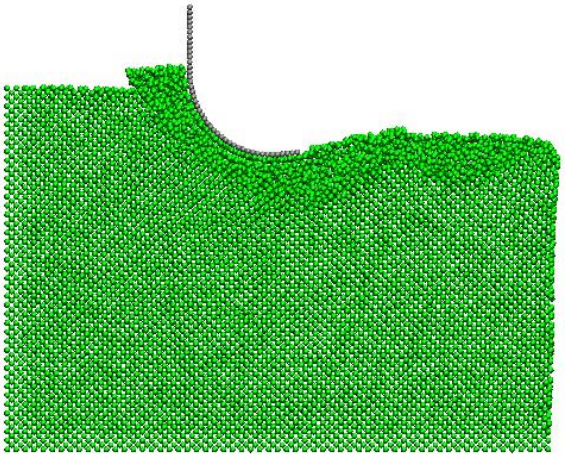

(a)

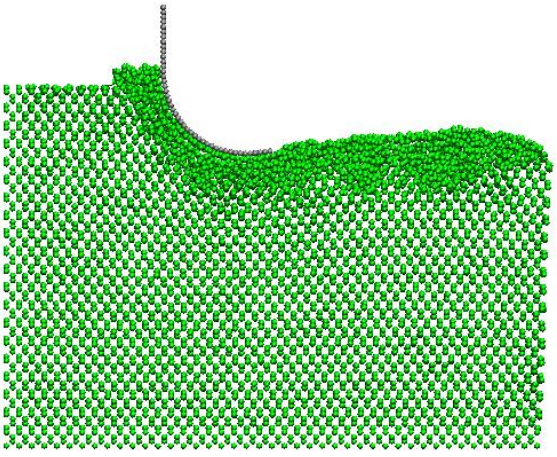

(b)

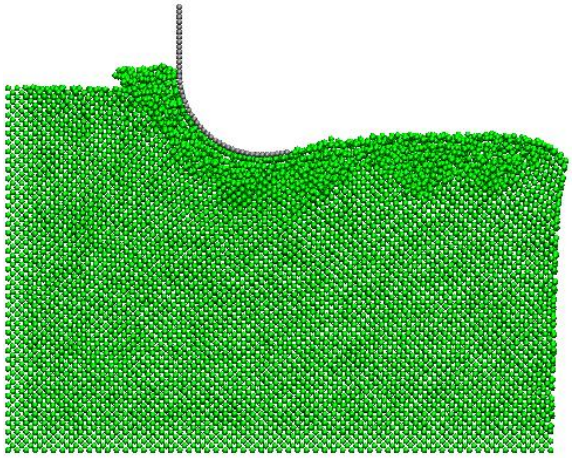

(c)

Figure 4.10 Workpiece material deformation in different cutting direction: (a) [100], (b) [101] and (c) [001].

Table 4.2 The MD simulated results for different cutting directions.

Cutting Direction	d_s (nm)	d_a (nm)
[100]	0.6198	1.4394
[101]	0.6167	1.4779
[001]	0.6231	1.4187

Figure 10 shows the workpiece material deformation in different cutting directions: (a) [100], (b) [101] and (c) [001], and Table 4.2 shows the affected zone thickness of tool edge and the spring-back thickness of finished surface corresponding to the deformations in different cutting directions. From them, the obvious differences among the results of different cutting directions still cannot be found, and the deformation

profiles of workpiece in different cutting directions are nearly the same. Therefore, the cutting direction has no obvious effect on the cutting forces and deformation of workpiece in nanoscale ductile mode cutting of silicon. This is understandable and in the experimental tests, the cutting directions are normally considered as having no effect on the ductile mode cutting, because in the turning test, the cutting direction is always changing with the rotation of the spindle, but the good surface obtained is independent of the direction on the machined surface. From another viewpoint, the ductile chip formation is caused by the high pressure induced phase transformation, which should be independent of the cutting direction. As a result, the ductile mode cutting is independent of the cutting direction. The mechanism of ductile chip formation in nanoscale ductile mode cutting of silicon will be presented in Chapter 5.

4.5 Concluding Remarks

In this chapter, MD method has been used to simulate nanoscale ductile mode cutting of single crystal silicon. The effect of tool edge radius and cutting direction on the cutting forces, workpiece material deformation zone, and machined surface spring-back in nanoscale ductile cutting of silicon are investigated. Some tentative conclusions can be drawn as follows:

1) The MD simulation showed that the thrust force is much larger than the cutting force in cutting. When the tool cutting edge radius increases and the undeformed chip thickness is fixed, both cutting force and thrust force increase. However, the increase of thrust force is much greater than that of cutting force.

2) The good agreement between the MD simulated results and the experimental cutting results for the trends in the cutting forces as they vary with tool edge radius indicated that the present MD model and simulation system can be used for simulation of the nanoscale ductile mode cutting of silicon.

3) The simulated results denoted that the stress in the cutting process is not uniformly distributed along the cutting tool edge. As the cutting edge radius increases, the affected zone thickness near the part of tool edge interfaced with the machined workpiece surface increases.

4) In nanoscale ductile cutting of silicon, there is an elastic spring-back zone of very small thickness on the machined workpiece surface.

5) The cutting direction has no obvious effects on the cutting forces and deformation of workpiece in the nanoscale ductile mode cutting of silicon.

Chapter 5

Mechanism of Ductile Chip Formation

5.1 Introduction

In nanoscale cutting of silicon wafer, it has been found that under certain conditions ductile mode chip formation can be achieved. However, the mechanism of ductile chip formation has not been adequately explained. In order to understand the mechanism of the ductile chip formation, molecular dynamics (MD) simulations have been conducted to study the phase transformation in ductile cutting of monocrystalline silicon. The results of MD simulations of nanoscale cutting of silicon showed that because of the high hydrostatic pressure in the chip formation zone, there is a phase transformation of the monocrytslline silicon from diamond cubic structure to both β silicon and amorphous phase in the chip formation zone, which results in plastic deformation of the work material in the chip formation zone as observed in experiments. The results further showed that although from experimental observation the plastic deformation in the ductile mode cutting of silicon is similar to that in cutting of ductile materials, such as aluminum, in ductile mode cutting of silicon it is the phase transformation of silicon rather than atomic dislocation that results in the plastic deformation.

5.2 MD Simulation Condition

In this simulation for the nanoscale ductile cutting of monocrystalline silicon, the dimensions of the silicon workpiece used were $30a \times 20a \times 4a$. For the simulation of nanoscale cutting of aluminum, the dimensions of the workpiece used were $80b \times 26b \times 5b$, where b, i.e., the lattice constant of aluminum, is equal to 0.405 nm. The working environment temperature was set at 293 K and the integration time step was set at 1 fs. The cutting speed was set at 20 m/s.

In the simulation of nanoscale cutting of silicon, the tool cutting edge radius was R = 3.5 nm and the undeformed chip thicknesses was a_c = 2.8 nm ($a_c < R$). For the simulation of nanoscale cutting of aluminum, the tool cutting edge radius was fixed at R = 2.5 nm and two cuts also were performed at the undeformed chip thicknesses of $a_c < R$ (a_c = 2.0 nm) and $a_c > R$ (a_c = 3.0 nm).

5.3 Results and Discussion

5.3.1 The Phase Transformation of Silicon Workpiece Material

Figure 5.1 shows the workpiece deformation from the simulation of nanoscale cutting of silicon under the undeformed chip thicknesses a_c = 2.8 and the tool cutting edge radius R = 3.5 nm. According to previous research (Liu and Li, 2001), when the undeformed chip thickness is smaller than the tool cutting edge radius, ductile mode cutting can be achieved. Therefore, Figure 5.1 should show evidence of ductile mode

cutting. From Figure 5.1, it can be seen that along the tool cutting edge in the chip formation zone, the silicon workpiece material has large deformation.

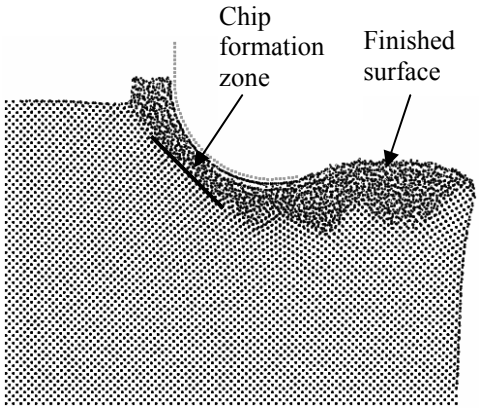

Figure 5.1 The silicon workpiece deformation when the tool cutting edge radius R = 3.5 nm and the undeformed chip thickness was a_c = 2.8 nm.

In this deformation zone, the interatomic bond length has been studied. Figure 5.2(a) shows the distribution frequencies of interatomic bond lengths of the silicon workpiece at different cutting distances in the chip formation zone in comparison to that in the undeformed workpiece material. It can be seen that in the undeformed workpiece material, the distribution of interatomic bond length concentrates near the value of bond length L = 2.35 Å. This denotes that the atoms were vibrating at the equilibrium positions in the simulation and the bond length was 2.35 Å, which is consistent with theoretical value of the length of covalent bond between the atoms in silicon. However, in the chip formation zone the interatomic bond length varies in a wide range, and this indicates the existence of the amorphous phase in this zone. Also, two peaks of the curves in the chip formation zone can be observed and they correspond to the interatomic bond length values 2.455 Å and 2.61 Å. This indicates that there was a phase transformation from diamond cubic structure to β silicon in the chip formation zone. The result of simulation of nanoscale indentation using MD method showed that

during indentation the average atomic distance between the atoms that have undergone transformation changed from 2.35 Å (diamond cubic structure) to 2.43 and 2.58 Å (β silicon) (Cheong and Zhang, 2000). In this study, 2.455 Å and 2.61 Å are a little larger than 2.43 Å and 2.58 Å, respectively, which is because the workpiece material continues flowing out in the chip formation zone, but the workpiece material does not come out in the indentation simulation. Moreover, from Figure 5.2(a), it can be seen that most of the bond lengths in the chip formation zone become longer than the normal bond length in the undeformed silicon workpiece material. Figure 5.2(b) shows the distribution frequency of interatomic bond lengths of the silicon workpiece material near the finished surface in comparison to that in the undeformed workpiece material. It can be seen that near the finished surface, the interatomic bond length varies in a wide range, and there are no peak values corresponding to special lattice structure of silicon, indicating that the structure in this zone should be amorphous. So, in the ductile mode cutting of silicon, there was a phase transformation from diamond cubic structure to β silicon and amorphous phase in the chip formation zone, and the phase near the finished surface was amorphous.

The material phase transformation could be caused by the high hydrostatic pressure in the chip formation zone near the tool cutting edge. It has been reported that at a hydrostatic pressure of 10-13 GPa silicon undergoes phase transformation from diamond cubic structure to β silicon and amorphous (Needs and Mujica, 1995; Zhang and Tanaka, 1999; Cheong and Zhang, 2000; Ruffell et al, 2006; Rao et al, 2007). According to the results from the present simulation, the average hydrostatic pressure was around 12 GPa. Therefore, it is possible that phase transformation took place in the chip formation zone. Moreover, due to the release of compressive stress in the

finished surface, the structure of workpiece material near the finished surface became amorphous (Cheong and Zhang, 2000).

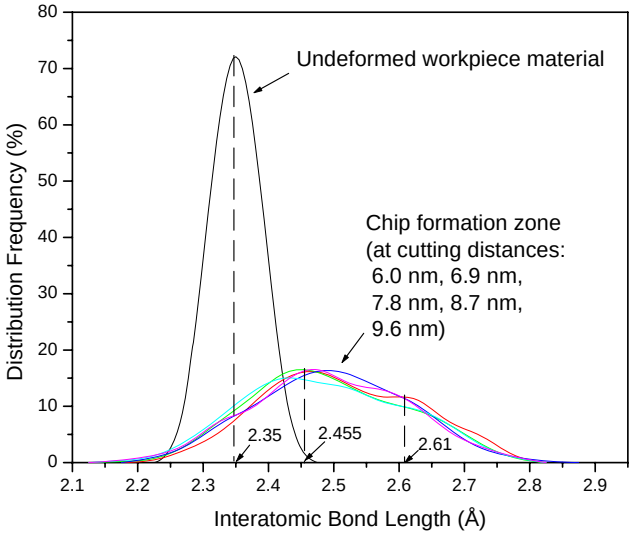

(a)

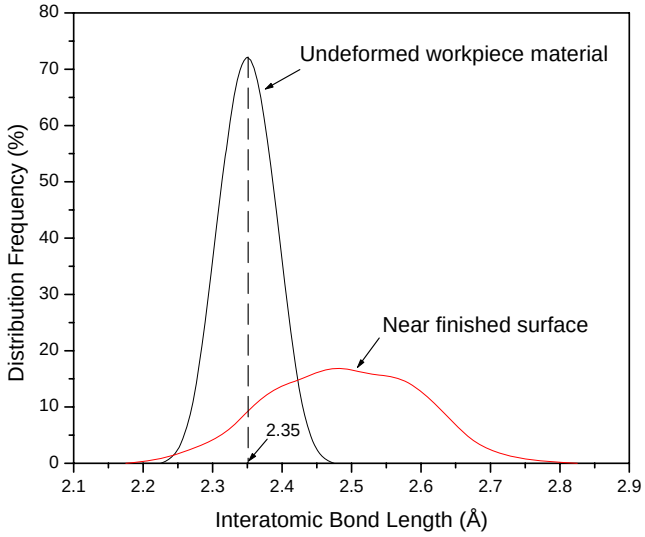

(b)

Figure 5.2 The comparisons of distribution frequency of interatomic bond length in the undeformed silicon workpiece material with those (a) in the chip formation zone at different cutting distances and (b) near the finished workpiece surface.

5.3.2 The Chip Formation in Nanoscale Ductile Mode Cutting of Silicon

Two sets of experimental tests of nanoscale cutting of monocrystalline silicon wafer with monocrystalline diamond tool were conducted. The cutting tests were carried out on the ULG-100 Toshiba Ultra-precision Machine. The tool rake angle and relief angle were 0° and 7°, respectively. In the first test, the tool cutting edge radius R was 30 nm and the undeformed chip thickness a_c was 7.73 nm. In the second one, the tool cutting edge radius R was 23 nm and the undeformed chip thickness a_c was 21.83 nm. Hence, in the two tests, the undeformed chip thicknesses were both smaller than the tool cutting edge radii, which made it possible that the cutting was in ductile mode.

The SEM photographs of chips obtained from the two cutting tests are shown in Figure 5.3(a) and (b), respectively. It can be seen that like those of metal cutting, the chips are long and continuous, well reflecting that plastic deformation was the dominant process. However, whether or not the plastic deformation in the cutting of silicon was the same as that in cutting of ductile materials was unknown. In order to have a comparison between these two kinds of plastic deformations, a simulation of nanoscale cutting of aluminum was also carried out.

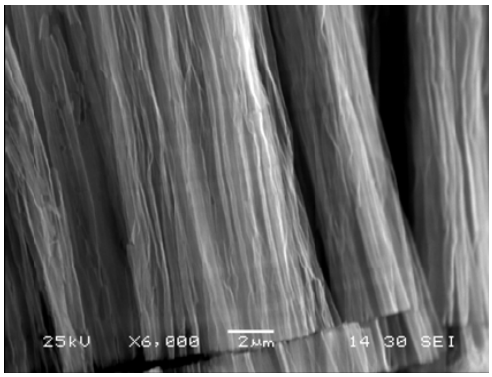

(a)

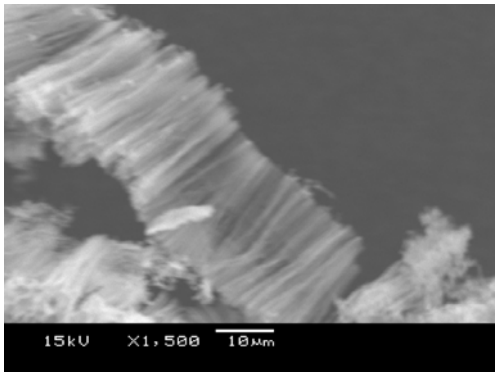

(b)

Figure 5.3 SEM photographs of continuous chips obtained in ductile mode cutting: (a) $R = 30$, $a_c = 7.73$ nm, (b) $R = 23$, $a_c = 21.83$ nm.

Figure 5.4 shows the workpiece deformation from the simulation of nanoscale cutting of aluminum, where (a) and (b) present the simulated results under the two undeformed chip thicknesses, 2.0 nm and 3.0 nm, respectively. It can be seen from Figure 5.4(a) that when the undeformed chip thickness was smaller than the cutting edge radius, the lattice structure of aluminum remained unchanged in the chip formation zone and the chip; when the undeformed chip thickness was larger than the cutting edge radius, as shown in Figure 5.4(b), the lattice structure of aluminum also remained unchanged in the chip formation zone and the chip from the frontal view and rotated views. Moreover, as shown in Figure 5.4, near the finished subsurface of aluminum, the aluminum lattice structure was not changed, remaining the same as the original structure.

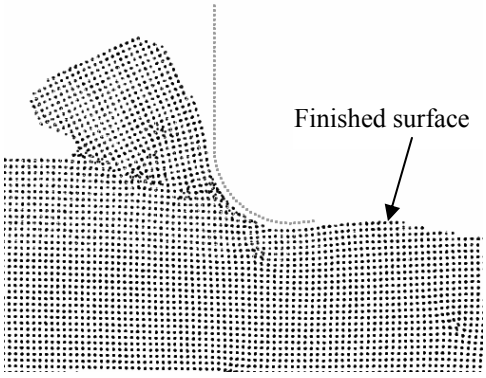

(a)

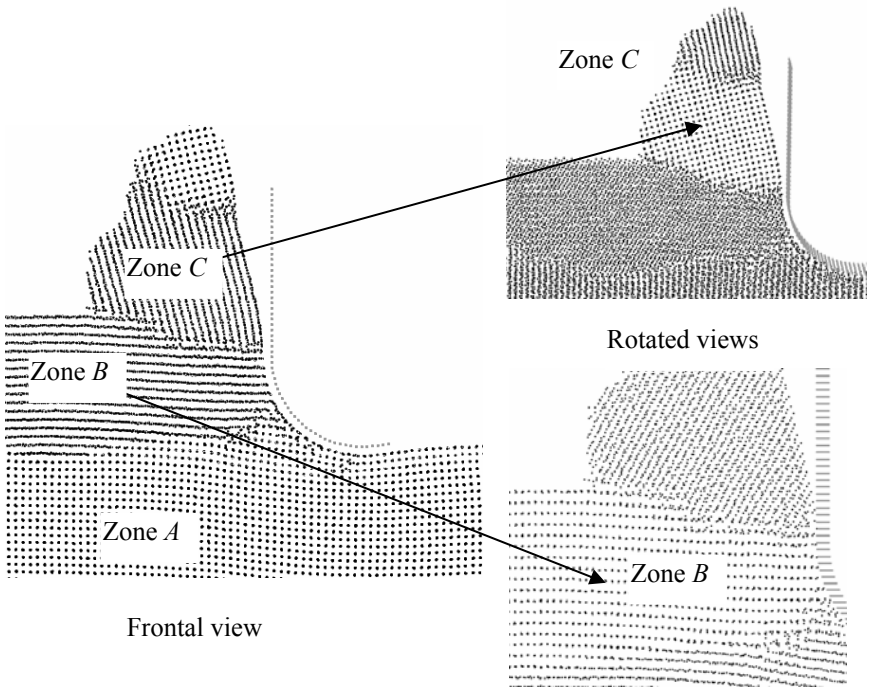

(b)

Figure 5.4 The aluminum workpiece deformation in the chip formation zone when R = 2.5 nm and the undeformed chip thicknesses were: (a) a_c = 2.0 nm and (b) a_c = 3.0 nm.

Figure 5.5 shows the distribution frequency of interatomic bond length in the aluminum workpiece, where zone *A* represents the undeformed zone, zone *B* represents the zone before the tool cutting edge in the chip formation zone, and zone *C* is in the aluminum chip. It can be seen that the curves of the distribution frequency of interatomic bond length in zones *A*, *B* and *C* are nearly superimposed by each other and they all have four peak values, i.e. 2.86 Å, 4.05 Å, 4.96 Å and 5.73 Å, corresponding to the theoretical values of interatomic bond length in aluminum, that is, all the zones show the same distribution frequency of interatomic bond length like the undeformed zone. This further indicates that the lattice structure of aluminum remains unchanged in nanoscale cutting.

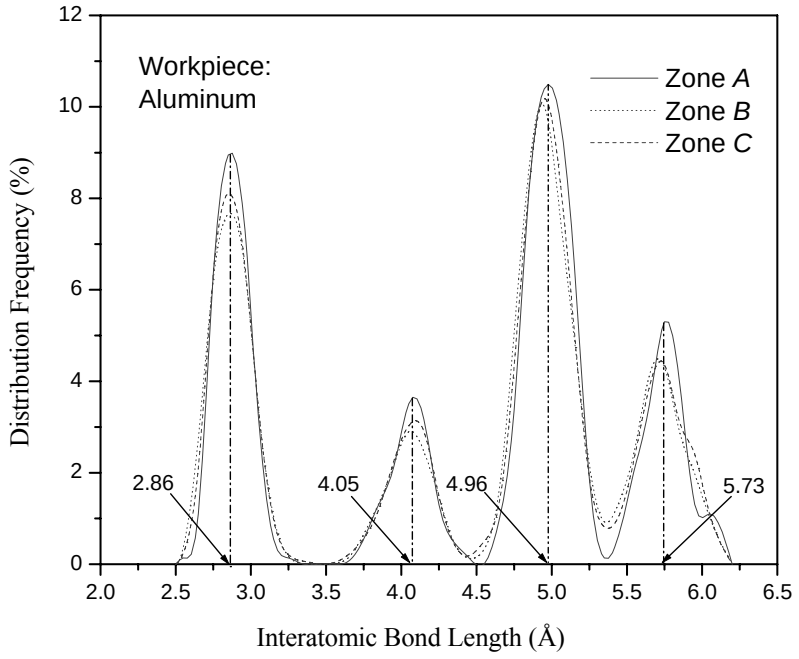

Figure 5.5 The distribution frequency of interatomic bond length in the aluminum workpiece.

Figures 5.4 and 5.5 indicate that the lattice structure of aluminum remained unchanged in the chip formation zone and near the finished surface in nanoscale cutting, thus the deformation of aluminum was clearly different from that of silicon workpiece in

nanoscale cutting as shown in section 5.3.1. This is understandable because monocrystalline aluminum as a ductile metal in nanoscale cutting is deformed by dislocation. Moreover, the dislocations occur only on the slip planes and do not destroy the lattice structure of aluminum (Hull and Bacon, 2001). As a result, in the nanoscale cutting of monocrystalline aluminum, the lattice structure of aluminum was not changed. The dislocation movements can also be observed in the simulated cutting of aluminum, as shown in Figure 5.6, in which dislocations were generated (Figure 5.6(a)) and then moved along the slip line from location as shown in Figure 5.6(b) to locations as shown in Figure 5.6(c) and (d). This is a typical plastic deformation in metal, where plastic deformation is in the form of dislocation movements. However, the plastic deformation in the chip formation zone of ductile mode cutting of silicon was different, where dislocation was not observed. The plastic deformation was a plastic flow of the material, as described in the next Section.

5.3.3 The Mechanism of Ductile Mode Cutting of Silicon

As shown in section 5.3.1, in the ductile mode cutting of silicon there was a phase transformation from diamond cubic structure to both β silicon and amorphous phase in the chip formation zone. The β phase of silicon is a metallic body-centered tetragonal structure and can lead to plastic deformation (Zhang and Tanaka, 1999; Cheong and Zhang, 2000). Moreover, in both β silicon and amorphous phase silicon in the chip formation zone, nearly all the bond lengths became longer than those of original silicon.

According to the research of Gao et al. (2003), the interatomic bond length is a very important factor in determining the hardness of covalent crystals, such as silicon and

diamond. For pure covalent crystals, the resistant force of bond can be evaluated by the energy gap E_g and the hardness of overly covalent crystals should have a following form:

$$H = A\left(N_e/2\right)^{2/3} E_g , \tag{5.1}$$

where A is a proportional coefficient, N_e is the electron density expressed in number of valence electrons per cubic angstroms and it is inversely proportional to L^3, where L represents the interatomic bond length as mentioned previously. That is,

$$N_e \propto 1/L^3 . \tag{5.2}$$

For pure covalent crystals,

$$E_g = 39.74/L^{2.5} . \tag{5.3}$$

Inserting Eqs.(5.2) and (5.3) into Eq.(5.1), the following equation can be obtained,

$$H \propto A\left(\frac{1}{2L^3}\right)^{2/3} 39.74/L^{2.5} = 25AL^{-4.5} . \tag{5.4}$$

Based on Eq. (5.4), for pure silicon, the hardness is inversely proportional to $L^{4.5}$, Therefore, the longer the bond lengths, the softer the silicon atom groups. For example, when the bond length is changed from 2.35 Å to 2.6 Å, there will be a 37% decrease in the hardness. Since nearly all the bond lengths of the silicon material in the chip

formation zone became longer than the normal bond length, the silicon workpiece material in the chip formation zone should become softer than the original silicon workpiece. As a result, like in cutting of ductile materials, the silicon workpiece material in the chip formation zone could be deformed in a form of plastic flow that is a result of high pressure phase transformation of silicon rather than atomic dislocation movement.

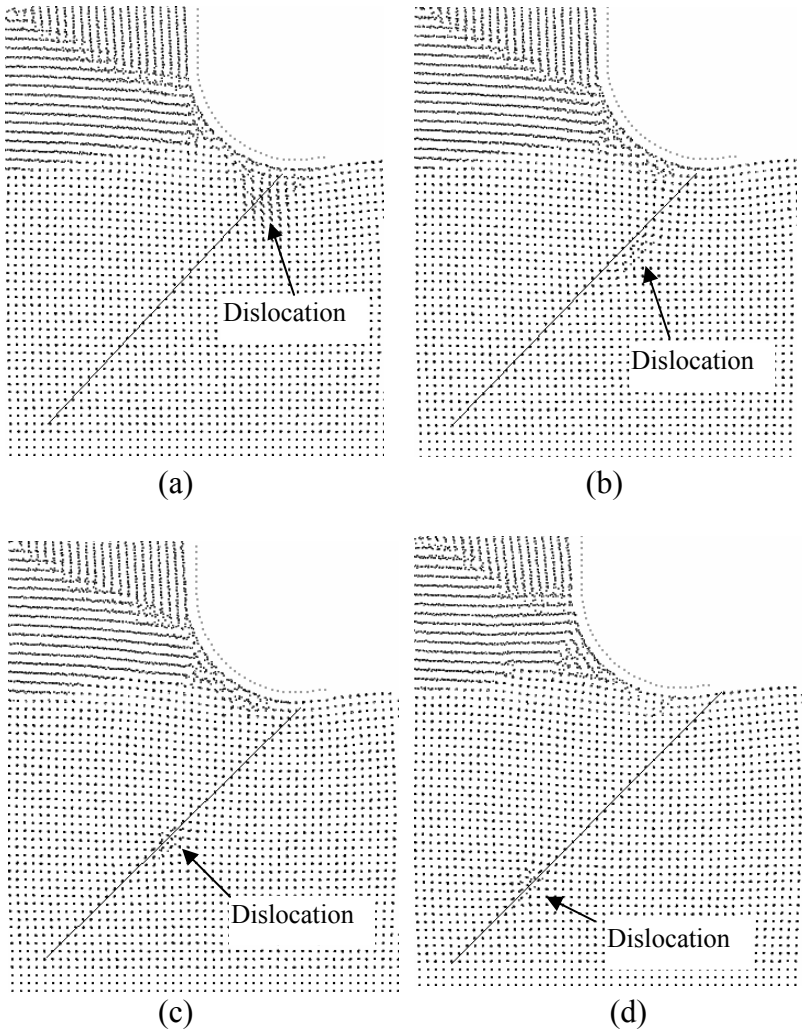

Figure 5.6 Dislocation movement in the simulated chip formation zone of nanoscale cutting of aluminum: (a) the generation of dislocation in the chip formation zone, and (b), (c) and (d) movement of dislocation along the slip line.

5.4 Concluding Remarks

In this chapter, high pressure phase transformation of monocrystalline silicon workpiece in the chip formation of nanoscale ductile cutting and its role in the ductile mode cutting of silicon have been investigated through MD simulations and cutting experiments. The following conclusions can be drawn:

1) The results of MD simulations of nanoscale cutting of silicon showed that because of the high hydrostatic pressure in the chip formation zone, there is a phase transformation of silicon from diamond cubic structure to both β silicon and amorphous phase in the chip formation zone.

2) The experimental results of nanoscale ductile cutting of silicon indicated that plastic deformation occurs in ductile mode cutting. But the comparison between workpiece deformation in cutting of silicon and that in cutting of aluminum through MD simulations showed that unlike cutting of aluminum, in nanoscale cutting of silicon the plastic deformation is not a result of dislocation movements.

3) In the case of ductile mode cutting of silicon, it is the high pressure phase transformation of silicon that results in the plastic deformation in ductile mode cutting of silicon.

Chapter 6

Upper Bound of Tool Cutting Edge Radius

6.1 Introduction

In cutting of brittle materials, experimentally it was observed that there is an upper bound of tool cutting edge radius, beyond which, although the undeformed chip thickness is small than the tool cutting edge radius, the ductile mode cutting cannot be achieved. However, why there is an upper bound of tool cutting edge radius in nanoscale ductile mode cutting of brittle materials has not been fully understood. In this thesis, based on the tensile stress distribution and the characteristics of the distribution obtained from molecular dynamics (MD) simulation of nanoscale ductile cutting of silicon, an approximation for the tensile stress distribution was obtained. Using this tensile stress distribution with the principles of geometrical similarity and fracture mechanics, the critical conditions for crack initiation have been determined. The result showed that there is a critical tool cutting edge radius, beyond which crack initiation can occur in the nanoscale cutting of silicon and the chip formation mode is transferred from ductile to brittle. That is, this critical tool cutting edge radius is the upper bound of the tool cutting edge radius for ductile mode cutting of silicon.

6.2 Experimental Observation

SEM photographs of the machined silicon wafer surfaces achieved in cutting of silicon wafers using diamond tools with different cutting edge radii at cutting speed of 150 m/min are shown in the Figures (from Figure 6.1 to 6.12). For the diamond tool edge radius of 23 nm, 202 nm, 490 nm, 623 nm and 717 nm, one test was conducted under the condition that the undeformed chip thickness was less than the tool edge radius and the other test was conducted under the condition that the undeformed chip thickness was larger than the tool edge radius. For diamond tool edge radius of 807 nm, both the tests were conducted under the condition that the undeformed chip thickness was less than the tool edge radius.

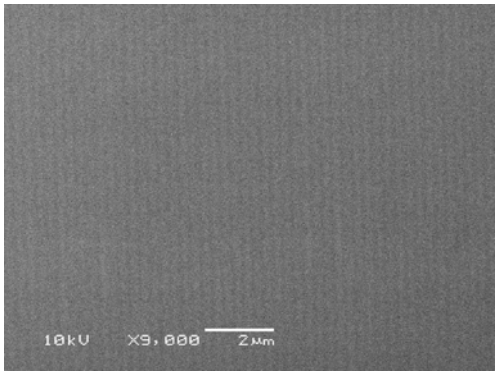

Figure 6.1 Cutting edge radius R = 23 nm; undeformed chip thickness a_c = 21.83 nm.

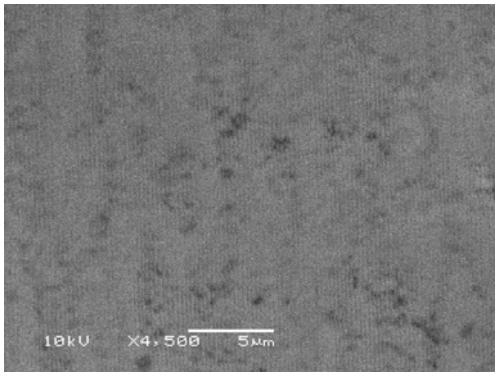

Figure 6.2 Cutting edge radius R = 23 nm; undeformed chip thickness a_c = 24.9 nm.

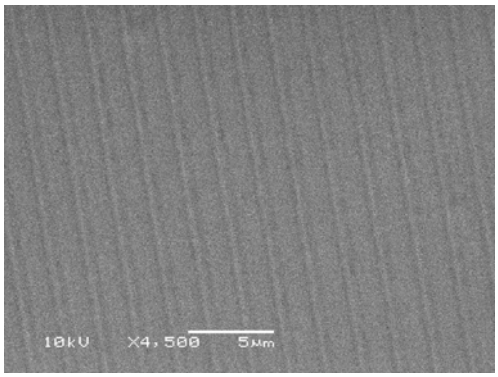

Figure 6.3 Cutting edge radius R = 202 nm; undeformed chip thickness a_c = 188 nm.

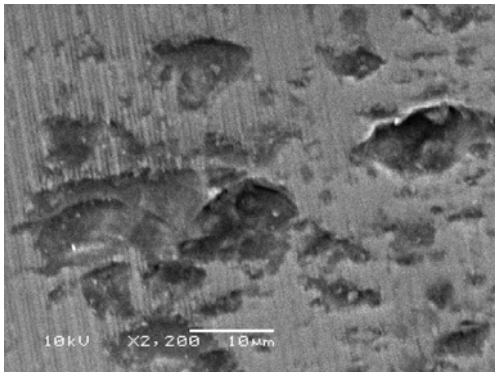

Figure 6.4 Cutting edge radius R = 202 nm; undeformed chip thickness a_c = 215 nm.

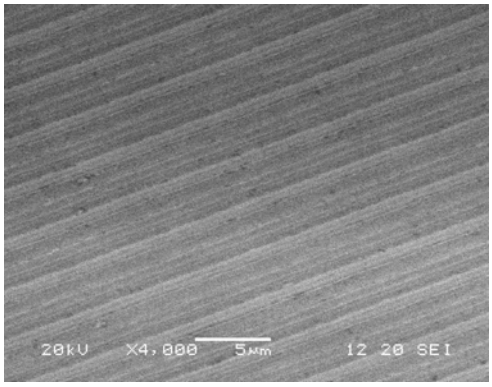

Figure 6.5 Cutting edge radius R = 490 nm; undeformed chip thickness a_c = 455 nm.

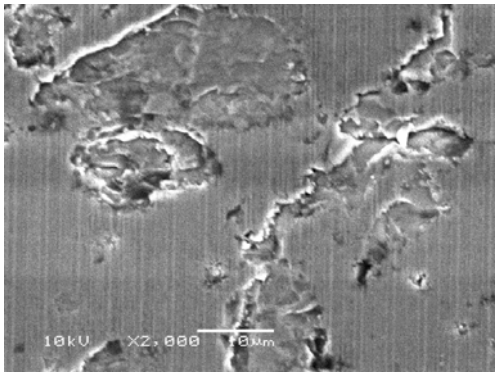

Figure 6.6 Cutting edge radius R = 490 nm; undeformed chip thickness a_c = 520 nm.

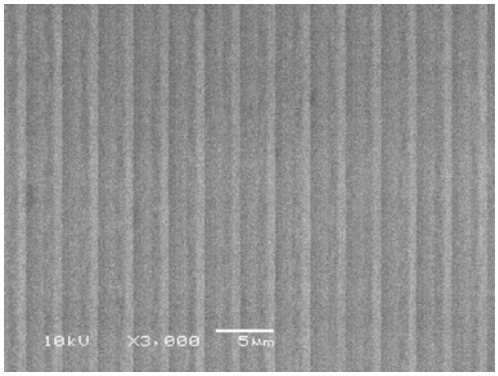

Figure 6.7 Cutting edge radius R = 623 nm; undeformed chip thickness a_c = 588 nm.

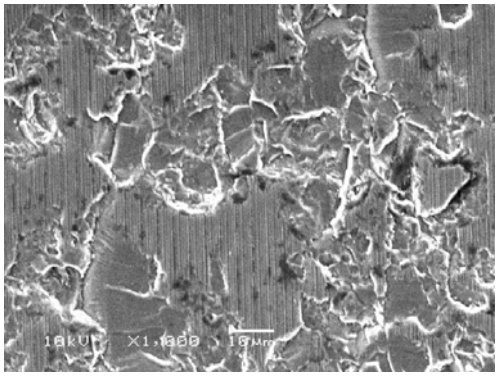

Figure 6.8 Cutting edge radius R = 623 nm; undeformed chip thickness a_c = 675 nm.

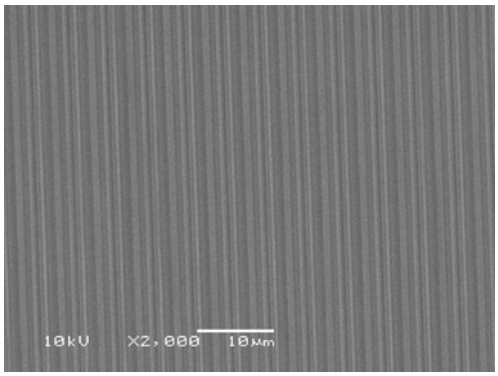

Figure 6.9 Cutting edge radius R = 717 nm; undeformed chip thickness a_c = 681 nm.

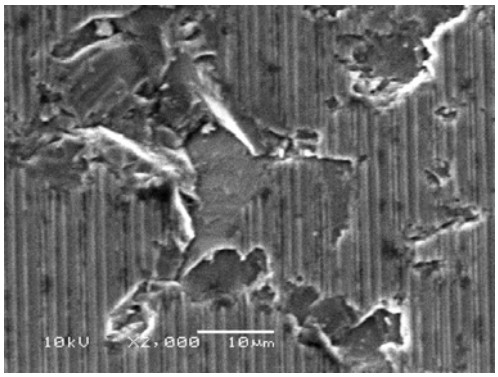

Figure 6.10 Cutting edge radius R = 717 nm; undeformed chip thickness a_c = 748 nm.

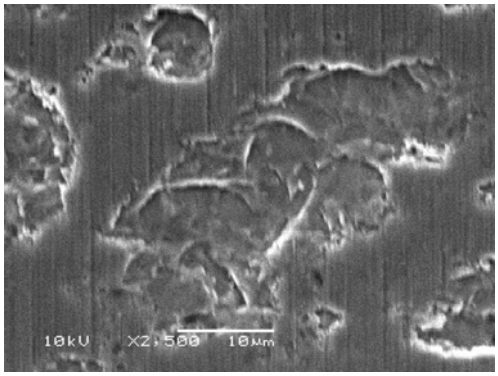

Figure 6.11 Cutting edge radius R = 807 nm; undeformed chip thickness a_c = 750 nm.

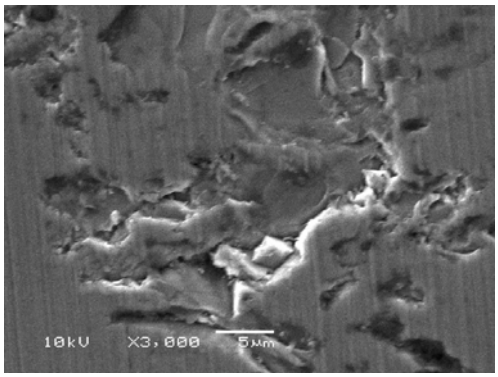

Figure 6.12 Cutting edge radius R = 807 nm; undeformed chip thickness a_c = 607 nm.

SEM observations indicated that when the tool cutting edge radius was not larger than 807 *nm* and undeformed chip thickness was smaller than the tool cutting edge radius, the machined workpiece surfaces were very smooth and feed marks were clearly displayed on the surfaces, which show that the cutting was carried out under ductile mode. On the other hand, when the undeformed chip thickness was larger than the tool cutting edge radius, the machined workpiece surfaces were very rough and fractured, which show that the cutting was conducted under brittle mode. However, when the tool cutting edge radius reached 807 nm and even undeformed chip thickness was much smaller than the tool cutting edge radius, the machined workpiece surfaces were very

rough and fractured, which show that the cutting was carried out in a brittle mode under the cutting conditions. It is likely that the tool cutting edge radius of 807 nm is an upper bound for ductile mode cutting of silicon wafer material. As a result, in order to achieve ductile mode cutting of silicon wafer material, two conditions should be satisfied: (1) the diamond tool edge radius must be very small, that is, there is an upper bound of the tool edge radius, (2) the undeformed chip thickness must be smaller than the tool cutting edge radius.

These two necessary conditions in nanoscale ductile mode cutting of monocrystalline silicon have been explained based on MD simulation results. In this chapter, the explanation for the first necessary condition is presented.

6.3 MD Simulation Condition

A series of MD simulations have been carried out under different cutting edge radii, which were 2.5 nm, 4.0 nm and 6.0 nm, respectively. In the simulations, the ratio of undeformed chip thickness to the cutting edge radius was fixed at 0.8, so that the corresponding undeformed chip thicknesses are 2 nm, 3.2 nm and 4.8 nm, respectively. This cutting condition makes it possible that the chip formation is in ductile mode. The working environment temperature was set at 293 K and the cutting speed was set at 20 m/s.

6.4 Tensile Stress Distribution and Cutting Forces

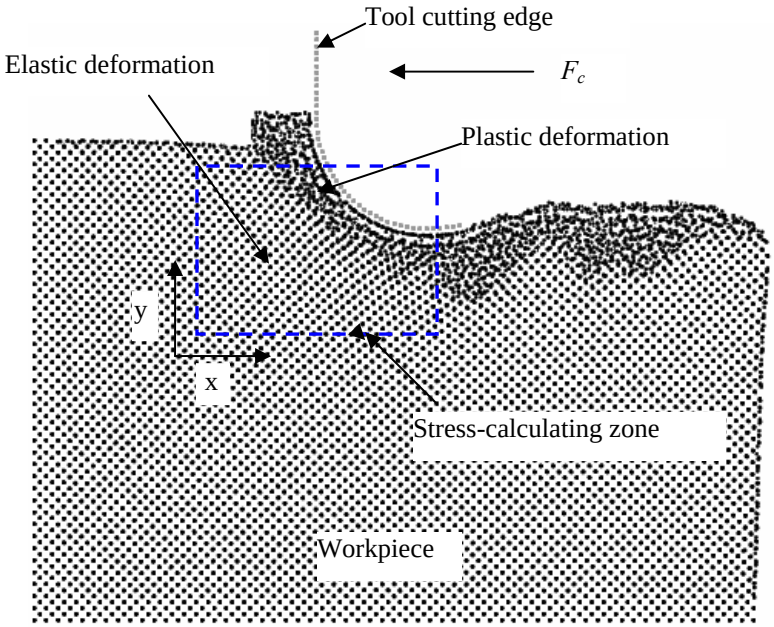

Figure 6.13 A snapshot of the MD simulation of nanoscale cutting process.

Figure 6.13 shows a snapshot of the MD simulation of nanoscale cutting process. The normal stress along the *y* direction σ_{yy} in the stress-calculating zone as shown in Figure 6.13 has been calculated. Figures 6.14, 6.15 and 6.16 show the normal stress σ_{yy} distributions in the stress-calculating zone under different cutting conditions, R = 2.5 nm and a_c = 2.0 nm, R = 4.0 nm and a_c = 3.2 nm, and R = 6.0 nm and a_c = 4.8 nm, respectively. From these figures, it can be seen that in most areas of the stress-calculating zone, σ_{yy} is compressive stress and only in a small area it is tensile stress (the positive value represents compressive stress and the negative value tensile stress). It also can be seen that this small area with tensile stress borders upon the interface of plastic and elastic deformation zones as shown in Figure 6.13. Moreover, the

maximum value of tensile stress σ_{yy} will increase and the location of the maximum tensile stress σ_{yy} will be nearer to the interface of plastic and elastic deformation zones.

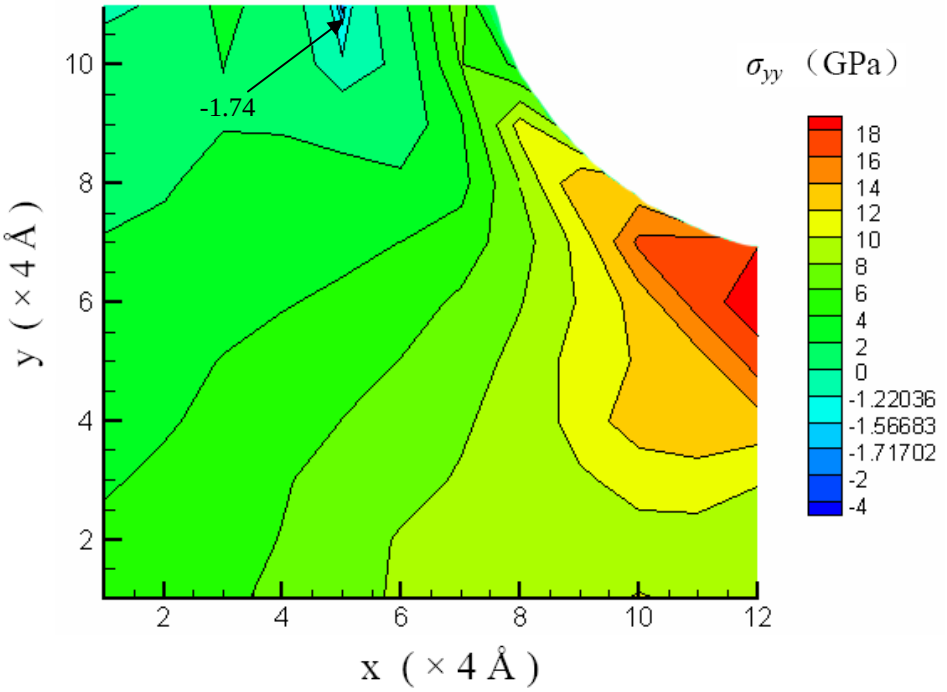

Figure 6.14 The normal stress σ_{yy} distribution in the stress-calculating zone when R = 2.5 nm and a_c = 2.0 nm.

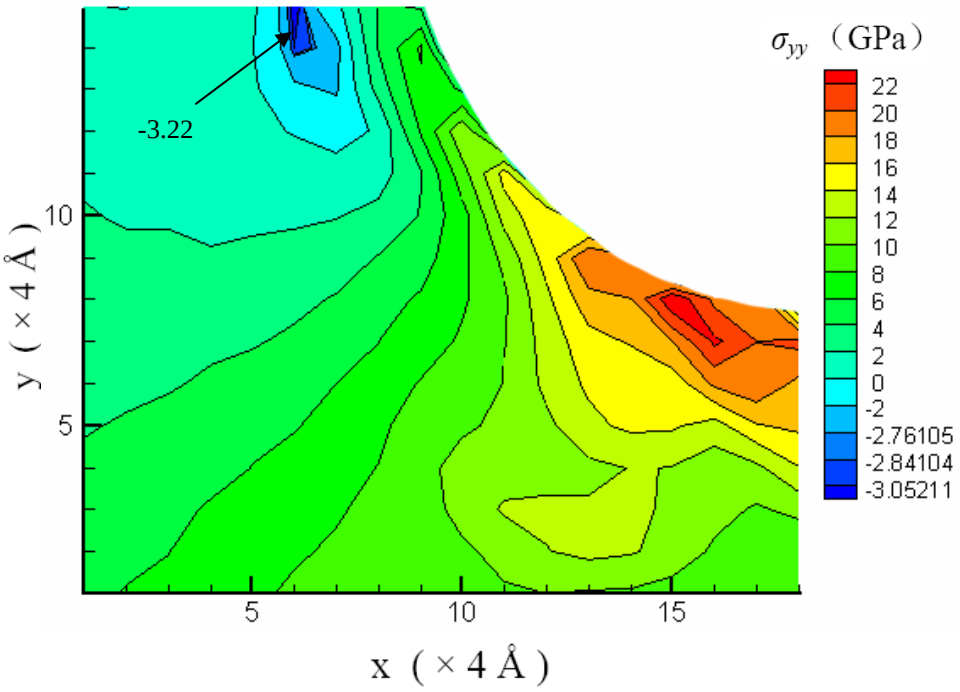

Figure 6.15 The normal stress σ_{yy} distribution in the stress-calculating zone when R = 4.0 nm and a_c = 3.2 nm.

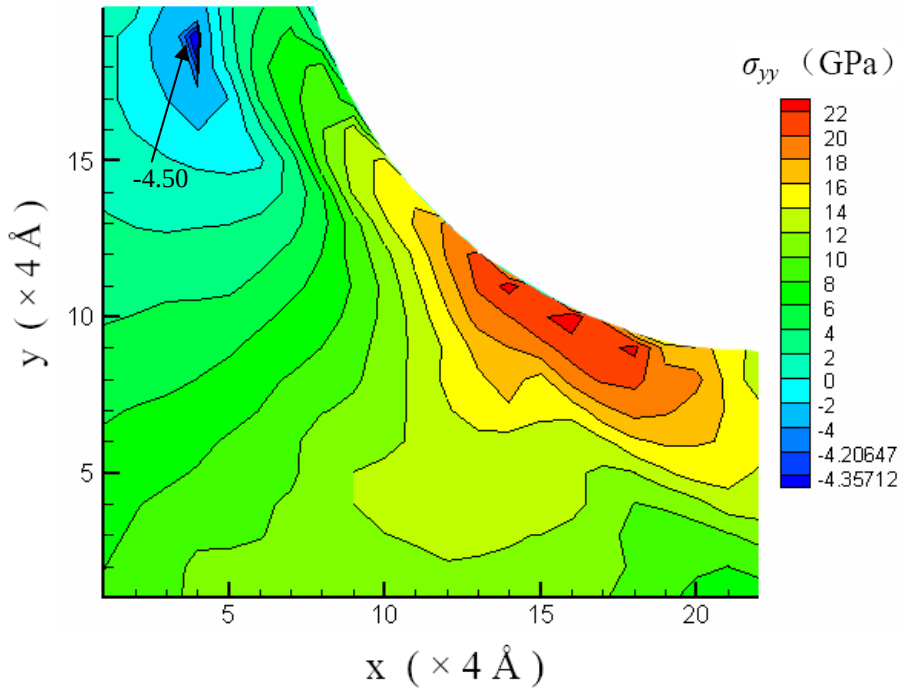

Figure 6.16 The normal stress σ_{yy} distribution in the stress-calculating zone when R = 6.0 nm and a_c = 4.8 nm.

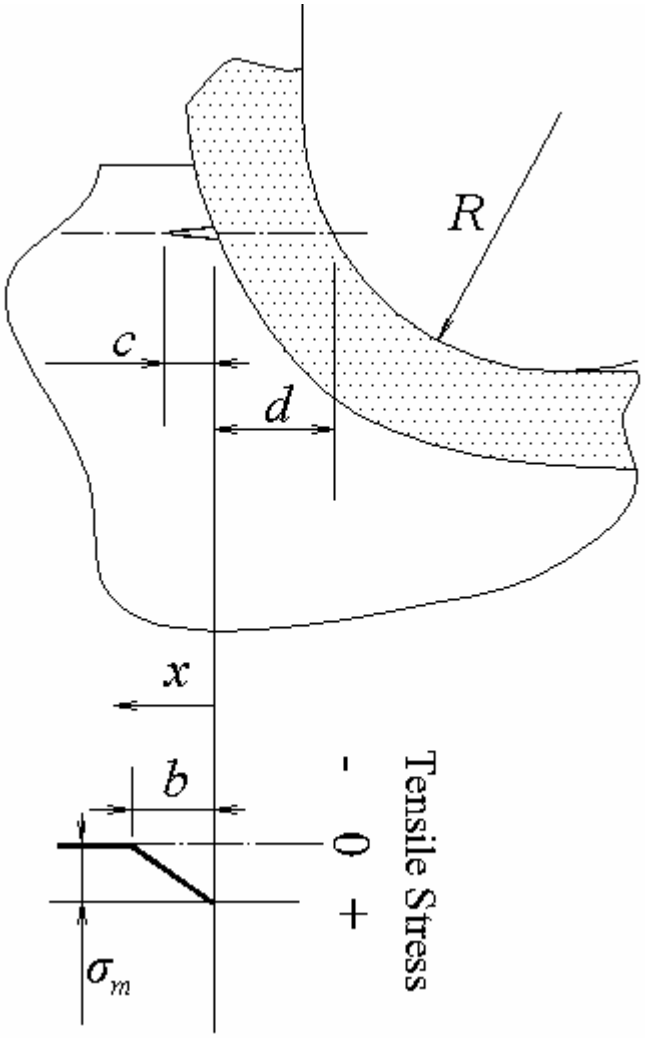

Figure 6.17 The model for the edge crack initiation in nanoscale cutting of silicon.

Based on this tensile stress distribution and the characteristics of the distribution obtained from MD simulation of nanoscale cutting of silicon, a simple linear approximation for the tensile stress distribution is given as shown in Figure 6.17 when the tool cutting edge radius reaches its upper bound,

$$\sigma(x) = \begin{cases} \sigma_m(1 - x/b) & (x \le b) \\ 0 & (x \ge b) \end{cases}, \tag{6.1}$$

where b is the size of tensile stress field, σ_m represents the maximum tension at the interface. The actual tensile stress filed is extremely complex and should depend on other parameters. Moreover, out of the range b, the normal stress in y direction is compressive stress. However, this simplified linear stress distribution is essentially same as the complex stress field (Lawn and Evans, 1977) and it will be useful to deduce the formulation.

The cutting force F_c (see Figure 6.13) in the cutting direction at the different tool cutting edge radius is shown in Figure 6.18, which indicates that when the tool cutting edge radius increases, the cutting force acting on the cutting tool also increases.

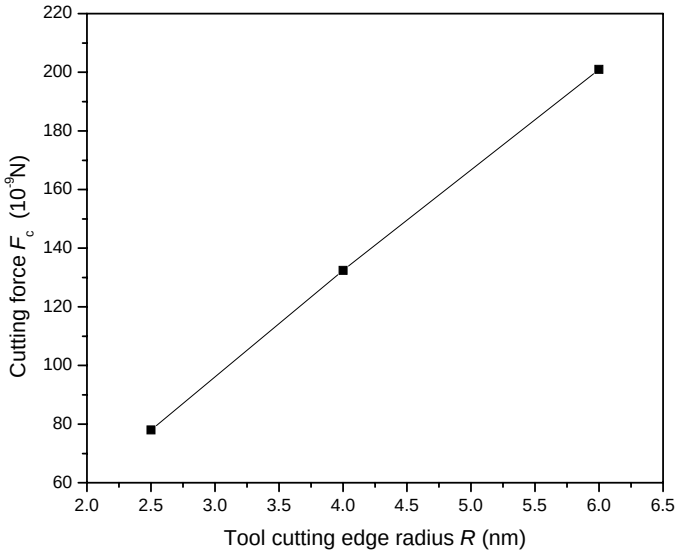

Figure 6.18 The cutting force F_c acting on the cutting tool at the different tool cutting edge radius.

6.5 A Model for Crack Initiation in Nanoscale Cutting

6.5.1 Defect

In the plastic deformation zone (the size d as shown in Figure 6.17), there is a phase transformation of the monocrytslline silicon from diamond cubic structure to both β silicon and amorphous phase due to the high compressive stress (see Chapter 5). Therefore, the interface of plastic and elastic deformations is similar to a grain boundary. Because of the different lattice structures in the plastic and elastic deformation zones, the small defect will occur at the interface, which has been shown in Figure 6.17 with the length c.

6.5.2 Model for Crack Initiation

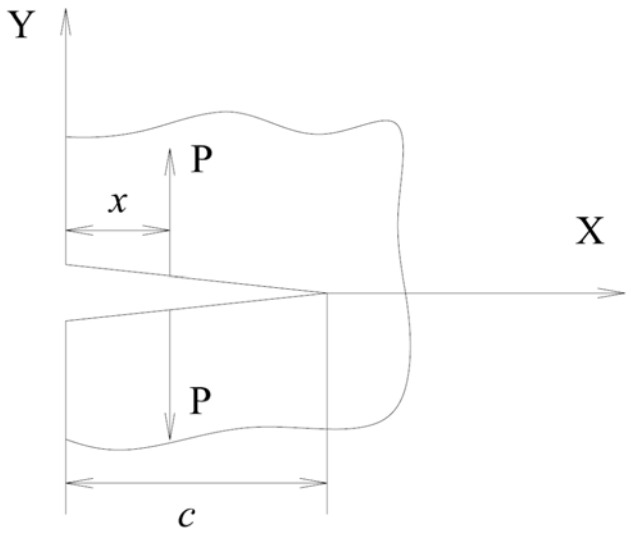

Figure 6.19 A mode I edge crack.

As shown in Figure 6.17, a model for crack initiation has been proposed. In the tensile stress area, there is a defect at the interface of plastic and elastic deformation zones. With this tensile stress, the defect can propagate and form an edge crack, but when the tensile stress is not enough for defect propagation, the defect will be stable, so the crack will not be initiated and chip is formed in ductile mode. Since the tensile stress will increase when the tool cutting edge radius increases as mentioned in Section 6.4, there should be an upper bound of the tool cutting edge radius for the ductile mode chip formation.

In order to determine the critical condition of defect propagation, the stress intensity factor for this edge crack in the tensile stress field should be evaluated. The Green's function for an edge crack loaded by a tensile force P is (Tada et al., 2000)

$$K_I = \frac{2}{3}\frac{P}{\sqrt{\pi c}}\frac{4-\left(\frac{x}{c}\right)}{\sqrt{1-\left(\frac{x}{c}\right)^2}}, \tag{6.2}$$

where K_I is the stress intensity factor, c is the initial length of the crack, and x represents the place of the force P as shown in Figure 6.19. Based on this Green's function, and using the Schwartz alternating method (Kantorovich and Krylov, 1964), a first approximation for the stress intensity factor for this edge crack in the simplified linear stress field yields,

$$K_I = \frac{2}{3}\frac{1}{\sqrt{\pi c}}\int_0^c \sigma(x)dx\frac{4-\left(\frac{x}{c}\right)}{\sqrt{1-\left(\frac{x}{c}\right)^2}}. \tag{6.3}$$

Substituting Eq. (6.1) into Eq. (6.3), the stress intensity factors are obtained in different conditions,

$$K_I = (2\sigma_m/3)(c/\pi)^{1/2}\left[2\pi - 1 + (\pi/4 - 4)(c/b)\right], \qquad c \le b\,, \tag{6.4a}$$

$$K_I = (\sigma_m/3)(c/\pi)^{1/2}\left\{(8c/b+1)\left(1-b^2/c^2\right)^{1/2} + (8+c/b)\tan^{-1}\left[1/\left(c^2/b^2-1\right)^{1/2}\right] - 8c/b - 2\right\}, \qquad c \ge b. \tag{6.4b}$$

The MD simulation result has shown that when the tool cutting edge radius increases, the cutting force acting on the cutting tool also increases. So, when the tool cutting edge radius just reaches the critical value for crack initiation, the cutting force F_c in the cutting direction also reaches the maximum value F_m. A new material hardness, the cutting hardness H_c, is defined using the maximum value F_m,

$$H_c = F_m/(\lambda_1 W_h W_w), \tag{6.5}$$

where λ_1 is a dimensionless factor determined by the tool geometry, W_h is the height of the area subject to cutting force in the cutting direction and W_w is the width of the area subject to cutting force. Both W_h and W_w are scaled with the tool cutting edge radius R using coefficients λ_2 and λ_3, respectively,

$$W_h = \lambda_2 R\,,\ W_w = \lambda_3 R\,. \tag{6.6}$$

H_c represents the resistance to crack initiation, which is similar to the indentation hardness H or scratching hardness H_s of brittle materials and should be a constant of

the material property. It is supposed that for monocrystalline silicon the ratio of the cutting hardness to the indentation hardness is ζ (Ichimura and Rodrigo, 2000),

$$H_c = \zeta H . \tag{6.7}$$

The maximum tensile stress should scale directly with the cutting hardness in the cutting direction (Lawn and Evens, 1977), that is

$$\sigma_m = \theta H_c = \theta \zeta H , \tag{6.8}$$

where θ is a dimensionless factor. The size of the tensile stress field b also should scale with the tool size R, so

$$b = \eta R = \eta \left[F_m / \left(\zeta \lambda_1 \lambda_2 \lambda_3 H \right) \right]^{1/2} , \tag{6.9}$$

where η is another dimensionless constant. According to the Griffith criterion, when the crack starts to grow, K_I reaches the critical stress intensity factor K_{Ic}, that is,

$$K_I = K_{Ic} . \tag{6.10}$$

Substituting Eqs.(6.8), (6.9) and (6.10) into Eq. (6.4), and after simplification, the critical condition equations for the crack growth can be obtained as follows:

$$1 = 2\mathscr{C}^{1/2} \left[2\pi - 1 + \left(\pi/4 - 4 \right) \left(\mathscr{C} / \mathscr{T}^{1/2} \right) \right], \qquad \mathscr{C}^2 \le \mathscr{T} , \tag{6.11a}$$

$$1 = \mathscr{C}^{1/2}\left\{\left(8\mathscr{C}/\mathscr{F}^{1/2}+1\right)\left(1-\mathscr{F}/\mathscr{C}^{2}\right)^{1/2}+\left(8+\mathscr{C}/\mathscr{F}^{1/2}\right)\tan^{-1}\left[1\Big/\left(\mathscr{C}^{2}/\mathscr{F}-1\right)^{1/2}\right]-8\mathscr{C}/\mathscr{F}^{1/2}-2\right\},\qquad \mathscr{C}^{2}\geq\mathscr{F}, \tag{6.11b}$$

where $\mathscr{C}$ and $\mathscr{F}$ are the normalized defect length and normalized cutting force, respectively,

$$\mathscr{C} = \left[\left(\theta\zeta H\right)\Big/\left(3\pi^{1/2}K_{Ic}\right)\right]^{2} c, \tag{6.12a}$$

$$\mathscr{F} = \left[\left(\eta^{2}\theta^{4}\zeta^{3}H^{3}\right)\Big/\left(81\pi^{2}\lambda_{1}\lambda_{2}\lambda_{3}K_{Ic}{}^{4}\right)\right]F_{m}. \tag{6.12b}$$

6.5.3 Discussion

Eq. (6.11) only has two variables and it is can be set that $\mathscr{F}$ is the function of variable $\mathscr{C}$. Based on this, the solution of function $\mathscr{F}(\mathscr{C})$ can be plotted as shown in Figure 6.20. Since Eq. (6.11) represents the critical condition for crack growth, the curve of $\mathscr{F}(\mathscr{C})$ shows the critical normalized cutting force $\mathscr{F}$ corresponding to the different normalized defect length $\mathscr{C}$ when the crack begins to grow. From Figure 6.20, it can be seen that there is a lowest point ($\mathscr{C}^*$ = 0.02015, $\mathscr{F}^*$ = 0.00135) along the curve of $\mathscr{F}(\mathscr{C})$, where

$$\mathscr{C}^* = 0.02015, \tag{6.13a}$$

$$\mathscr{F}^* = 0.00135, \tag{6.13b}$$

that is, when the normalized cutting force is smaller than $\mathscr{F}^*$, the defect will not extend regardless of the size and place of defect. Therefore, the lowest point is a critical point and only when the normalized defect length and normalized cutting force both reach the critical value $\mathscr{C}^*$ and $\mathscr{F}^*$, respectively, the crack propagates.

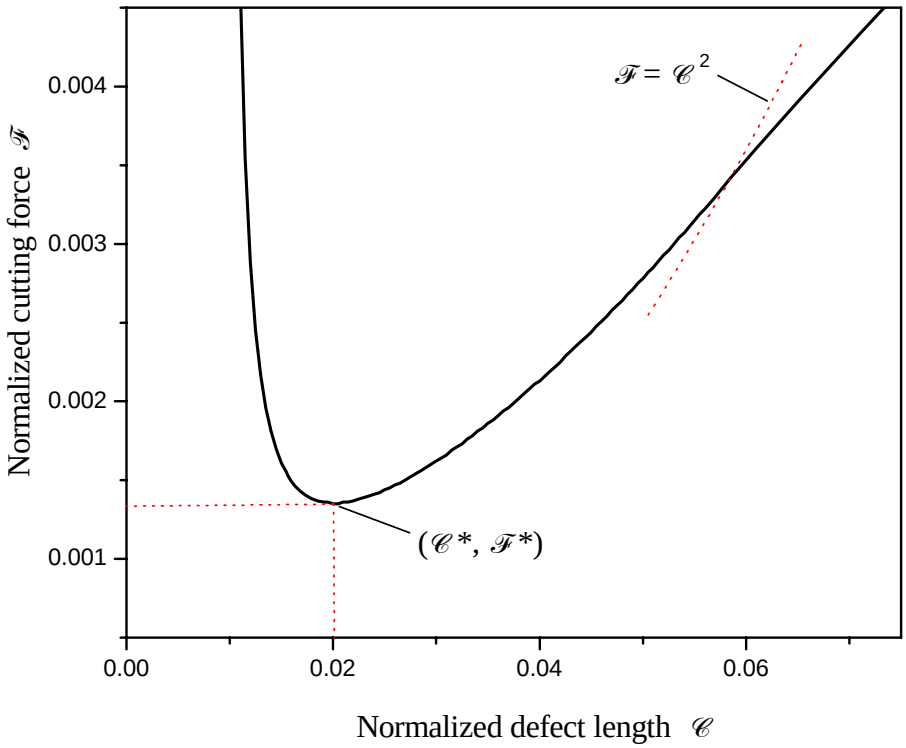

Figure 6.20 Plot of function $\mathscr{F}(\mathscr{C})$.

According to Eqs. (6.12) and (6.13), the critical defect length and critical cutting force for the crack initiation can be obtained as follows:

$$c^* = \left[0.5697 \Big/ \left(\theta^2 \zeta^2\right)\right] \left(K_{Ic}/H\right)^2, \tag{6.14a}$$

$$F_m{}^* = \left[\left(1.079 \lambda_1 \lambda_2 \lambda_3\right) \Big/ \eta^2 \theta^4 \zeta^3\right] K_{Ic}{}^4 \Big/ H^3 . \tag{6.14b}$$

Based on the assumption that the defect length for crack initiation scales directly with the machining size (Marshall and Lawn, 1986), which is the tool cutting edge radius R here, the critical tool cutting edge radius R^* can be obtained,

$$R^* = \kappa c^* = \left[0.5697\kappa \Big/ \left(\theta^2 \zeta^2\right)\right]\left(K_{Ic}/H\right)^2, \tag{6.15}$$

where κ is a dimensionless factor, and represents the ratio of the critical tool cutting edge radius to the critical defect length. Since when the tool cutting edge radius is beyond the critical value *R**, the crack initiation becomes possible and the chip formation mode is transferred from ductile to brittle, the critical tool cutting edge radius *R** is the upper bound of tool edge radius in nanoscale ductile mode cutting of silicon wafer. Eq. (6.15) indicates that the upper bound of the tool cutting edge radius mainly depends on the ratio of the critical stress intensity factor to the indentation hardness of the material and this is similar to the result of indentation (see Eq. (1.2)).

6.6 Concluding Remarks

Experimentally it was observed that there is an upper bound of tool cutting edge radius, beyond which, although the undeformed chip thickness is small than the tool cutting edge radius, ductile mode cutting cannot be achieved. This phenomenon that there is an upper bound of tool edge radius in nanoscale ductile mode cutting of silicon wafer has been explained based on the MD simulation result. The MD simulation result of stress showed that the tensile stress exists in a small area, which borders up the interface of plastic and elastic deformation zones, and the location of the maximum tensile stress is near to this interface. Based on the tensile stress distribution and the characteristics of the distribution obtained from MD simulation, a simple approximation for the tensile stress distribution was obtained. Using this tensile stress

distribution with the principles of geometrical similarity and fracture mechanics, the critical conditions for crack initiation have been determined. The analysis showed that there is a critical tool cutting edge radius beyond which, crack initiation can occur in the nanoscale cutting of silicon and the chip formation mode is transferred from ductile to brittle. Therefore, this critical tool cutting edge radius is the upper bound of the tool cutting edge radius for the ductile mode cutting of silicon.

Chapter 7

Crack Initiation in Relation to the Ratio of Undeformed Chip Thickness to Tool Cutting Edge Radius

7.1 Introduction

In Chapter 6, the experimental results of cutting of monocrystalline silicon showed that there is a ductile-brittle transition when the undeformed chip thickness is increased from smaller to larger than the tool cutting edge radius of the zero rake angle. However, how the crack is initiated in the ductile-brittle mode transition as the undeformed chip thickness is increased from smaller to larger than the tool cutting edge radius (that is, the ratio of undeformed chip thickness to tool cutting edge radius changes from $a_c/R < 1$ to $a_c/R > 1$) has not been fully understood.

In this chapter, crack initiation in the ductile-brittle mode transition as the undeformed chip thickness is increased from smaller to larger than the tool cutting edge radius has been studied using the molecular dynamics (MD) method on nanoscale cutting of monocrystalline silicon with a non-zero edge radius tool, from which, for the first time, a peak deformation zone in the chip formation zone has been found in the transition from ductile mode to brittle mode cutting. The results showed that as the undeformed chip thickness is larger than the cutting edge radius, in the chip formation zone there is a peak deformation depth in association with the connecting point of tool edge arc and

the rake face, and there is a crack initiation zone in the undeformed workpiece next to the peak deformation zone, in which the material is tensile stressed and the tensile stress is perpendicular to the direction from the connecting point to the peak. When the undeformed chip thickness is smaller than the cutting edge radius, there is no deformation peak in the chip formation zone, and there is no crack initiation zone formed in the undeformed workpiece. This finding explains well the ductile-brittle transition as the undeformed chip thickness increases from smaller to larger than the tool cutting edge radius.

7.2 MD Simulation Condition

In this simulation for nanoscale ductile cutting of monocrystalline silicon, the dimensions of the silicon workpiece used were $30a \times 20a \times 4a$. The working environment temperature was set at 293 K and the cutting speed was set at 20 m/s.

Two sets of simulations were conducted in this study. In the first set, the tool cutting edge radius R was fixed at 3.5 nm, and three cuts were performed, at the undeformed chip thickness of $a_c < R$ (a_c = 2.8 nm), $a_c = R$ (a_c = 3.5 nm), and $a_c > R$ (a_c = 4.0 nm), respectively. In the second set, the tool cutting edge radius R was fixed at 4.0 nm, and also three cuts were performed, at the undeformed chip thickness of $a_c < R$ (a_c = 3.2 nm), $a_c = R$ (a_c = 4.0 nm), and $a_c > R$ (a_c = 4.5 nm), respectively.

7.3 Results and Discussion

7.3.1 The Peak Deformation Zone

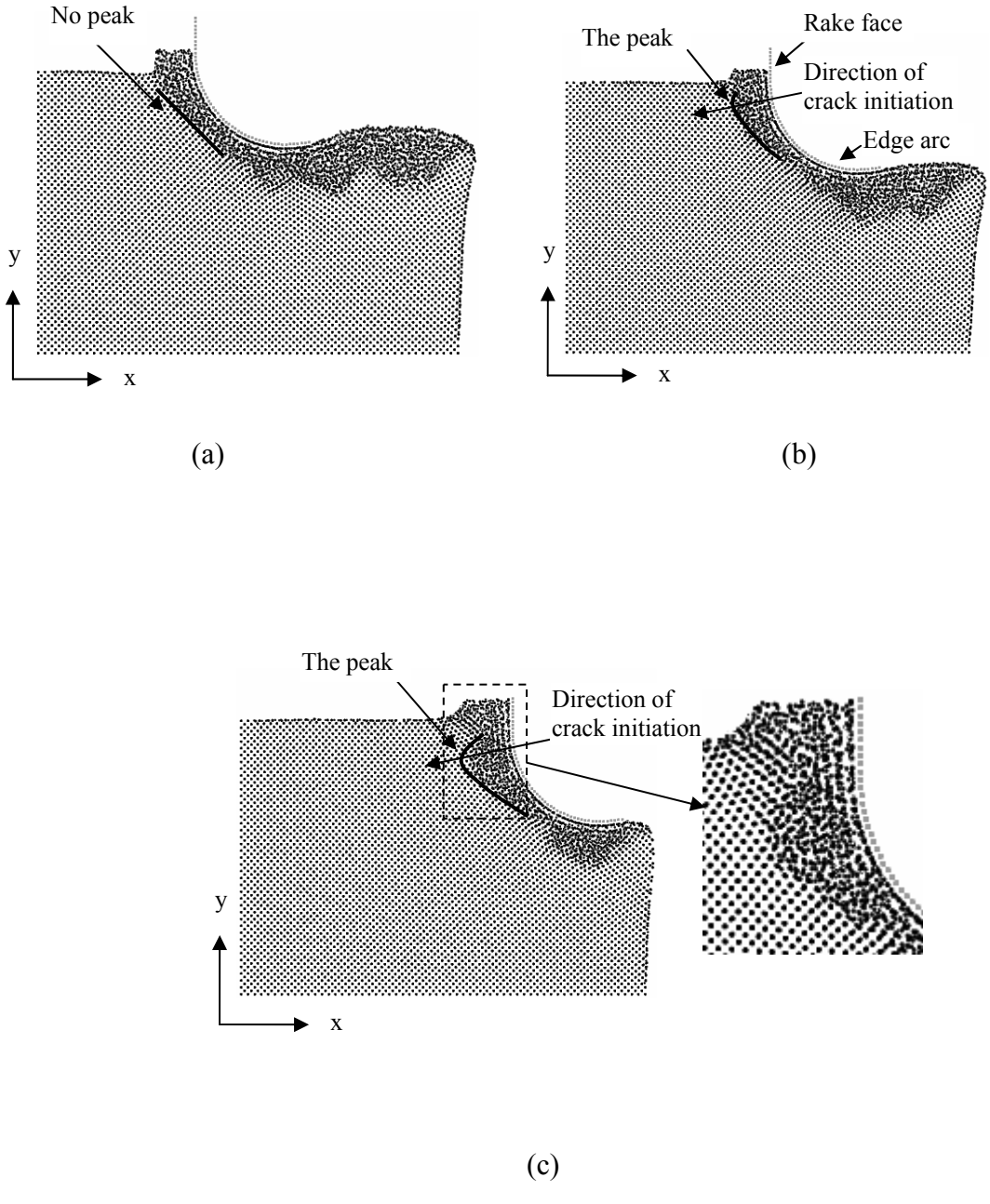

Figure 7.1 The workpiece deformation in the chip formation zone when R = 3.5 nm and the undeformed chip thicknesses were: (a) a_c = 2.8 nm (a_c/R<1), (b) a_c = 3.5 nm (a_c/R=1) and (c) a_c = 4.0 nm (a_c/R>1).

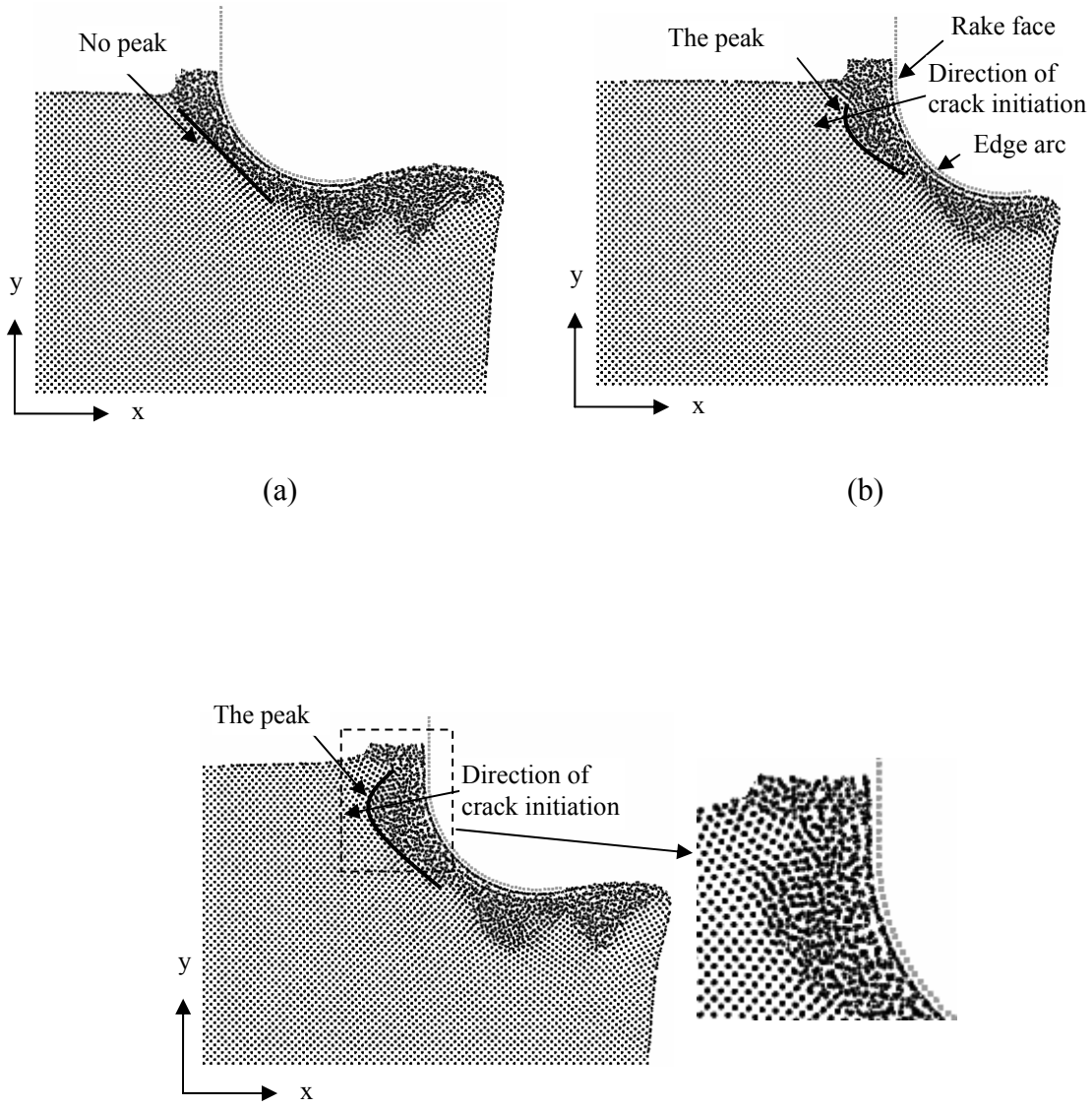

Figure 7.2 The workpiece deformation in the chip formation zone when R = 4.0 nm and the undeformed chip thicknesses were: (a) a_c = 3.2 nm (a_c/R<1), (b) a_c = 4.0 nm (a_c/R=1) and (c) a_c = 4.5 nm (a_c/R>1).

Figure 7.1 shows the result from the first set of simulations, where (a), (b), and (c) present the simulated results of nanoscale cutting for the three undeformed chip thicknesses, 2.8 nm, 3.5 nm, and 4.0 nm, respectively. It can be seen from Figure 7.1(a) that when the undeformed chip thickness was smaller than the cutting edge radius ($a_c/R<1$), along the tool edge the variation of workpiece deformation in the chip formation zone was flat, and the largest deformation took place at the surface of workpiece. However, when the undeformed chip thickness was equal to or larger than the cutting edge radius ($a_c/R\geq1$), as shown in Figures 7.1(b) and 7.1(c), there was a peak deformation zone in the chip formation zone corresponding to the connecting point of tool edge arc and the rake face, where the black lines are the boundaries between plastically deformed and elastically deformed materials. Similar result was obtained from the second set of simulations, as shown in Figure 7.2, where the cutting edge radius was 4.0 nm and the three undeformed chip thicknesses were 3.2 nm, 4.0 nm, and 4.5 nm, respectively.

7.3.2 The Tensile Stress in Association with the Peak

Consider the stress conditions in the workpiece next to the peak deformation zone in the chip formation zone. The stresses were calculated for cutting at the undeformed chip thickness smaller, equal to and larger than the cutting edge radius of two different values. For the first set of simulations, in cutting with the tool edge radius 3.5 nm at the three undeformed chip thickness 2.8 nm, 3.5 nm, and 4.0 nm, respectively, Figures 7.3 and 7.4 show the variations of the stresses in the stressed zone next to the peak deformation zone, where the simulation steps indicate tool advancing against the workpiece and the σ_{xx} and σ_{yy} represent the normal stresses in the x and y directions. It

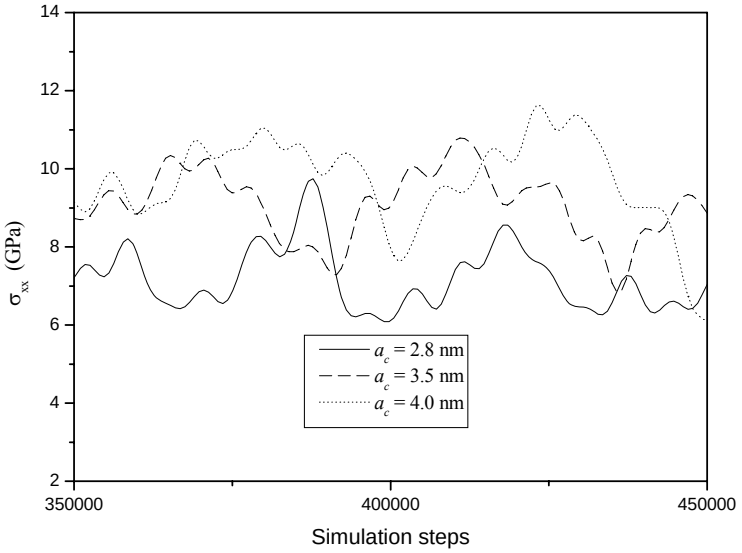

(a)

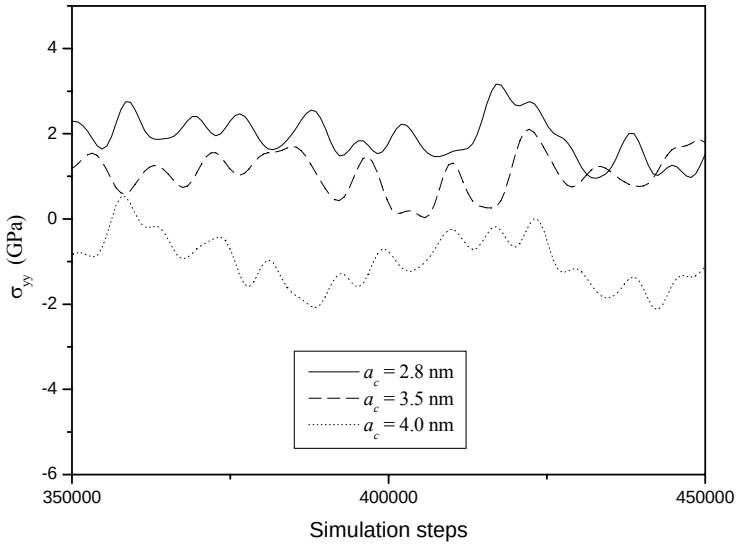

(b)

Figure 7.3 The variations of normal stresses (a) σ_{xx} and (b) σ_{yy} with the undeformed chip thickness at R = 3.5 nm.

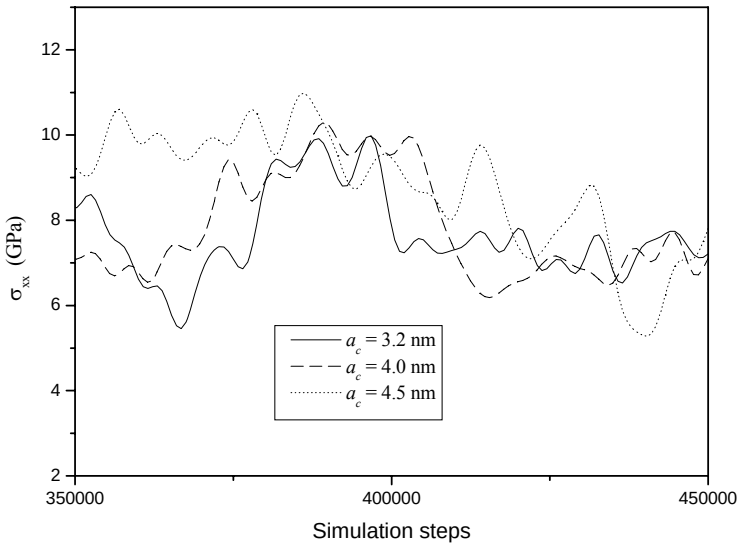

(a)

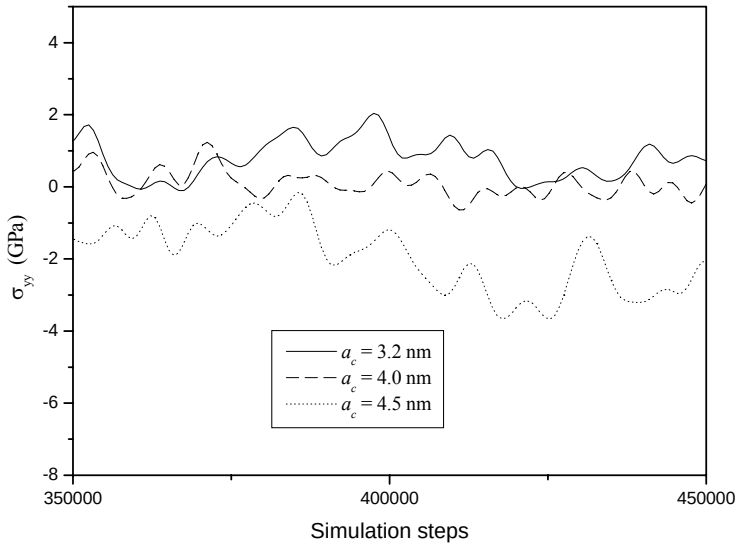

(b)

Figure 7.4 The variations of normal stresses (a) σ_{xx} and (b) σ_{yy} with the undeformed chip thickness at R = 4.0 nm.

can be seen that as the undeformed chip thickness increased from smaller to larger than the tool edge radius, σ_{xx} was positive (compressive stress) for all cases of undeformed chip thickness. The stress in the direction nearly perpendicular to the direction of crack initiation (see Figures 7.1 and 7.2), σ_{yy}, however, decreased as the undeformed chip thickness increased. When the tool cutting edge radius was 3.5 nm and undeformed chip thickness was 2.8 nm ($a_c/R<1$) and 3.5 nm ($a_c/R=1$), σ_{yy} was compressive stress (positive); when the tool cutting edge radius was 3.5 nm and undeformed chip thickness was 4.0 nm ($a_c/R>1$), σ_{yy} reduced to become tensile (negative). When the tool cutting edge radius was 4.0 nm and undeformed chip thickness was 3.2 nm ($a_c/R<1$), σ_{yy} was still compressive stress; when the tool cutting edge radius was 4.0 nm and undeformed chip thickness was 4.0 nm ($a_c/R=1$), σ_{yy} was nearly zero; when the tool cutting edge radius was 4.0 nm and undeformed chip thickness was 4.5 nm ($a_c/R>1$), σ_{yy} also reduced to be tensile stress. Therefore, when the undeformed chip thickness is smaller than the tool cutting edge radius, σ_{yy} will decrease when the tool cutting edge radius increases, and it can change to be tensile stress, as shown in Chapter 6. However, when the undeformed chip thickness is larger than the tool cutting edge radius, σ_{yy} is tensile.

7.3.3 The Crack Initiation Zone

When the undeformed chip thickness was smaller than the tool cutting edge radius ($a_c/R<1$), no peak deformation zone occurred in the chip formation zone. In this condition, when the stress σ_{yy} was compressive, the workpiece material next to the chip formation zone was purely compressive stressed. Therefore, there was no crack initiation, as shown in Figure 7.5(a). When the stress σ_{yy} was tensile stress in this

condition, as shown in Figure 7.5(b), there was still no crack initiation as long as the tool cutting edge radius was below the upper bound (see Chapter 6).

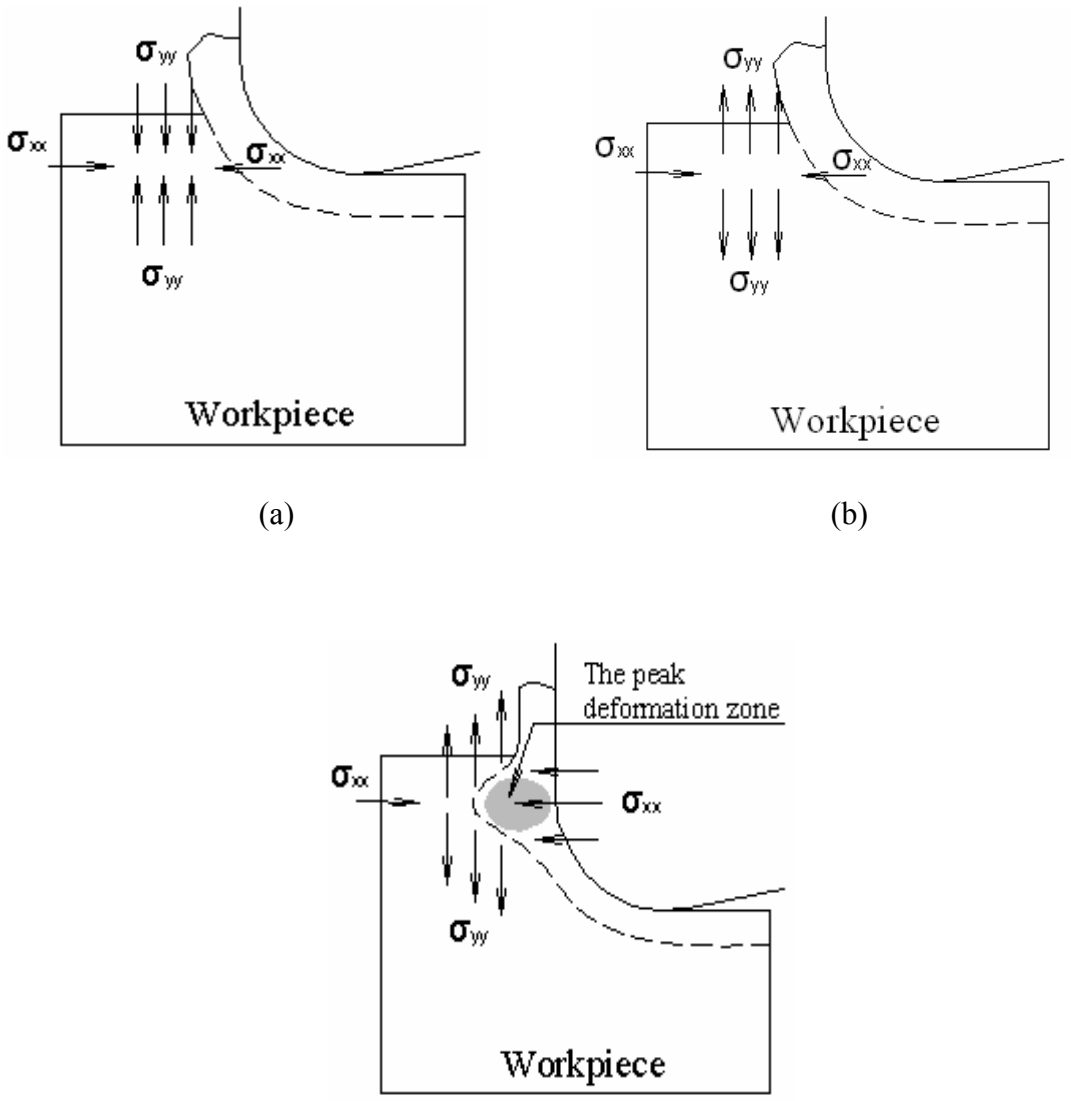

Figure 7.5 Two different chip formation modes: (a) and (b) ductile mode, (c) brittle mode.

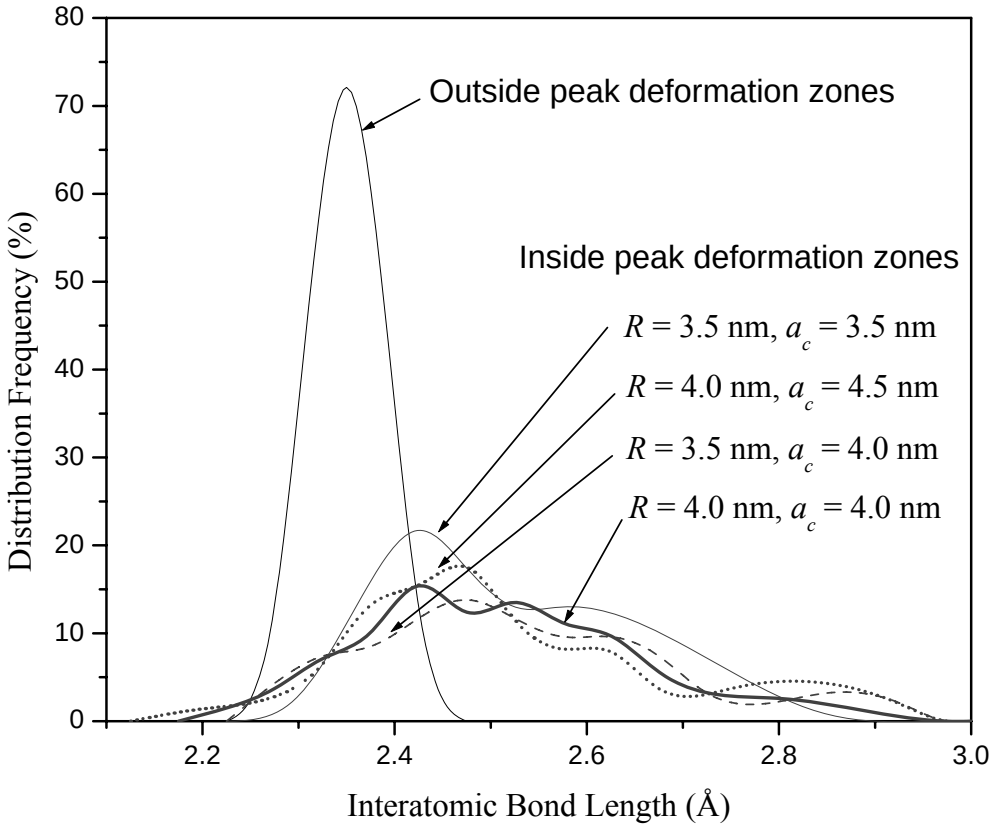

Figure 7.6 The distribution frequency of interatomic bond length.

In contrast, as shown in Figure 7.5(c), when the undeformed chip thickness was equal to or larger than the tool cutting edge radius ($a_c/R \geq 1$), there was a peak deformation zone generated in the chip formation zone. Figure 7.6 shows the distribution frequency of interatomic bond length, where the bond length is the distance between two atoms. From Figure 7.6, it can be seen that the interatomic bond lengths in the peak deformation zones under the conditions of $a_c/R \geq 1$ (see Figure 7.1(b, c) and Figure 7.2(b, c)) were in the range from 2.4 to 3.0 Å, whereas outside the peak deformation zone the interatomic bond lengths were about 2.35 Å, that is, the interatomic bond lengths in the peak deformation zone became longer. Due to the increase of interatomic bond length, the volume of material in the peak deformation zone was

expanded. Unlike ductile materials, which have much larger fracture strains, silicon is a kind of brittle material with extremely small fracture strain. As a result, with the tensile stress in the *y* direction and compressive stress in the *x* direction (see Figure 7.5(c)), the workpiece material will be split, initiating a crack in the material next to the peak deformation zone, forming a crack initiation zone next to the peak deformation zone. In this crack initiation zone, the crack would be formed, which propagates along the direction of crack initiation – from the connecting point of tool rake face and edge arc to the deformation peak of chip formation (see Figure 7.1 and 7.2). This explains the phenomena that in nanoscale cutting of silicon as the undeformed chip thickness is larger than the tool cutting edge radius (that is, the ratio of undeformed chip thickness to tool cutting edge radius a_c/R is increased from $a_c/R < 1$ to $a_c/R > 1$), crack initiation and propagation occur and the chip formation is in a brittle mode.

7.4 Concluding Remarks

In this chapter, MD method has been used to study crack initiation in nanoscale cutting of monocrystalline silicon. For the first time, a peak deformation zone in the chip formation zone has been found in the transition from ductile mode to brittle mode cutting as the undeformed chip thickness is increased from smaller to larger than the tool cutting edge radius. The results showed that as the undeformed chip thickness is larger than the cutting edge radius, in the chip formation zone there is a peak deformation zone in association with the connecting point of the tool rake face and tool edge arc. The interatomic bond length's increase in the peak deformation zone results

in the volume expansion of the zone, which could cause the material next to the zone to become tensile stressed, leading to crack initiation in the material. When the undeformed chip thickness is smaller than the cutting edge radius, there is no peak in the chip formation zone, and there is no crack initiation zone in the undeformed workpiece material. The findings explain well the phenomena of ductile-brittle transition as the undeformed chip thickness is increased from smaller to larger than the tool cutting edge radius (that is, the ratio of undeformed chip thickness to tool cutting edge radius a_c/R is increased from $a_c/R < 1$ to $a_c/R > 1$).

Chapter 8

Mechanism of Diamond Tool Groove Wear

8.1 Introduction

Li et al. (2005) studied the diamond tool wear characteristics in nanoscale ductile mode cutting of monocrystalline silicon and the effects of tool wear on the chip formation mode. In that study, the cutting tool was natural diamond with a perfect lattice. It was shown that in nanoscale ductile mode cutting of monocrystalline silicon wafers, micro/nano groove wear could be observed on the cutting tool flank (see Figure 8.1). These grooves form sub-cutting edges of much smaller radii on the main cutting edge and may consequently affect the mode of ductile chip formation.

In conventional cutting processes, such as cutting of metallic alloys, the groove wear of tool flank face is usually caused by abrasion (Trent, 1977), in which hard particles (carbide, nitride or oxide) in the workpiece material abrade the tool face and form grooves on it. Since a monocrystalline silicon body is supposedly free of hard particles, and the diamond cutting tool material is much harder than the monocrystalline silicon at room temperature, the generation of grooves in nanoscale cutting of monocrystalline silicon with diamond tools is beyond the understanding based on conventional cutting processes. In order to study the mechanism of groove generation, the molecular dynamics (MD) method was used to simulate the naonoscale cutting process of

monocrystalline silicon with monocrystalline diamond cutting tools. Based on the simulated temperature and the deformation characteristics of workpiece in the cutting region, a possible formation mechanism of groove wear has been proposed.

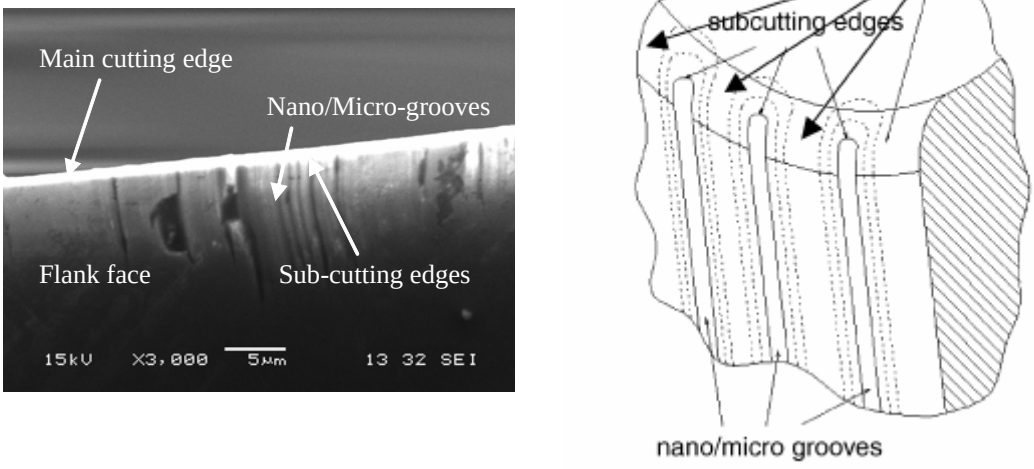

(a) (b)

Figure 8.1 (a) SEM photographs of the tool flank face after ductile mode cutting, showing micro/nano grooves on the diamond tool flank face; (b) Sub-cutting edges of much smaller edge radii formed on the main cutting edge by the micro/nano grooves at the tool flank.

8.2 MD Simulation Condition

In the simulation for the nanoscale ductile cutting of monocrystalline silicon, the dimensions of the silicon workpiece used were $30a \times 20a \times 4a$. The working environment temperature was set at 293 K.

A simulation case, where the undeformed chip thickness a_c was set at 2.0 nm and the tool cutting edge radius R was 2.5 nm was first conducted. Based on the result of this

simulation case, a new concept of “dynamic hard particles” was proposed to explain the groove wear.

In order to further study the characteristics of “dynamic hard particles”, additional four simulation cases were also conducted. The cutting speed v_c was set at 20 m/s in the first three cases. In the first case, the tool cutting edge radius R = 3.5 nm and the undeformed chip thickness of a_c = 2.8 nm were used. In the second one, the tool cutting edge radius R was still 3.5 nm and the undeformed chip thickness a_c was reduced to 2.0 nm. In the third case, the tool cutting edge radius R was increased to 4.0 nm, but the undeformed chip thickness a_c was 2.8 nm, the same as the value in the first case. In order to check the effect of cutting speed, in the last case, only the cutting speed was changed to 40 m/s, but both the tool cutting edge radius and the undeformed chip thickness were the same as those in the first case.

8.3 A Possible Mechanism of Diamond Tool Groove Wear

8.3.1 Temperature Rise and Its Effect on the Diamond Tool

In Figure 8.2, *A* and *B* zones are near the interface of the tool and workpiece. Zone *A* is near the arc part of the tool cutting edge and zone *B* is under the flank face of the tool. Zone *C* is relatively far from the machined surface. Figure 8.3 shows the temperature variations of deformation zones *A*, *B* and *C* in the workpiece. It can be seen that the temperature in zone *C* was stable and its value was about 315 K, which was near the work environment temperature (293 K) set in the MD simulation. In zone *B*, the material deformation tended to be intensive and the temperature was increased,

varying in a range of 320 K – 512 K. In zone *A*, the average temperature was 550 K, which was the highest among those in the three zones, and the peak could reach 725 K. These could be due to the workpiece material in zone *A* being deformed at the highest rate.

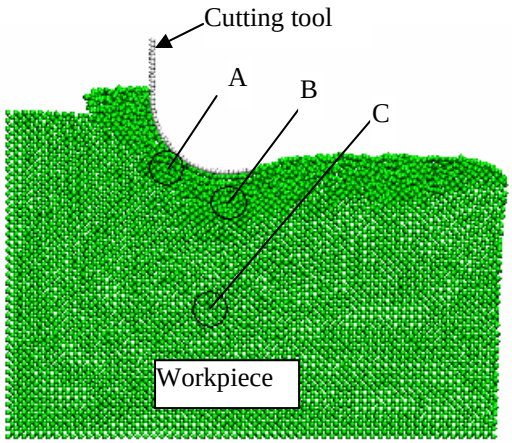

Figure 8.2 The different deformation zones in the workpiece.

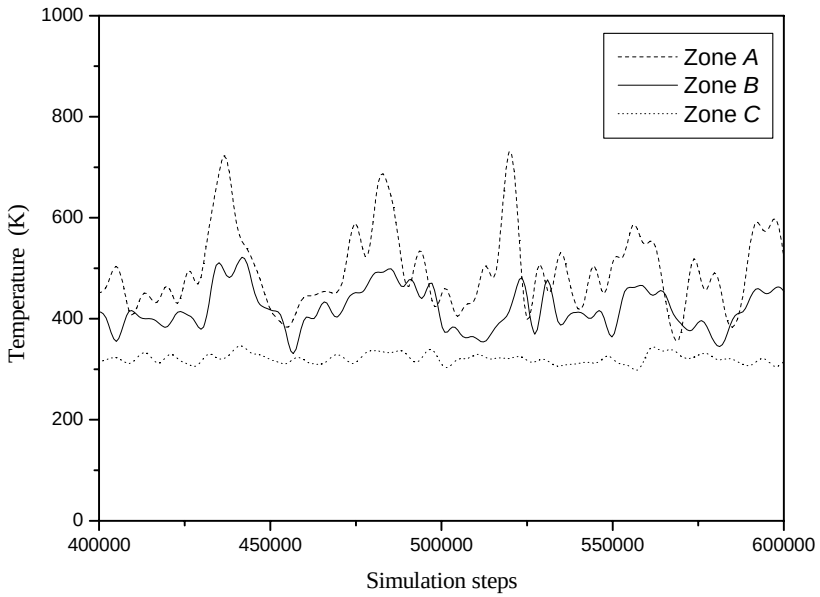

Figure 8.3 The temperature variations of deformation zones *A*, *B* and *C* in the workpiece.

It should be noted that the fluctuations of temperature in the deformation zones, especially in zone *A*, were due to the stress and strain fluctuations as a result of deformation in the zones formed by limited number of atoms. Figure 8.4 showed the stress variations in deformation zone *A* of the workpiece. Comparing Figure 8.3 with Figure 8.4, it can be seen that at steps of about 430000, 480000, and 512000, the stresses and the temperature in zone *A* nearly simultaneously reached the peak value.

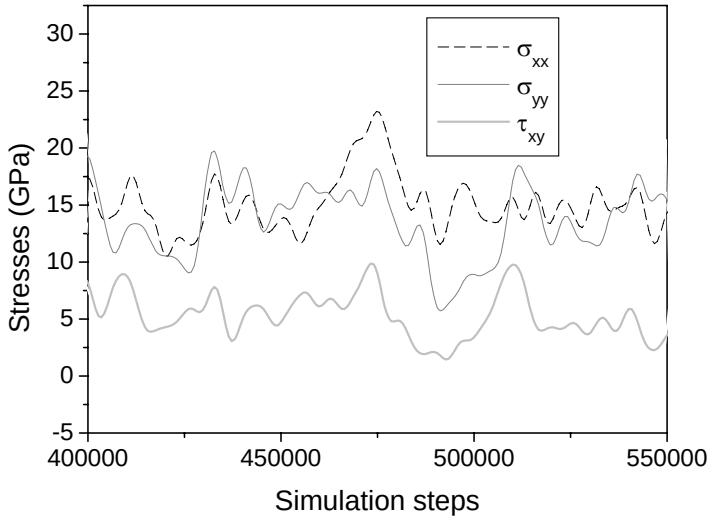

Figure 8.4 The stresses variations of deformation zone *A* in the workpiece.

Consider that the tool and workpiece are in intimate contact. The tool surface temperature would be the same as the workpiece temperature at the interface. Since diamond is a good conductor, the temperature at the subsurface immediately below the surface layer (on scale of the groove wear sizes) should be very close to the surface temperature. The chemical stability of diamond decreases with temperature increasing. For example, as the temperature increases above 473 K, a layer of oxide forms on the diamond, from which, starting at about 623 K, carbon oxides evolve (Bakon and Szymanski, 1992). Therefore, the temperature in zones *A* and *B* was sufficient to lead to the generation of carbon oxides on the diamond cutting tool. Since the carbon oxides

are surely softer than the original diamond, the hardness of the diamond cutting tool edge could be reduced during cutting.

Experimental results (Field, 1979) showed that the temperature rise can directly lead to the decrease of diamond's hardness. Figure 8.5 shows the effect of temperature on the hardness of diamond. It can be seen that the hardness decrease from about 75 GPa to 57 GPa, which is very significant, when the temperature increases from 300 K to 550 K. If the temperature is at the peak 725 K, the diamond hardness would even decrease to 48 GPa. Therefore, the effect of temperature on the diamond hardness can be a significant factor that softens the tool during cutting.

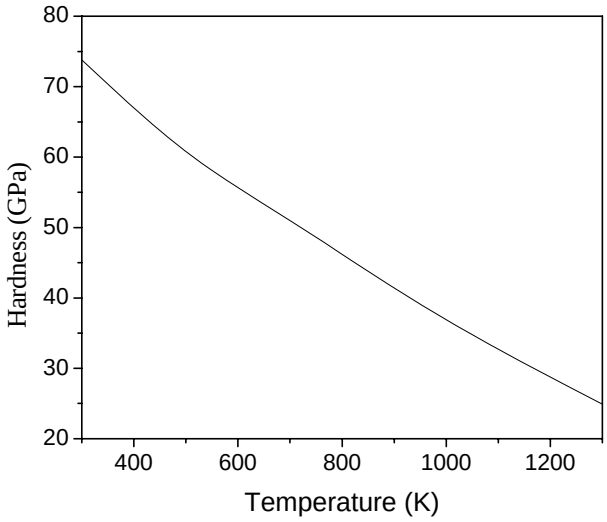

Figure 8.5 Effect of temperature on the hardness of diamond (Field, 1979).

8.3.2 Material Phase Transformation and its Effect on the Diamond Tool

In Chapter 5, the results of MD simulations of nanoscale cutting of silicon showed that because of the high hydrostatic pressure in the chip formation zone, there is a phase

transformation of the monocrytslline silicon from diamond cubic structure to both β silicon and amorphous phase in the chip formation zone.

Figure 8.6 shows the output result of the present simulation. The silicon workpiece can be divided into a chip formation zone and an undeformed workpiece material zone. In the undeformed workpiece material zone, the silicon atoms were regularly arranged. In the chip formation zone, the arrangement of the atoms was amorphous or β silicon as mentioned in Chapter 5.

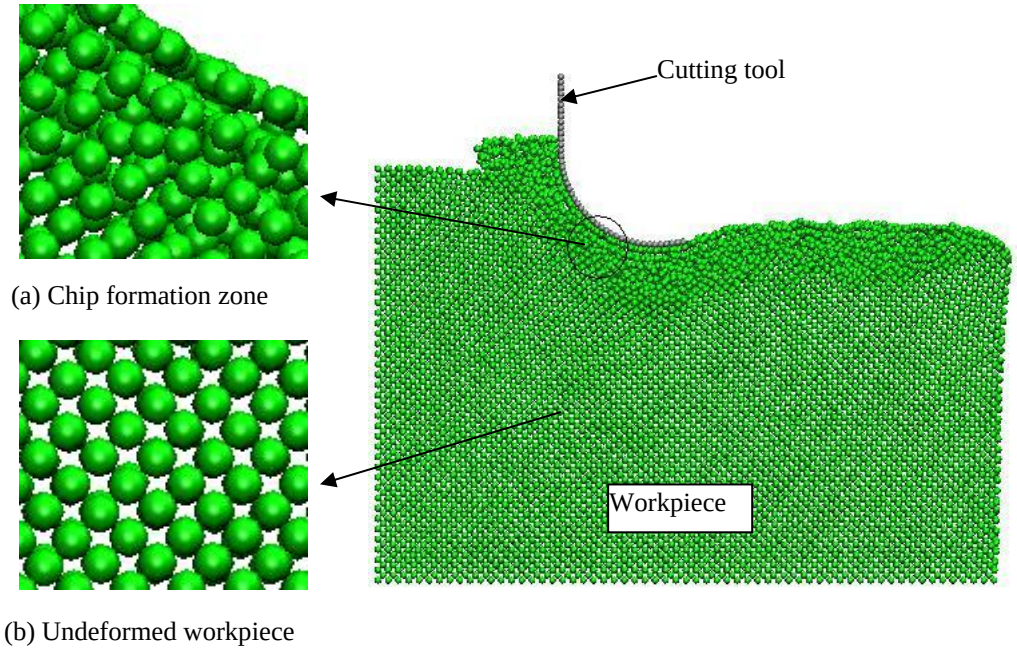

(a) Chip formation zone

(b) Undeformed workpiece

Figure 8.6 The output result of MD simulation, showing the amorphous phase and β phase of silicon in the chip formation zone and monocrystalline phase of silicon in undeformed workpiece material zone.

Figure 8.7(a) shows at a moment in cutting the distribution frequency of interatomic bond length of the workpiece material. Same as the conclusion in Chapter 5, in the undeformed workpiece material, the distribution of interatomic bond length

concentrated near the value of bond length L = 2.35 Å, and in the chip formation zone, the interatomic bond length varied in a wide range. However, from this figure it also can be seen that although most of the bond lengths became longer than the normal bond length, a small portion of bond lengths became shorter than the normal bond length.

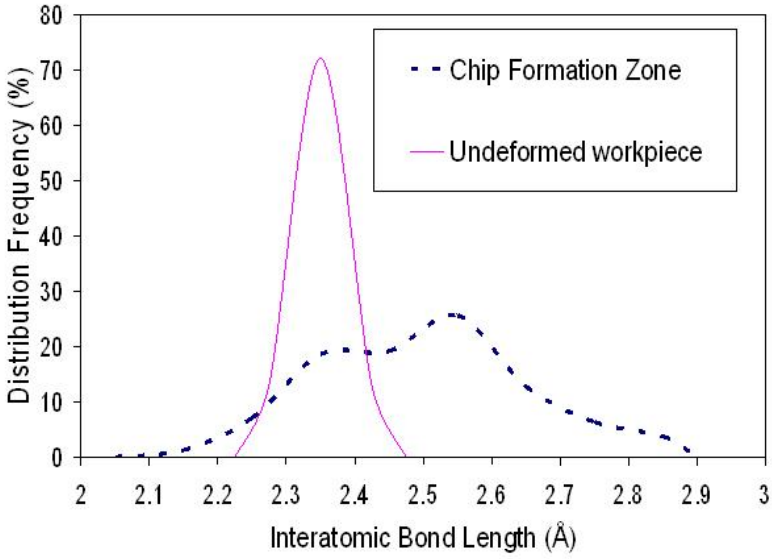

Figure 8.7 The distribution frequencies of interatomic bond length of the silicon workpiece material in the chip formation zone and undeformed workpiece material zone.

In Chapter 5, it has been indicated that for pure silicon, the hardness is inversely proportional to $L^{4.5}$, where L represents the interatomic bond length. Therefore, the shorter the bond lengths, the harder the silicon atom groups with these bond lengths. For example, when the bond length is shortened from 2.35 Å to 2.05 Å, the hardness will increase by 1.85 times. As a result, the silicon atom groups with the shorter bond lengths could have acted as “hard particles” in the chip formation zone, which have the hardness of a few times harder than the original hardness of silicon. Since these silicon atom groups with shorter bond lengths appear only in the chip formation zone under dynamic high hydrostatic pressure, they could be called “dynamic hard particles”.

Such “hard particle” could be observed in the chip formation zone from the MD simulation results, as shown in Figure 8.8, where the “hard particles” have atoms with the bond lengths shorter than 2.30 Å (smaller than the normal bond length of 2.35 Å) are marked.

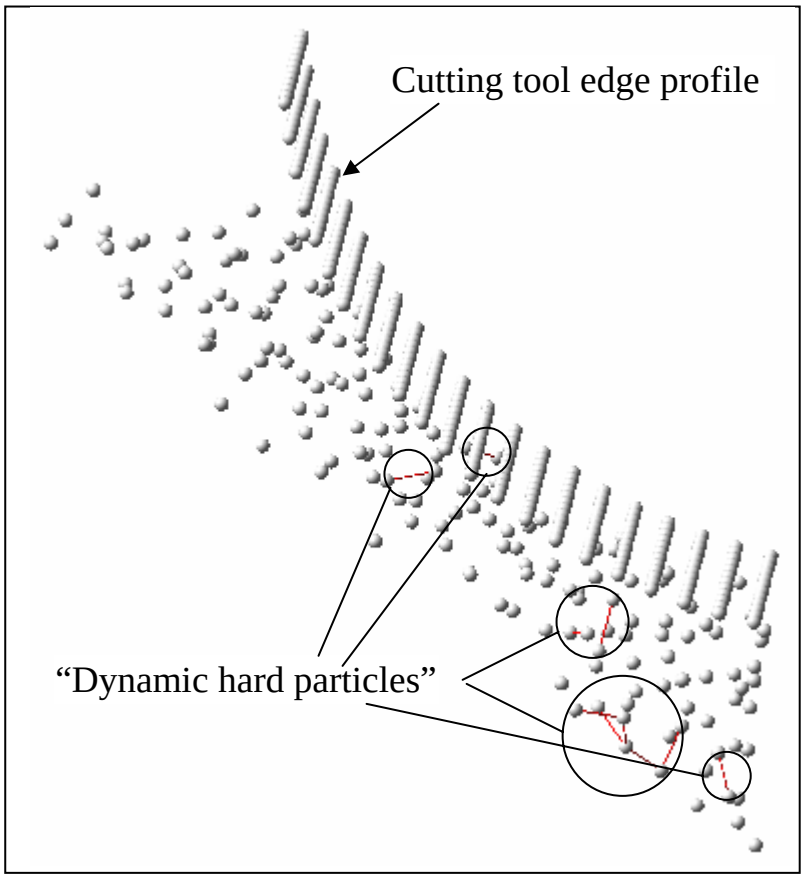

Figure 8.8 3-D representation of the chip formation zone having atom groups with shortened bond lengths (the line marks between the atoms indicate bond lengths shorter than 2.30 Å), showing the “dynamic hard particles” in the chip formation zone.

8.3.3 A Possible Formation Mechanism of Diamond Tool Groove Wear

As discussed in Section 8.3.1, the temperature in the chip formation zone will be increased during cutting, forming the carbon oxides on the diamond tool surface, which make the diamond softer than the original. Moreover, the increase of

temperature will directly result in the decrease of the diamond material hardness. On the other hand, as discussed in section 8.3.2, in the workpiece material, the phase transformation caused by high hydrostatic pressure creates atom groups with shortened bond lengths, forming “dynamic hard particles” that are a few times harder than the original silicon. As a result of the “dynamic hard particles” ploughing on the softened diamond tool flank face, micro/nano grooves are formed on the tool flank face.

8.4 Characteristics of “Dynamic Hard Particles”

Although the groove wear could be caused by the “dynamic hard particles” formed by the atom groups with much shorter bond lengths as a result of the workpiece material phase transformation from monocrystalline to amorphous and β silicon under the high pressure in the chip formation zone, the characteristics of such “dynamic hard particles” and the detailed mechanism of causing the groove wear by the “dynamic hard particles” are unknown. In order to further study the characteristics of “dynamic hard particles”, additional four simulation cases were conducted and the simulation condition has been given in Section 8.2.

8.4.1 “Dynamic Hard Particles” in the Chip Formation Zone

As a result of phase transformation in the chip formation zone, atom groups with shortened bond lengths were formed in addition to the atom groups with enlarged bond lengths. These were observed from the simulation tests under the four different conditions, as shown in Figure 8.9, which shows the distribution frequency of interatomic bond lengths of the silicon workpiece in the chip formation zone in

comparison to those in the undeformed workpiece material. From Figure 8.9, it can be seen that for all the four tests, in the chip formation zone, although most of the bond lengths became longer than the normal bond length (2.35 Å) in the undeformed workpiece material, a small portion of bond lengths became shorter or much shorter than the normal bond length. The silicon atom groups with the shortened bond lengths in the chip formation zone have been called “dynamic hard particles” in section 8.3.2, which have hardness a few times larger than the original hardness of silicon.

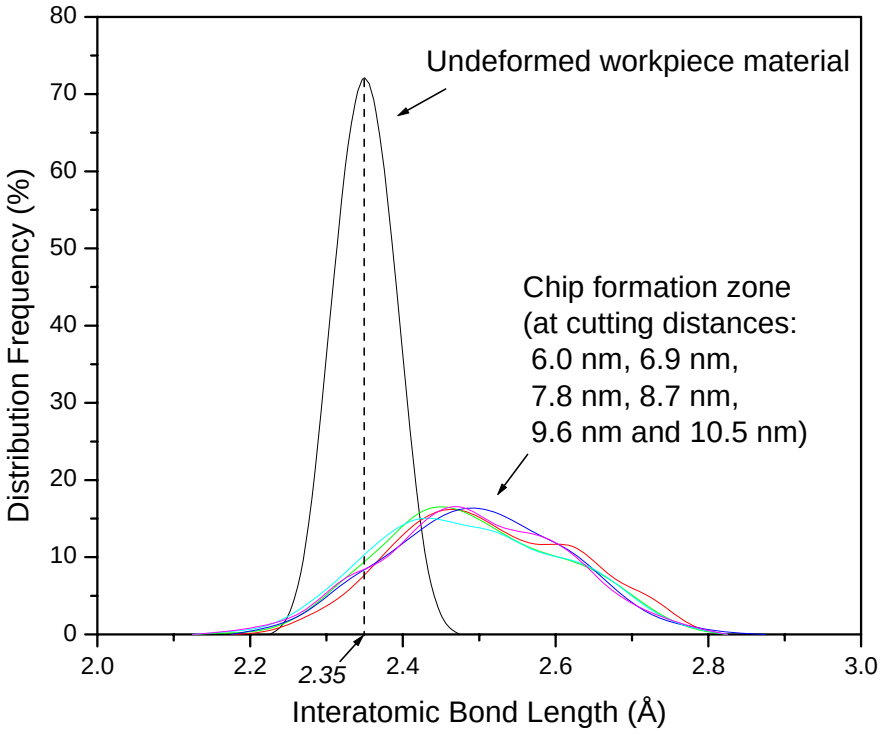

(a)

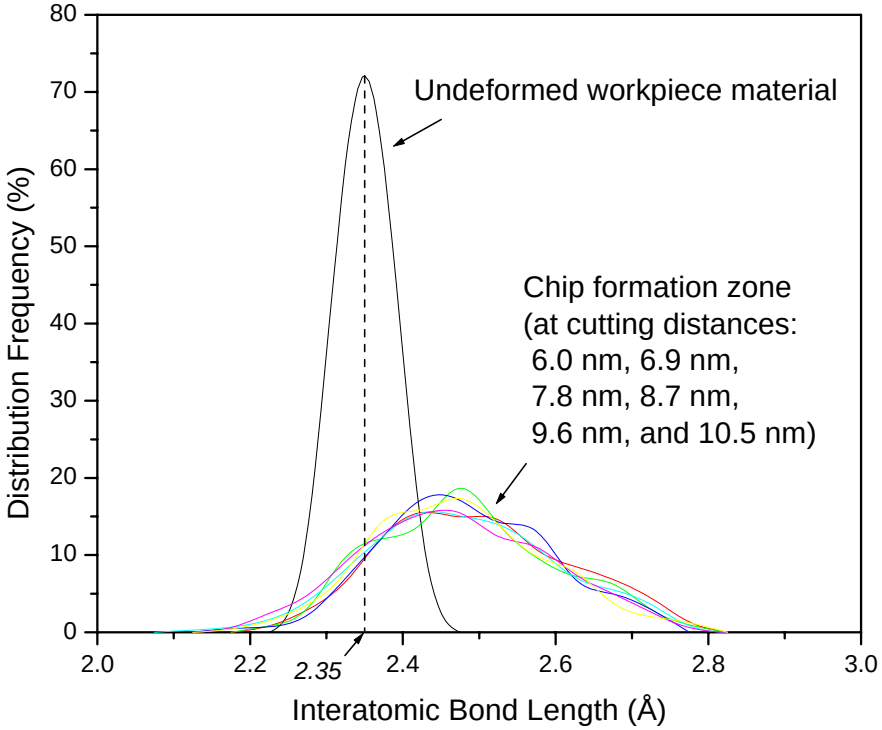
Undeformed workpiece material
Chip formation zone
(at cutting distances:
6.0 nm, 6.9 nm,
7.8 nm, 8.7 nm,
9.6 nm, and 10.5 nm)
Distribution Frequency (%)
Interatomic Bond Length (Å)
2.35
0
10
20
30
40
50
60
70
80
2.0
2.2
2.4
2.6
2.8
3.0

(b)

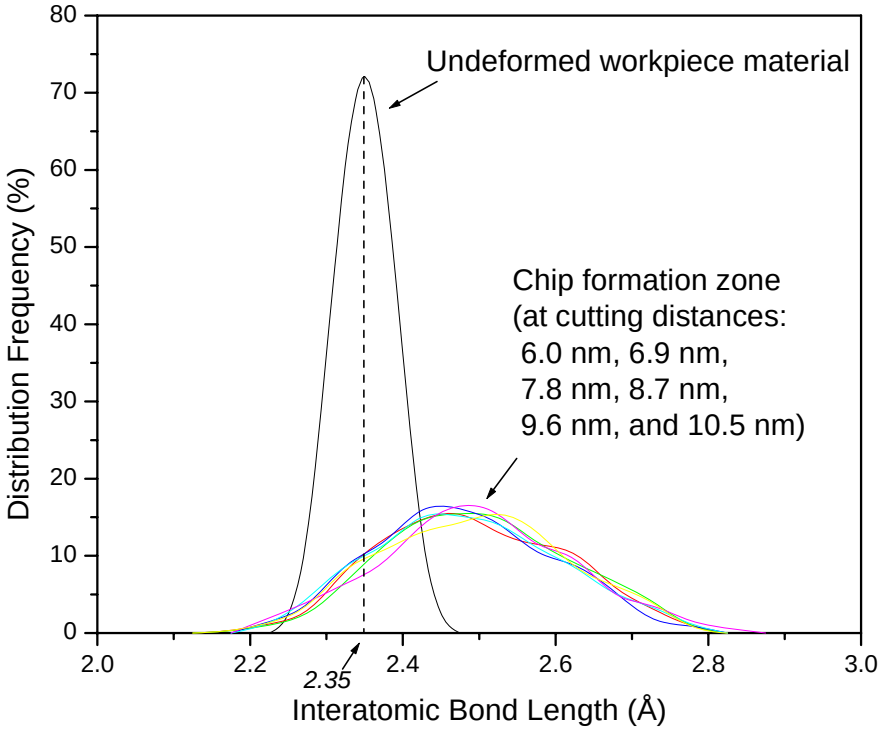
Undeformed workpiece material
Chip formation zone
(at cutting distances:
6.0 nm, 6.9 nm,
7.8 nm, 8.7 nm,
9.6 nm, and 10.5 nm)
Distribution Frequency (%)
Interatomic Bond Length (Å)
2.35
0
10
20
30
40
50
60
70
80
2.0
2.2
2.4
2.6
2.8
3.0

(c)

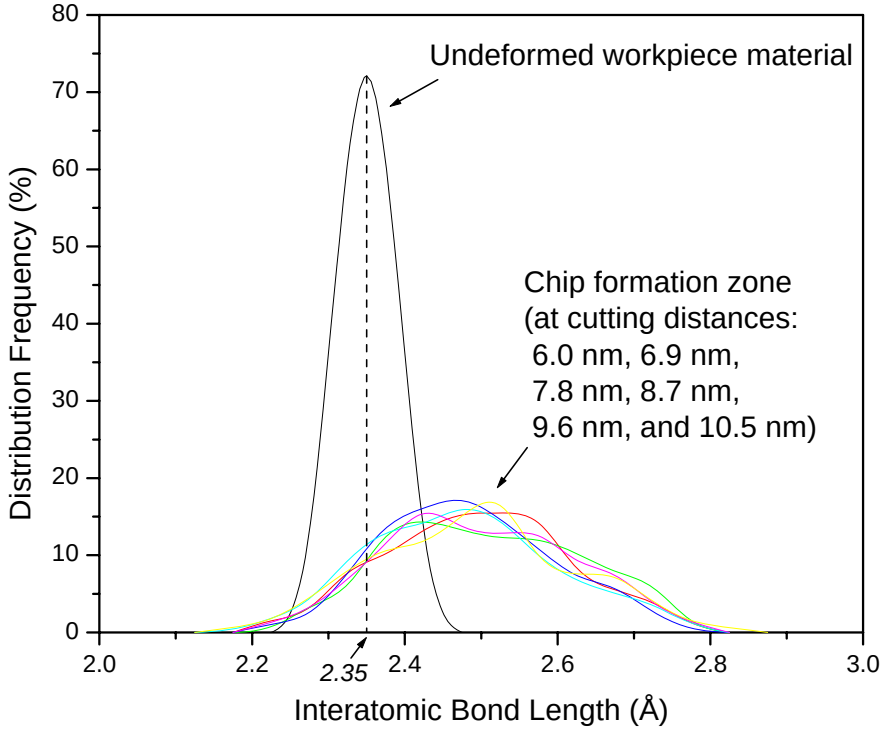

(d)

Figure 8.9 The distribution frequency of interatomic bond length of the silicon workpiece for cutting at different conditions: (a) R = 3.5 nm, a_c = 2.8 nm, v_c = 20 m/s, (b) R = 3.5 nm, a_c = 2.0 nm, v_c = 20 m/s, (c) R = 4.0 nm, a_c = 2.8 nm, v_c = 20 m/s, (d) R = 3.5 nm, a_c = 2.8 nm, v_c = 40 m/s.

8.4.2 The Distribution of "Dynamic Hard Particles"

The distributions of the "dynamic hard particles" in the chip formation zone in the tests under the four different simulation conditions are shown in Figure 8.10. In each of the figures (a) to (d), the distribution of the "dynamic hard particles" at six different cutting distances, 6.0 nm, 6.9 nm, 7.8 nm, 8.7 nm, 9.6 nm, and 10.5 nm, are shown. According to the distribution of these short bonds, they are divided into two portions - one is the upper portion and the other is the lower portion, and the number of bonds with bond length shorter than 2.30 Å in each portion is marked in these figures.

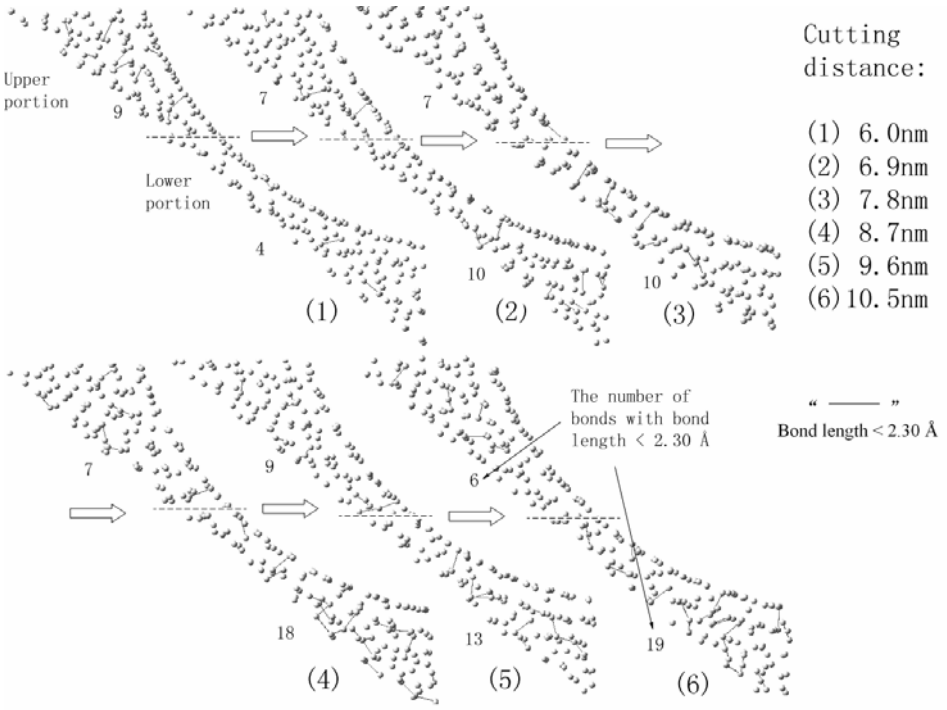
Upper portion
Lower portion
Cutting distance:
(1) 6.0nm
(2) 6.9nm
(3) 7.8nm
(4) 8.7nm
(5) 9.6nm
(6) 10.5nm
The number of bonds with bond length < 2.30 Å
" ——— "
Bond length < 2.30 Å

(a)

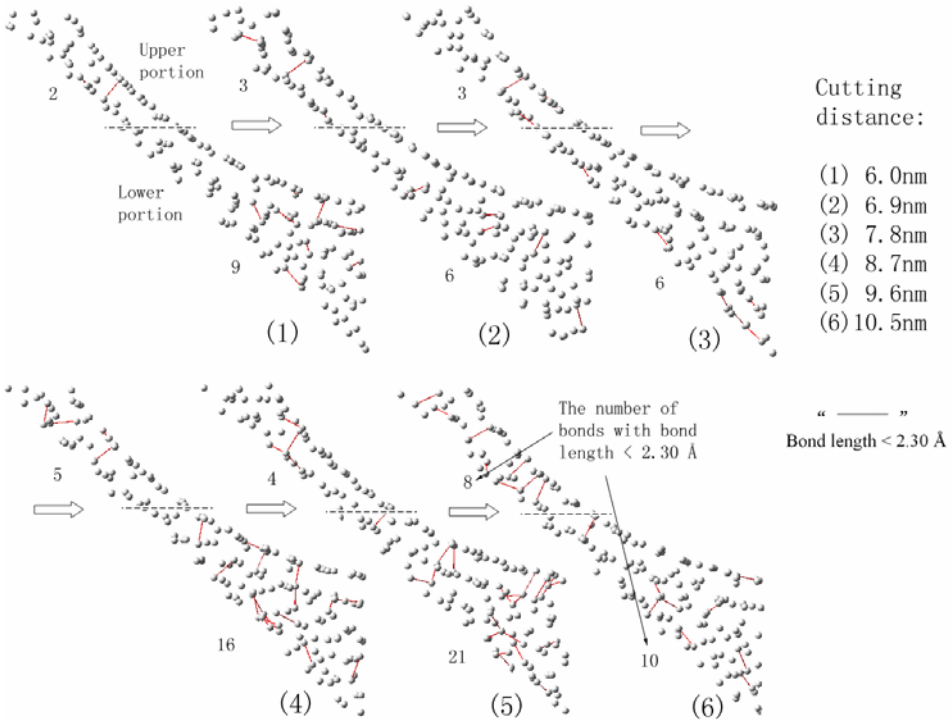
Upper portion
Lower portion
Cutting distance:
(1) 6.0nm
(2) 6.9nm
(3) 7.8nm
(4) 8.7nm
(5) 9.6nm
(6) 10.5nm
The number of bonds with bond length < 2.30 Å
" ——— "
Bond length < 2.30 Å

(b)

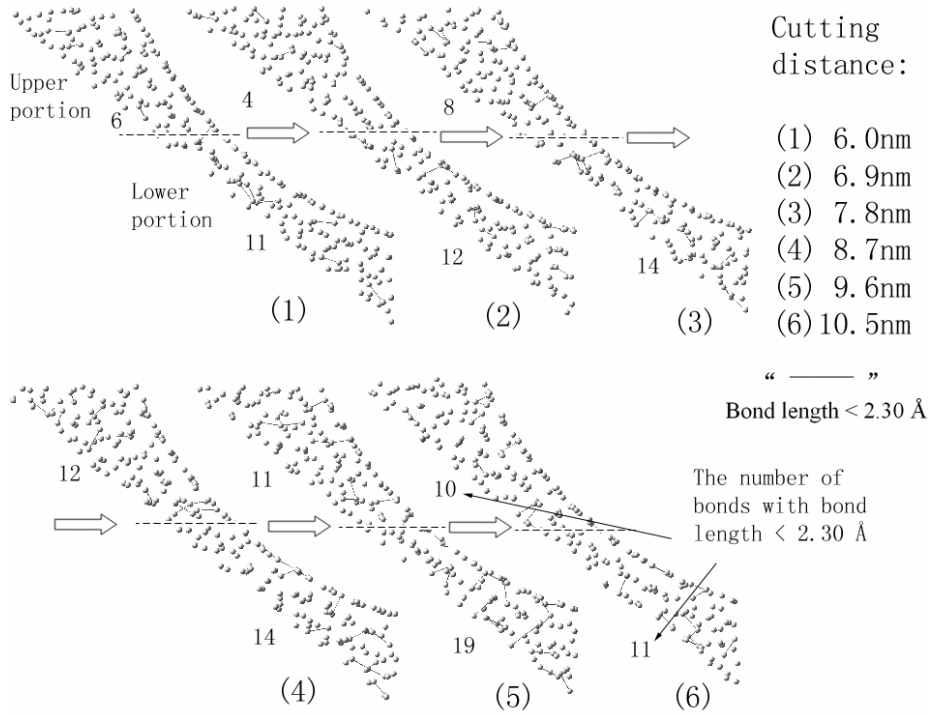

(c)

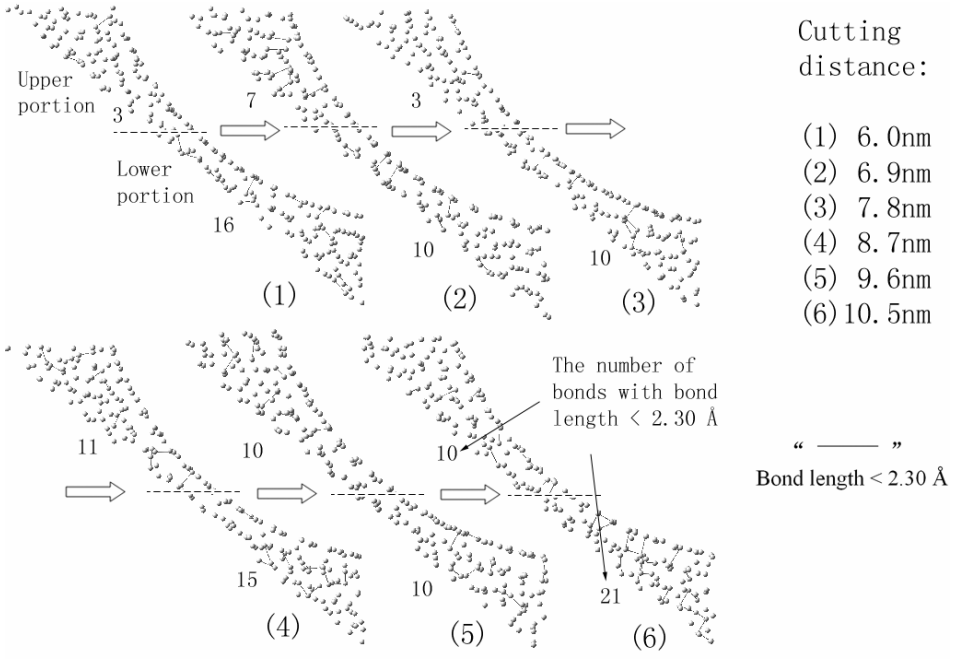

(d)

Figure 8.10 The distribution of "dynamic hard particles" for cutting at different conditions: (a) R = 3.5 nm, a_c = 2.8 nm, υ_c = 20 m/s, (b) R = 3.5 nm, a_c = 2.0 nm, υ_c = 20 m/s, (c) R = 4.0 nm, a_c = 2.8 nm, υ_c = 20 m/s, (d) R = 3.5 nm, a_c = 2.8 nm, υ_c = 40 m/s.

From these figures, three characteristics of the "dynamic hard particles" can be observed. First, in the entire cutting process, the distribution is dynamic and changes over time and cutting stages. Second, in each cutting stage, the distribution is uneven in the entire chip formation zone. By comparing the numbers in the upper portion and in the lower portion, the third characteristic can be observed, which is that the "dynamic hard particles" are mostly distributed in the lower portion of chip formation zone. This could be due to the larger compressive stress in the lower portion of the chip formation zone. The results in Chapter 6 show that in the ductile mode cutting, the average compressive stresses in the upper portion and in the lower portion of chip formation zone were about 8 GPa and 20 GPa, respectively.

8.4.3 The Characteristics of the "Dynamic Hard Particles" in Relation to Diamond Tool Groove Wear

As described in Section 8.3.2, the "dynamic hard particles" in the chip formation zone may have hardness a few times larger than the original hardness of the silicon workpiece. Since the "dynamic hard particles" are mainly distributed in the lower portion of the chip formation zone, as reported in Section 8.4.2, these "particles" of greater hardness may flow into the tool flank-workpiece interface and form three body abrasions, causing groove wear at the tool flank. The experimentally observed micro/nano groove wear at the tool flank, as shown in Figure 8.1, can be a firm evidence of such a relationship between the distribution of the "dynamic hard particles" and the tool flank wear.

The experimental results presented by Li et al. (2005) further showed that the locations of grooves on the tool flank face were not determinate. This may be explained by the

first characteristic of the “dynamic hard particles”: the distribution of the “particles” is dynamic and changes over time and cutting stages, as described in section 8.4.2. During the cutting process, since the tool grooves were caused by the “dynamic hard particles” and the distribution of “dynamic hard particles” was changing, the locations of grooves at the tool flank face were also uncertain.

8.5 Concluding Remarks

In this chapter, MD method has been applied to simulate the ductile mode cutting of silicon to investigate the mechanism of micro/nano diamond tool groove wear formation in ductile mode cutting of monocrystalline silicon with a diamond tool.

The results of the first simulation case showed that the temperature rise in the chip formation zone could soften the material at the flank face of the diamond cutting tool. Also, the high hydrostatic pressure in the chip formation region could result in the workpiece material phase transformation, in which the material interatomic bond length varies, yielding atom groups of much shorter bond lengths. Such atom groups could be many times harder than that of the original monocrystalline silicon and could act as “dynamic hard particles” in the material. Having the “dynamic hard particles” ploughing on the softened flank face of the diamond tool, the micro/nano grooves could be formed, yielding the micro/nano groove wear as observed.

In order to investigate the characteristics of the “dynamic hard particles” in nanoscale ductile mode cutting of monocrystalline silicon with diamond tools as well as their

relationship with the tool groove wear, additional four simulation cases were conducted. Some tentative conclusions can be drawn as follows:

- The “dynamic hard particles” have a dynamic and uneven distribution over the entire chip formation zone. The distribution changes over time and cutting stages.

- The “dynamic hard particles” are mostly distributed in the lower portion of chip formation zone. Such a distribution causes micro/nano groove wear at the tool flank through three body abrasions.

- The dynamic distribution of the “dynamic hard particles” results in the uncertainty of the groove wear locations at the tool flank.

Chapter 9

Conclusions

9.1 Conclusions of the Research

In this research, a molecular dynamics (MD) model and a simulation system have been developed as a tool to study the nanoscale ductile mode cutting of monocrystalline silicon. The aspects that have been investigated in this research include the following: the effects of tool cutting edge radius, the mechanism of ductile chip formation, the upper bound of tool cutting edge radius, the crack initiation in relation to undeformed chip thickness, and the mechanism of diamond tool groove wear.

The conclusions of this research are summarized as follows:

1) A realistic MD model taking into account the effect of tool cutting edge radius on the chip formation and cutting characteristics has been developed. In this model, the initial atom positions of silicon workpiece material are arranged according to the crystal lattice structure, the atomic interactive actions of silicon are based on the Tersoff potential, the diamond cutting tool is assumed to be undeformable, and the motions of the atoms in the chip formation zone are determined by the Newton's equation of motion.

2) Different cutting tool edge radii and different cutting directions were applied to simulate the cutting process. Furthermore, an experiment was conducted to verify the MD model. The simulated variation of the cutting forces with the tool cutting edge radius was compared with the cutting force results from experimental cutting tests. The good agreement of results indicated that the present MD model and simulation system can be used for simulation of the nanoscale ductile mode cutting of silicon. The MD simulation results showed that in nanoscale ductile mode cutting of silicon the thrust force is much larger than the cutting force and the stress in the cutting process is not uniformly distributed along the cutting tool edge. In the simulation, the elastic spring-back of small thickness was observed on the machined workpiece surface. Moreover, the results showed that the cutting direction has no obvious effects on the cutting forces and deformation of workpiece.

3) The mechanism of ductile chip formation has been explained based on the study of phase transformation in the ductile cutting of monocrystalline silicon. The results of MD simulations of nanoscale cutting of silicon showed that because of the high hydrostatic pressure in the chip formation zone, there is a phase transformation of the monocrytslline silicon from diamond cubic structure to both β silicon and amorphous phase in the chip formation zone, which results in plastic deformation of the work material in the chip formation zone as observed in experiments. The results further showed that although from experimental observation the plastic deformation in the ductile mode cutting of silicon is similar to that in cutting of ductile materials, such as aluminum, in

ductile mode cutting of silicon it is the phase transformation of silicon rather than atomic dislocation that results in the plastic deformation.

4) The experimental phenomenon that there is an upper bound of tool cutting edge radius in nanoscale ductile mode cutting of silicon has been explained. In this thesis, based on the tensile stress distribution and the characteristics of the distribution obtained from molecular dynamics (MD) simulation of nanoscale ductile cutting of silicon, an approximation for the tensile stress distribution was obtained. Using this tensile stress distribution with the principles of geometrical similarity and fracture mechanics, the critical conditions for the crack initiation have been determined. The result showed that there is a critical tool cutting edge radius, beyond which crack initiation can occur in the nanoscale cutting of silicon and the chip formation mode is transferred from ductile to brittle. That is, this critical tool cutting edge radius is the upper bound of the tool cutting edge radius for ductile mode cutting of silicon.

5) The crack initiation in the ductile-brittle mode transition as the undeformed chip thickness is increased from smaller to larger than the tool cutting edge radius has been studied using the MD method on nanoscale cutting of monocrystalline silicon with a non-zero edge radius tool, from which, for the first time, a peak deformation zone in the chip formation zone has been found in the transition from ductile mode to brittle mode cutting. The results show that as the undeformed chip thickness is larger than the cutting edge radius, in the chip formation zone there is a peak deformation depth in association with the connecting point of tool edge arc and the rake face, and there is a crack

initiation zone in the undeformed workpiece next to the peak deformation zone, in which the material is tensile stressed and the tensile stress is perpendicular to the direction from the connecting point to the peak. As the undeformed chip thickness is smaller than the cutting edge radius, there is no deformation peak in the chip formation zone, and there is no crack initiation zone formed in the undeformed workpiece. This finding explains well the ductile-brittle transition as the undeformed chip thickness increases from smaller to larger than the tool cutting edge radius.

6) A new concept of "dynamic hard particles" was proposed to investigate the mechanism of micro/nano groove wear formation in ductile mode cutting of monocrystalline silicon with a diamond tool. The results showed that the temperature rise in the chip formation zone could soften the material at the flank face of the diamond cutting tool. Also, the high hydrostatic pressure in the chip formation region could result in the workpiece material phase transformation, in which the material interatomic bond length varies, yielding atom groups of much shorter bond lengths. Such atom groups could be many times harder than that of the original monocrystalline silicon and could act as "dynamic hard particles" in the material. Having the "dynamic hard particles" ploughing on the softened flank face of the diamond tool, the micro/nano grooves could be formed, yielding the micro/nano groove wear as observed. These "dynamic hard particles" have a dynamic and uneven distribution over the entire chip formation zone. Their distribution changes over time and cutting stages. Moreover, they are mostly distributed in the lower portion of chip formation zone. These characteristics of the "dynamic hard particles" in

nanoscale ductile mode cutting of monocrystalline silicon causes micro/nano groove wear at the tool flank through three body abrasions and its uncertainty of the groove wear locations at the tool flank.

9.2 Recommendation for Future Work

Up to now, nearly all the MD simulations simulate defect-free materials, but actually it is impossible and all real materials should have defects, such as voids, dislocations, cracks, and so on. As shown in Figure 8.1, due to the existence of defects, it is inevitable that there is some relationship between the defects and the mechanism of brittle-ductile transition in the nanocale cutting. Therefore, it is necessary to introduce the defects into the workpiece in the simulation. Moreover, at present, most of the simulations of brittle materials concentrate on the study of silicon. The study should be extended to more brittle materials, such as glass, quartz, and ceramics.

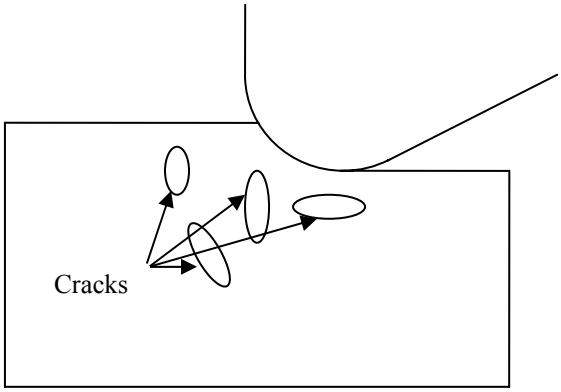

Figure 9.1 The workpiece with cracks.

In this research, the material deformation in the chip formation zone has been investigated, but a little wok has been done to study the chip formation, the chip

velocity, etc. Because the undeformed chip thickness is on the nanoscale, the chip size is also very small, like dust. This makes it very difficult to observe and study the chip in the experimental cutting process. MD simulation might be a good way to study the chip.

Although the tool wear has been studied, in the present MD model, the diamond cutting tool is considered infinitely hard. Therefore, tool deformation is neglected. In order to further study tool wear, the tool atoms can be movable. This will be helpful to directly observe and study the tool wear.

More measures should be taken to reduce the computing time. One limitation of MD method is that it needs a long time to finish the running of one case. Other than using better hardware, some new numerical techniques can be applied to improve the simulation system to reduce the computing time, such as parallel arithmetic and nerval network.

List of Publications from This Study

International Journal Papers:

M.B. Cai, X.P. Li and M. Rahman, Study of the mechanism of nanoscale ductile mode cutting of silicon using molecular dynamics simulation, *International Journal of Machine Tools & Manufacture*, Vol. 47, pp.75-80, 2007.

M.B. Cai, X.P. Li, M. Rahman and A.A.O. Tay, Crack initiation in relation to the tool edge radius and cutting conditions in nanoscale cutting of silicon, *International Journal of Machine Tools & Manufacture*, Vol. 47, pp.562-569, 2007.

M.B. Cai, X.P. Li and M. Rahman, Study of the mechanism of groove wear of the diamond tool in nanoscale ductile mode cutting of monocrystalline silicon, *Transactions of the ASME - Journal of Manufacturing Science and Engineering*, Vol. 129, pp.281-286, 2007.

M.B. Cai, X.P. Li and M. Rahman, Molecular dynamics modeling and simulation of nanoscale ductile cutting of silicon, *International Journal of Computer Applications in Technology*, Vol. 28, No.1, pp.2-8, 2007.

M.B. Cai, X.P. Li and M. Rahman, Study of the temperature and stress in nanoscale ductile mode cutting of silicon using molecular dynamics simulation, *Journal of Materials Processing Technology*, Vol. 192/193, pp.607-612, 2007.

M.B. Cai, X.P. Li and M. Rahman, Characteristics of "dynamic hard particles" in nanoscale ductile mode cutting of monocrystalline silicon with diamond tools in relation to tool groove wear, *Wear*, Vol. 263, pp.1459-1466, 2007.

M.B. Cai, X.P. Li and M. Rahman, High pressure phase transformation as the mechanism of ductile chip formation in nanoscale cutting of silicon wafer, *Proceedings of the Institution of Mechanical Engineers Part B – Journal of Engineering Manufacture*, Vol. 221, pp. 1511-1519, 2007.

X.P. Li, M.B. Cai, K. Liu, M. Rahman, Characteristics of ductile mode chip formation in nanoscale cutting of brittle materials, *International Journal of Abrasive Technology*, Vol. 1, No. 1, pp. 37-58, 2007.

M.B. Cai, X.P. Li and M. Rahman, Molecular dynamics simulation of the effect of tool edge radius on cutting forces and cutting region in nanoscale ductile cutting of silicon, *Int. J. Manufacturing Technology and Management*, Vol. 7, No. 5/6, pp. 455-466, 2005.

S. Arefin, X.P. Li, M.B. Cai, M. Rahman, K. Liu, A.A.O. Tay, Effect ofcutting edge radius on machined surface in nanoscale ductile mode cutting of silicon wafer,

Proceedings of the Institution of Mechanical Engineers Part B – Journal of Engineering Manufacture, Vol. 221, pp.213-220, 2007.

International Conference Papers:

X.P. Li, M.B. Cai, and M. Rahman, Study of the upper bound of tool edge radius in nanoscale ductile mode cutting of silicon wafer, *Proceedings of 2007 International Conference on Product Design and Manufacturing Systems (PDMS 07)*, Chongqing, China, October 12-15, 2007.

M.B. Cai, X.P. Li and M. Rahman, Study of the temperature and stress in nanoscale ductile mode cutting of silicon using molecular dynamics simulation, *Proceedings of the 7th Asia Pacific Conference on Materials Processing*, Singapore, December 4-6, 2006.

M.B. Cai, X.P. Li and M. Rahman, Study of the crack initiation in nanoscale ductile mode cutting of silicon by molecular dynamics simulation, *2006 International Symposium on Flexible Automation*, pp. 85-91, Japan, July 9-14, 2006.

X.P. Li, M.B. Cai and M. Rahman, Study of nanoscale ductile mode cutting of silicon using molecular dynamics simulation, *Proceedings of the 7th International Conference on Frontiers Design and Manufacturing*, Guangzhou, pp. 391-394, China, June 19-22, 2006.

M.B. Cai, X.P. Li and M. Rahman, Molecular dynamics simulation of the effect of tool edge radius on cutting forces and cutting region in nanoscale ductile cutting of silicon, *In: Proceedings of the Thirteenth International Conference on Processing and Fabrication of Advanced Materials*, Singapore, December 6-8, 2004.

References

Alder, B. and T. Wainwright. Studies in Molecular Dynamics. I. General Method, J. Chem. Physics, *31*, pp.459-466. 1959.

Alder, B. and T. Wainwright. Studies in Molecular Dynamics. II. Behavior of A Small Number of Elastic Spheres, J. Chem. Physics, *33*, pp.1439-1451. 1960.

Allen, M.P. and D.J. Tildesley. Computer Simulation of Liquid. Oxford: Clarendon press, p.25. 1986.

Baskes, M.I. Modified Embedded-atom Potentials for Cubic Materials and Impurities, Physical Review B, *46*, pp.2727-2742. 1992.

Bakon, A. and A. Szymanski. Practical Uses of Diamond. New York: Ellis horwood, p.30. 1992.

Beeman, D. Some Multistep Methods for Use in Molecular Dynamics Calculations, J. Comput. Phys., *20*, p.130. 1976.

Bifano, T.G., T.A. Dow, R.O. Scattergood. Ductile-Regime Grinding of Brittle Materials: Experimental Results and the Development of a Model, SPIE – Advances in Fabrication and Metrology for Optic and Large Optics, 966, pp.108-115. 1988.

Bifano, T.G., T.A. Dow, R.O. Scattergood. Ductile-Regime Grinding: A New Technology for Machining Brittle Materials, Transactions of the ASME, *113*, pp.184-189. 1991.

Blackley, W.S. and R.O. Scattergood. Ductile-Regime Machining Model for Diamond Turning of Brittle Materials, Precision Engineering, *13*, pp.95-103. 1991.

Belak, J. and I.F. Stowers. Molecular Dynamics Model of the Orthogonal Cutting Process, Proc. Am. Soc. Prec. Eng., Rochester, New York, pp.76-79. 1990.

Belak, J, D.B. Boercher and I.F. Stowers, Simulation of Nano-Scale Deformation of Metallic and Ceramic Surface, MRS BULLETIN/MAY, pp.55-60, 1993

Blackley, W.S. and R.O. Scattergood. Chip Topography for Ductile-Regime Machinng of Germanium, ASME Transactions-Journal of Engineering for Industry, *116*, pp.263-266. 1994.

Blake, P.N., Ronald O. Scattergood. Ductile-Regime Machining of Germanium and Silicon, Journal of American Ceramic Society, *73*, pp.949-957. 1990.

Born, M. and T. Von Karman. Über Schwingungen in Raumittern, Physik. Z., *13*, pp.297-309. 1912.

Chandra, N., S. Namilae, and C. Shet. Local Elastic propertys of Carbon Nanotubes in the Presence of Stone-Wales Defects, Physical Review B, *69*, 094101. 1984.

Cheng, K., X. Luo, R. Ward, and R. Holt. Modeling and Simulation of the Tool Wear in Nanometric Cutting, Wear, *255*, pp.1427-1432. 2003.

Cheong, W.C.D. and L.C. Zhang. Molecular Dynamics Simulation of Phase Transformation in Silicon Monocrystals Due to Nano-Indentation, Nanotechnology, *11*, pp. 173-180. 2000.

Daw, M.S., M.I. Baskes. Embedded-atom method: Derivation and Application to Impurities, Surfaces, and other Defects in Metals, Physical Review B, *29*, pp.6443-6453. 1984.

Daw, M.S., M.I. Baskes. Semiempirical, Quantum Mechanical Calculation of Hydrogen Embrittlement in Metals, Physical Review Letters, *50*, pp.1285-1288. 1983.

Doyama, M., Y. Kogure. Embedded Atom Potentials in FCC and BCC Metals, Computational Materials Science, *14*, pp.80-83. 1999

Fabrizio, C. Representation of Mechanical Loads in Molecular Dynamics Simulation, Physical Review B, *65*, 014107. 2001.

Fang, F.Z., H. Wu and Y.C. Liu. Modelling and Experimental Investigation on Nanometric Cutting of Monocrystalline Silicon, International Journal of Machine Tools & Manufacture, *45*, pp.1681-1686. 2005.

Fang, F.Z., V.C. Venkatesh. Diamond Cutting of Silicon with Nanometric Finish, Annals of the CIRP, *47*, pp.45-49. 1998.

Fang, T.H. and C. Weng. Three-Dimensional Molecular Dynamics Analysis of Processing Using a Pin Tool on The Atomic Scale, Nanotechnology, *11*, pp.148-153. 2000.

Field, J. E. The Properties of Diamond. London: Academic press, p.400. 1979.

Foiles, S.M. Embedded-atom and Related Methods for Modeling Metallic System, MRS Bull, *21*, pp.24-28. 1996.

Frankel, D. and B. Smit. Understanding Molecular Simulation: From Algorithms to Applications. pp.67-69, New York: Academic Press. 2002.

Gao, F., J. He, E. Wu, S. Liu, D. Yu, D. Liu, S. Zhang, and Y. Tian. Hardness of covalent crystals, Physical Review Letters, *91*, 015502. 2003.

Gear, C.W. Numerical Initial Value Problems in Ordinary Differential Equations. NJ: Prentice-Hall, Englewood Cliffs, Chapter 9. 1971.

Glardon, R.E., I. Finne, Some Observations on the Wear of Single Point Diamond Tools Used for Machining Glass, J. Mater. Sci., *16*, pp.1776–1784. 1981.

Haile, J.M. Molecular Dynamics Simulation: Elementary Methods. Wiley, p.65, p.293. 1992.

Han, X.S., B. Lin, S.Y. Yu, S.X. Wang. Investigation of Tool Geometry in Nanometric Cutting by Molecular Dynamics Simulaion, Journal of Materials Processing Technology, *129*, pp.105-108. 2002.

Heermann, D.W. Computer Simulation Method in Theoritical Physics. New York: Springer-Verlag, p.37. 1990.

Hoover, W.G., C.G. Hoover and I.F. Stowers. Interface Tribology by Nonequilibrium Molecular Dynamics Fabrication Technology, Mater Res. Soc. Symp., *140*, pp.119-122. 1989.

Huerta, M. and S. Malkin. Grinding of Glass: The Mechanics of the Process, ASME Transactions, Journal of Engineering for Industry, *98*, pp.459-467. 1976.

Hull, D. and D.J. Bacon. Introduction to Dislocations. Oxford: Butterworth-Heinemann, p.47. 2001.

Ichimura, H. and A. Rodrigo. The Correlation of Scratch Adhesion with Composite Hardness for TiN Coatings, Surface and Coatings Technology, *126*, pp.152-158. 2000.

Inamura, T., N. Takezawa and N. Taniguchi. Atomicscale Cutting in a Computer Using Crystal Models of Copper and Diamond, Ann. CIRP, *41*, pp.121-124. 1992.

Inamura, T., N. Takezawa, Y. Kumaki and T. Sata. On a Possible Mechanism of Shear Deformation in Nanoscale Cutting, Ann. CIRP, *43*, pp.47-50. 1994.

Inamura, T., S. Shimada and N. Nakahara, Brittle/Ductile Transition Phenomena Observed in Computer Simulations of Machining Defect-Free Monocrystalline Silicon, Annals of the CIRP, *46*, pp.31-34. 1997.

T. Inamura, S. Shimada, N. Takezawa and N. Ikawa, Crack Initiation in Machining Monocrystalline Silicon, Annals of the CIRP, *48*, pp.81-84. 1999.

Ikawa, N., R. Donaldson, R. Komanduri, W. Konig, P.A. McKeown, T. Moriwaki and I. Stowers. Ultraprecision Metal Cutting - the Past, the Present, and the Future, Ann. CIRP, 40, pp.587-594. 1991a.

Ikawa, N., S. Shimada, H. Tanaka, and G. Ohmori. An Atomistic Analysis of Nanometric Chip Removal as Affected by Tool–Work Interaction in Diamond Turning, Ann. CIRP, *40*, pp.551-554. 1991b.

Kantorovich, L.V. and V.I. Krylov. Approximate Method of Higher Analysis. New York: Wiley. 1964.

Keen, D., Some Observations on the Wear of Diamond Tools Used in Piston Machining, Wear, *17*, pp.195–208. 1971.

King, R.F. and D. Tabor. The Strength Properties and Frictional Behavior of Brittle Solids, Proceedings of the Royal Society of London, Series A: Mathematical and Physical Science, *223*, pp. 225-238. 1954.

Komanduri, R. Some Aspects of Machining with Negative Rake Tools Simulating Grinding, Int. J. Mach. Tool Des Res., *11*, pp.223-233. 1971.

Komanduri, R., D.A. Lucca, Y. Tani. Technological Advances in Fine Abrasive Process, Annals of the CIRP, *46*, pp.545-596. 1997.

Komanduri, R., N. Chandrasekaran and L.M. Raff. Effect of Tool Geometry in Nanometric Cutting: A Molecular Dynamics Simulation Approach, Wear, *219*, pp.84-97. 1998.

Komandury, R. and L.M. Raff. A Review on the Molecular Dynamics Simulation of Machining at the Atomic Scale, Proceedings of the Institution of Mechanical Engineers Part B, *215*, pp.1640-1672. 2001.

Komanduri, R., N. Chandrasekaran and L.M. Raff. Molecular Dynamics Simulation of the Nanometric Cutting of Silicon, Philosophical Magazine B, *81*, pp.1989-2019. 2001.

Lawn, B.R. and A.G. Evans. A model for Crack Initiation in Elastic/Plastic Indentation Fields, Journal of Materials science, *12*, pp.2195-2199. 1977.

Lawn, B.R., A.G. Evans and D.B. Marshall. Elastic-Plastic Indentation Damage in Ceramics: The Median Radial Crack System, Journal of American Ceramic Society, *63*, pp.574-581. 1980.

Lawn, B.R. and R. Wilshaw. Indentation Fracture: Priciples and Applications, Journal of Materials science, *10*, pp.1049-1081. 1975.

Lennard-Jones, J.E. Forces between Atoms and Ions, Proc. R. Soc. (Lond.) A, *109*, p.584. 1925.

Lennard-Jones, J.E. and B.M. Dent. Forces between Atoms and Ions, Proc. R. Soc. (Lond.) A, *112*, pp.230-234. 1926.

Leung, T.P, W.B. Lee, X.M. Lu. Diamond Turning of Silicon Substrates in Ductile-Regime, Journal of Materials Processing Technology, *73*, pp.42-48. 1998.

Li, X.P., T. He, and M. Rahman. Tool Wear Characteristics and Their Effects on Nanoscale Ductile Mode, Wear, *259*, pp.1207–1214. 2005.

Li, X.P., M. Rahman, K. Liu, K.S. Neo and C.C. Chan. Nano-precision Measurement of Diamond Tool Edge Radius for Wafer Fabrication, Journal of Materials Processing Technology, *140*, pp.358-362. 2003.

Liu, K. and X.P. Li. Modeling of Ductile Cutting of Tungsten Carbide, Transactions of NAMRI/SME, *XXIX* , pp. 251-258. 2001.

Maekawa, K. and A. Itoh., Friction and Tool Wear in Nano-Scale Machining-A Molecular Dynamics Approach, Wear, *188*, pp.115-122. 1995.

Marshall, D.B., B.R. Lawn. Indentation of Brittle Materials, Microindentation Technology in Materials Science and Engineering, ASTM STP, *889*, pp.26-46. 1986.

Mishin, Y., D. Farkas, M.J. Mehl and D.A. Papaconstantopoulos. Interatomic Potentials for Monoatomic Metals from Experimental Data and Ab Initio Calculations, Physical Review B, *59*, pp.3393–3407. 1999.

Morris, J.C., D.L., Callahan, J. Kulik, J.A. Patten and R.O. Scattergood. Origins of the Ductile Regime in Single-Point Diamond Turning of Semiconductors, Journal of the American Society, *78*, pp.2015-2020. 1995.

Morse, P.M. Diatomic Molecules according to the Wave Mechanics II Vibration Levels, Phys. Rev., *34*, pp.57-64. 1929.

Nakasuji, T., S. Kodera, S. Hara, H. Matsunga, N. Ikawa and S. Shimada. Diamond Turning of Brittle Materials for Optical Components, Annals of the CIRP, *39*, pp.89-92. 1990.

Needs, J. and A. Mujica. First-Principles Pseudopotential Study of the Structural Phase of Silicon, Physical Review B, *51*, 9652-9660. 1995.

Ohmori, H., T. Nakagawa. Mirror Surface Grinding of Silicon Wafers with Electrolytic In-Process Dressing, Annals of the CIRP, *39*, pp. 329-332. 1990.

Pei, Z.J., S.R. Billingsley, S. Miura. Grinding Induced Subsurface Cracks in Silicon Wafers, International Journal of Machine Tools & Manufacture, *39*, pp.1103-1116. 1998.

Pei, Z.J., A. Strasbaugh. Fine Grinding of Silicon Wafers, International Journal of Machine Tools & Manufacture, *41*, pp.659-672. 2001.

Pei, Z.J. A Study on Surface Grinding of 300 mm Silicon Wafers, International Journal of Machine Tools & Manufacture, *42*, pp.385-393. 2002.

Press, W.H., B.P. Flannery, S.A. Teukolsky, and W.T. Vetterling. Numerical Recipes. New York: Cambridge University Press, Chapter 15. 1986.

Puttick, K.E., M.R. Rudman, K.J. Smith, A. Franks, K. Klindsey, Single-Point Diamond Machining of Glasses, Proc. R. Soc. Lond. A, *426*, pp.19-30. 1989.

Puttick, K.E., L.C. Whitmore, C.L. Chao and A.E. Gee. Transition Electron Microscope of Nanomachined Silicon Crystals, Philosophical Magazine A, *69*, pp.91-103. 1994.

Puttick, K.E., L.C. Whitmore, P. Zhdan, A.E. Gee and C.L. Chao. Energy Scaling Transitions in Machining of Silicon by Diamond, Tribology International, *28*, pp.349-355. 1995.

Rahman, A. Correlations in the Motions of Atoms in Liquid Argon, Phys. Rev. A, *136* p.405. 1964.

Rao, R., J.E. Bradby, S. Ruffell, and J.S. Williams. Nanoindentation-induced Phase Transformation in Crystalline Silicon and Relaxed Amorphous Silicon, Microelectronics Journal, *38*, pp.722-726. 2007.

Rentch, R. and I. Inasaki. Molecular Dynamics Simulation for Abrasive Process, Annals of the CIRP, *43*, pp.327-330. 1994a.

Rentch, R. and I. Inasaki. Investigation of Surface Integrity by Molecular Dynamics Simulation, Annals of the CIRP, *44*, pp.295-298. 1994b.

Ruffell, S., J.E. Bradby, and J.S. Williams. High Pressure Crystalline Phase Formation during Nanoindentation: Amorphous versus Crystalline Silicon, Appl. Phys. Lett., *89*, 091919. 2006.

Schiøtz, J., T. Vegge, F.D. Di Tola, and K.W. Jacobsen. Atomic-Scale Simulations of the Mechanical Deformation of Nanocrystalline metals, Physical Review B, *60*, pp.11971-11983. 1999.

Shaw, M.C. A New Theory of Grinding, Mech Chem Trans Inst Eng Aust, *1*, pp.73-78. 1972.

Shimada, S., N. Ikawa, G. Ohmori and H. Tanaka. Molecular Dynamics Analysis as Compared with Experimental Results of Micromachining, Annals of the CIRP, *41*, pp.117-120. 1992.

Shimada, S., N. Ikawa, H. Tanaka, G. Ohmori, J. Uchikoshi and H. Yoshinaga. Feasibility Study on Ultimate Accuracy in Microcutting Using Molecular Dynamics Simulation, Annals of the CIRP, *42*, pp.91-94. 1993.

Shimada, S., N. Ikawa, H. Tanaka, and J. Uchikoshi. Structure of Micromachined surface simulated by Molecular Dynamics Analysis, Annals of the CIRP, *43*, pp.51-54. 1994.

Shimada, S., N. Ikawa, T. Inamura, N. Takezawa, G. Ohmori and T. Sata. Brittle-Ductile Transition Phenomena in Microindenation and Micromachining, Annals of the CIRP, *44*, pp.523-526. 1995.

Shimada, S. Molecular Dynamics Analysis of Nanometric Cutting Process, Int. J. Japan. Soc. Prec. Eng., *29*, pp.283-286. 1995.

Shimada, S., T. Inumura and N. Ikawa. Possible Mechanism of Brittle-Ductile Transition in Material Removal in Micromachining of Brittle Materials, International Symposium on Abrasive Technology, pp.28-32. 1997.

Slawomir, B. and B. Witold. Molecular Dynamics Simulation of Stress Relaxation in Metals and Polymers, Physical Review B, *49*, pp.6494-6500. 1994.

Stillinger, F.H. and T.A. Weber. Computer Simulation of Local Order in Condensed Phases of Silicon, Physical Review B, *31*, p.5262. 1985.

Swain, M.V. Microfracture about Scratches in Brittle Solids, Proceedings of the Royal Society of London, Series A: Mathematical and Physical Science, *366*, pp.575-597. 1979.

Swope, W.C., H.C. Andersen, P.H. Berens, and K.R. Wilson. A computer Simulation Methodnfor the Calculation of Equilibrium Constants for the Formation of Physical Clusters of Molecules: Application to Small Water Clusters, J. Chem. Phys., *76*, p.637. 1982.

Tada, H., P.C. Paris and G.R. Irwin. The Stress Analysis of Cracks Handbook. New York: ASME Press, p.71. 2000.

Tersoff, J. New Empirical Approach for the Structure and Energy of Covalent systems, Physical Review B, *37*, pp.6991-7000. 1988.

Tersoff, J. Modeling Solid-state Chemistry: Interatomic Potentials for Multicomponent Systems, Physical Review B, *39*, pp.5566-5568. 1989.

Trent, E.M. Metal Cutting. London: Butterworths. 1977.

Venkatesh, V.C., I. Inasaki, H.K. Toenshof, T. Nakagawa, and I.D. Marinescu. Observations on Polishing and Ultraprecision Machining of Semiconductor Substrate Materials, Annals of the CIRP, *44*, pp.611-618. 1995.

Verlet, L. Computer 'Experiments' on Classical Fluids. I. Thermodynamical Properties of Lennard-Jones Molecules, Phys. Rev., *159*, p.98. 1967.

Wada, R., H. Kodama, K. Nakamura, Y. Mizutani, Y. Shimura, and N. Takenaka, Wear Characteristics of Single Crystal Diamond Tool, Ann. CIRP, *29*, pp. 47–52. 1980.

Wu, H.A. Molecular Dynamics Study on Mechanism of Metal Nanowire, Mechanics Research Communication, *33*, pp.9-16. 2006.

Yan, J., M. Yoshino, T. Kuriagawa, T. Shirakashi, K. Syoji and R. Komanduri, On the Ductile Machining of Silicon for Micro Electro-mechanical System (MEMS), Opto-electronic and Optical Applications, Materials Science and Engineering A, *297*, pp.230-234. 2001.

Yan, J., K. Syoji, and J. Tamaki. Some Observations on the Wear of Diamond Tools in Ultra-Precision Cutting of Single-Crystal Silicon, Wear, *255*, pp.1380-1387. 2003.

Ye, Y.Y., R. Biswas, J.R. Morris, A. Bastawros and A. Chandra, Molecular Dynamics Simulation of Nanoscale Machining of Copper, Nanotechnology, *14*, pp.390-396. 2003.

Zhang, L.C. and H. Tanaka. Atomic Scale Deformation in Silicon Monocrystals Induced by Two-body and Three-body Contact Sliding, Tribology International, *31*, pp.425-433. 1998.

Zhang, L.C. and H. Tanaka. On the Mechanics and Physics in the Nano-Indentation of Silicon Monocrystals, JSME International Journal Series A, *42*, pp.546-559.1999.

Zimmerman, J.A., E.B. Webb III, J.J. Hoyt, R.E. Jones, P.A. Klein, and D.J. Bammann. Calculation of Stress in Atomic Simulation, Modelling and Simulation in Materials Science and Engineering, *12*, pp.319-332. 2004.

Zhong, Z. and V.C. Venkatesh. Surface Integrity Studies on the Grinding, Lapping and Polishing Processes for Optical Products, J Mater Process Tech, *44*, pp.176-186. 1994.